



**Francisco
de Nolasco Santos**

**Upstream Tower Effect on Wind Turbine Blade
Flow**

Efeito a Montante da Torre no Escoamento em torno das
Pás de uma Turbina Eólica



**Francisco
de Nolasco Santos**

Upstream Tower Effect on Wind Turbine Blade Flow

Efeito a Montante da Torre no Escoamento em torno das
Pás de uma Turbina Eólica

Dissertação apresentada à Universidade de Aveiro para cumprimento dos requisitos necessários à obtenção do grau de Mestre em Engenharia Mecânica, realizada sob orientação científica de Vítor António Ferreira da Costa, Professor Catedrático do Departamento de Engenharia Mecânica da Universidade de Aveiro, e de Reinhard Willinger, Ao.Univ.Prof. Dipl.-Ing. Dr.Techn. do Institut für Energietechnik und Thermodynamik Forschungsbereich Strömungsmaschinen, da Universidade Técnica de Viena.

This book/thesis/dissertation/etc is supported by the projects UID/EMS/00481/2019-FCT - FCT - Fundação para a Ciência e a Tecnologia; and CENTRO-01-0145-FEDER-022083 - Centro Portugal Regional Operational Programme (Centro2020), under the PORTUGAL 2020 Partnership Agreement, through the European Regional Development Fund

o júri / the jury

presidente / president

Prof. Doutor Fernando José Neto da Silva

Professor Auxiliar Departamento de Engenharia Mecânica Universidade de Aveiro

Prof. Doutor António Manuel Gameiro Lopes

Professor Auxiliar do Departamento de Engenharia Mecânica Faculdade de Ciências e Tecnologia da Universidade de Coimbra

Prof. Doutor Vítor António Ferreira da Costa

Professor Catedrático Departamento de Engenharia Mecânica Universidade de Aveiro

agradecimentos / acknowledgements

Ao Professor Doutor Vítor António Ferreira da Costa, pela orientação cuidada, conhecimento, críticas construtivas, afabilidade, inexcedível disponibilidade e atenção, e pelo seu grande interesse. Ao *Ao.Univ.* Professor Doutor Reinhard Willinger por me ter acolhido na Universidade Técnica de Viena, bem como, pelo acompanhamento ímpar, grande saber técnico, paciência e simpatia, que o levou a reparar-me a bicicleta.

Ao corpo docente do Departamento de Engenharia Mecânica da Universidade de Aveiro, que diariamente incorpora o ideal de uma Academia humana e interessada nos seus alunos.

A todos os meus amigos que, pelo companheirismo e encorajamento, tornaram este percurso numa experiência mais alegre. Agradeço em particular ao Zé, Afonso, Danny, Diogo e João por terem ido verificar a Viena o estado da tese, ao Christian e à Mareike.

Por último lugar, à minha família, que muito me apoiou durante o meu percurso académico, em especial aos meus pais, avó e irmã.

To Prof. Dr. Vítor António Ferreira da Costa, for his attentive supervising, knowledge, constructive criticism, affability, exemplary availability and care, and for his great interest.

To *Ao.Univ.Prof. Dipl.Ing. Dr.Techn.* Reinhard Willinger for having welcomed me at the *Technische Universität Wien*, and for his unmatched mentoring, great technical knowledge, patience and friendliness, which lead him to repair my bicycle. *Vielen Dank für alles.*

To the faculty of the Mechanical Engineering Department of the University of Aveiro, which embodies daily the ideal of a Academy which is humane and invested in its students.

To all my friend that, through their companionship and encouragement, have made this academic path in a more joyus experience. I thank in particular Zé, Afonso, Danny, Diogo and João for having traveled to Vienna to verify the state of the thesis, to Christian and Mareike.

Finally, to my family, which has always supported me through my studies, especially to my parents, grandmother and sister.

keywords

XFOIL, Potential Flow, Wind Turbines, Tower Interference, Upstream Tower Effect

abstract

The present work is focused on the study of the upstream tower effect on wind turbine blade flow through the employment of simplified methods. The state-of-the-art on aerodynamic loading predictive methods is presented and discussed through the comparison of their advantages and disadvantages, with emphasis on Engineering (or Potential Flow) Methods, on which the present work is based. The quality of results attained by Engineering Methods is also discussed. A short chapter on dimensional analysis is included, as the governing dimensional parameters are of major importance in this context. The potential flow theory is also presented, as its solutions are of the utmost importance to describe the flow around the tower. Thereafter, the lift and drag coefficients are calculated with the use of the panel-method-based software XFOIL, which utilizes as boundary conditions the potential flow solutions (later revised through Bak's model). This model is implemented through a MATLAB interface and is validated through QBLADE and secondary literature. Finally, the tangential and normal force coefficients are calculated based on XFOIL's outcomes and a critical discussion ensues, leading to the work's conclusions and future research paths.

palavras-chave

XFOIL, Escoamento Potencial, Turbinas Eólicas, Interferência da Torre, Efeito a Montante da Torre

resumo

O objecto deste trabalho é o estudo da influência a montante da torre no escoamento através das pás de uma turbina eólica empregando métodos simplificados. O estado-da-arte de métodos preditivos de forças aerodinâmicas é apresentado e discutido enumerando as vantagens e desvantagens de cada um, com ênfase nos Métodos de Engenharia (ou Potencial), nos quais se baseia o trabalho aqui apresentado. A qualidade dos resultados obtidos pelos Métodos de Engenharia também é discutida. É incluído um curto capítulo sobre análise dimensional, uma vez que os parâmetros adimensionais são da maior importância neste contexto. A teoria do escoamento do potencial é apresentada, uma vez que as suas soluções são de extrema importância para a descrição do escoamento em torno da torre. Em seguida, os coeficientes de impulso e de arrasto são calculados usando o *software* baseado num método do painel, XFOIL, que utiliza como condições de fronteira as soluções do escoamento potencial (que são posteriormente readaptadas através do modelo de Bak). Este modelo é implementado através de uma interface com o programa MATLAB e validado com resultados provenientes da literatura e através do *software* QBLADE. Finalmente, os coeficientes das forças tangencial e normal são calculados com base nos resultados obtidos com o XFOIL, seguindo-se uma discussão crítica, conducente às conclusões e direcções de trabalhos futuros.

Contents

I	Introduction and Background	1
1	Introduction to Wind Turbines	3
1.1	Why Wind Turbines?	3
1.2	Wind Turbine History and Blade Geometry	4
1.2.1	History and Types of Wind Turbines	4
1.2.2	Blade Geometry	6
1.3	Wind Turbine Aerodynamics and Tower Interference	9
1.4	Dynamic Stall in Wind Turbines	11
1.5	Betz Limit	13
2	State-of-the-art in Predictive Methods	17
2.1	Blade Element Method (BEM)	17
2.2	Engineering Methods (EM)	20
2.2.1	Lifting-Line Theory	21
2.2.2	Panel Methods	21
2.3	Computational Fluid Dynamics (CFD)	23
2.4	Comparison	25
3	Objectives and Lecture Guide	29
II	Software and Methods	31
4	Dimensional Analysis	33
4.1	Buckingham's II-Theorem	33
4.2	Application on the Tower of a Wind Turbine	34
4.3	Dimensionless Numbers	36
4.4	Reynolds Number in Wind Turbines	37
5	Potential Flow Theory	39
5.1	Theoretical Background	39
5.1.1	Elementary Plane Flow Solutions	42
5.2	Circular Cylinder	44

6	XFOIL	51
6.1	Introduction to XFOIL	51
6.2	MATLAB Interfaces	53
6.2.1	Airfoil Selection and Benchmarks	53
6.2.2	S809 Profile	57
6.2.3	MATLAB-XFOIL Interface	58
7	QBlade	63
III	Model and Results	67
8	Tower Interference Model	69
8.1	Coordinate System	75
8.2	Airfoil forces	77
8.3	Intermediary Results and Model Validation	78
9	Results	83
9.1	Sensibility Study	83
9.2	Lift and Drag Coefficients	84
9.3	Tangential- and Normal Coefficients	89
9.4	Twist Angle	92
9.5	Bak Model	97
IV	Discussion	103
10	Discussion	105
V	Conclusions	111
11	Conclusions and Further Research Directions	113
	Bibliography	114

List of Tables

2.1	Comparison of different methods	25
4.1	Dimensionless groups.	37
6.1	Typical values of n . Adapted from Drela [Drela 1989].	52
6.2	Abridge NACA 2415 airfoil coordinate table.	53
6.3	Sequence of XFOIL sequence orders.	60
8.1	Conversion table between $\Delta x/D$ and gap/D	76
9.1	Coefficient of variation and range according to gap for Reynolds number and angle of attack.	84
9.2	Maximum and minimum lift coefficient increase/decrease in relation to undisturbed value.	87
9.3	Maximum and minimum drag coefficient increase/decrease in relation to undisturbed value.	89

Intentionally blank page.

List of Figures

1.1	Earliest known illustration of a windmill by Jacques Besson (1578) [Russo 1948]. Extracted from "Power From Wind: a History of Windmill Technology," by R.L. Hills, 1996, Cambridge University Press [Hills 1996]. . . .	4
1.2	Savonius-Rotor [Savonius 1981]. Extracted from "Introduction to Wind Turbine Aerodynamics," by A.P. Schaffarczyk, 2014, Springer Verlag [Schaffarczyk 2014].	5
1.3	Darrieus-Rotor [Darrieus 1931]. Extracted from "Introduction to Wind Turbine Aerodynamics," by A.P. Schaffarczyk, 2014, Springer Verlag [Schaffarczyk 2014].	5
1.4	H-Darrieus-Rotor [Darrieus 1931]. Extracted from "Introduction to Wind Turbine Aerodynamics," by A.P. Schaffarczyk, 2014, Springer Verlag [Schaffarczyk 2014].	5
1.5	Schematic of wind turbine constituent parts.	6
1.6	Schematic of horizontal axis wind turbine rotor blade.	6
1.7	Blade Profile. Extracted from "Wind Turbine Blade Design," by P.J. Schubel and R.J. Crossley, 2012, Energies [Schubel and Crossley 2012]. . .	7
1.8	Schematic of common airfoil terminology and lift/drag forces.	8
1.9	Hele-Shaw flow [Hele-Shaw 1898] past an inclined NACA 64A015 airfoil. Extracted from "An Album of Fluid Motion," by M. Van Dyke, 1982, Parabolic Press Stanford [Van Dyke 1982].	9
1.10	Schematic of upwind and downwind tower configurations. Extracted from "Evaluation of Tower Shadow Effects on Various Wind Turbines Concepts," by F. Zahle, H. A. Madsen and N. N. Sørensen, 2009 [Zahle <i>et al.</i> 2009].	10
1.11	Effect of tower shadow on mechanical torque with and without blade and tower dynamics for different levels of tower interference (0 [...], 0.1 [o], 0.2 [*], 0.3 [×]). Extracted from "The Impact of Tower Shadow, Yaw Error, and Wind Shears on Power Quality in a Wind–Diesel System," by R. Fadaeinedjad, G. Moschopoulos and M. Moallem, 2009 [Fadaeinedjad <i>et al.</i> 2009].	10
1.12	Effect of tower shadow on output power and voltage with and without blade and tower dynamics for different levels of tower interference (0 [...], 0.1 [o], 0.2 [*], 0.3 [×]). Extracted from "The Impact of Tower Shadow, Yaw Error, and Wind Shears on Power Quality in a Wind–Diesel System," by R. Fadaeinedjad, G. Moschopoulos and M. Moallem, 2009 [Fadaeinedjad <i>et al.</i> 2009].	11

1.13	Airflow separation from airfoil as characteristic in stall. Adapted from "Le Tunnel Hydrodynamique au Service de la Recherche Aéronautique," by H. Werlé, 1974, ONERA [Werlé 1974].	12
1.14	Kelvin-Helmholtz instability of superposed streams. Both streams move to the right, but the upper one does so with a superior velocity. Adapted from "An Album of Fluid Motion," by M. Van Dyke, 1982, Parabolic Press Stanford [Van Dyke 1982].	12
1.15	Energy extraction by stream tube in a wind turbine. Extracted from "Wind Energy Handbook," by T. Burton, D. Sharpe, N. Jenkins and E. Bossanyi, 2011 [Burton <i>et al.</i> 2011].	13
1.16	Actuator disc and stream tube. Adapted from "Wind Energy Handbook," by T. Burton, D. Sharpe, N. Jenkins and E. Bossanyi, 2011 [Burton <i>et al.</i> 2011].	14
2.1	The local loads on a blade; \mathbf{R} is the vector sum of the lift and the drag. F_t and F_n are the tangential and normal components of \mathbf{R} , respectively. Adapted from "Aerodynamics of Wind Turbines," by M. Hansen, 2015 [Hansen 2015].	18
2.2	Flow field representations. Extracted from "Development of a Wind Turbine Aerodynamics Simulation Module," by A. Van Garrel, 2003, Energy Research Center of the Netherlands, ECN [Van Garrel 2003].	20
2.3	Flow field approximations. Extracted from "Development of a Wind Turbine Aerodynamics Simulation Module," by A. Van Garrel, 2003, Energy research Center of the Netherlands, ECN [Van Garrel 2003].	20
2.4	Inviscid panel method airfoil discretization. Adapted from "2D Panel Methods," by Aerodynamics for Students, 2019 [Aerodynamics for Students 2019].	22
2.5	Snapshot of axial velocity. Extracted from "Evaluation of Tower Shadow Effects on Various Wind Turbines Concept," by F. Zahle, H. A. Madsen and N. N. Sørensen, 2009 [Zahle <i>et al.</i> 2009].	24
2.6	Comparison of the flapwise bending moment for the test blade calculated using the original BEM code and the corrected one. Extracted from "Load pulses on wind turbine structures caused by tower interference," by A. Gómez and J.R. Seume, 2009 [Gómez and Seume 2009b].	26
2.7	Location of attachment point for different TIMs. Extracted from "On 2D and 3D potential flow models of upwind wind turbine tower interference," by M.A. Lackner, N. deVelder and T. Sebastian, 2013 [Lackner <i>et al.</i> 2013].	27
2.8	Induced velocity in the x -direction for various TIMs. Extracted from "On 2D and 3D potential flow models of upwind wind turbine tower interference," by M.A. Lackner, N. deVelder and T. Sebastian, 2013 [Lackner <i>et al.</i> 2013].	28
4.1	Schematic of variables involved in a flow through a circular tower.	35
4.2	Evolution of wind turbine rotor blades. Extracted from "Design of a fibrous composite preform for wind turbine rotor blades," by J. Zangenberg, P. Brøndsted and M. Koefoed, 2013 [Zangenberg <i>et al.</i> 2014].	38

4.3	Lift-to-drag ratio for a DU00-W2-401 airfoil. Extracted from "Reynolds number effect on the optimization of a wind turbine blade for maximum aero-dynamic efficiency," by M. Ge, D. Tian and Y. Deng, 2014 [Ge <i>et al.</i> 2014].	38
5.1	Orthogonality between potential lines and streamlines in an inviscid flow. Extracted from "Fluid Mechanics," by F.M. White, 2011 [White 2011]. . .	41
5.2	Uniform stream. Solid lines are streamlines and dashed lines are potential lines. Extracted from "Fluid Mechanics," by F.M. White, 2011 [White 2011].	42
5.3	Line Source schematic. Solid lines (radial spokes) are streamlines and dashed lines (circles) are potential lines. Extracted from "Fluid Mechanics," by F.M. White, 2011 [White 2011].	43
5.4	Computer-drawn source stream function with 25 contour lines using MATLAB.	43
5.5	Computer-drawn doublet stream function with 100 contour lines using MATLAB.	44
5.6	Hele-Shaw flow [Hele-Shaw 1898] past a circle. Extracted from "An Album of Fluid Motion," by M. Van Dyke, 1982, Parabolic Press Stanford [Van Dyke 1982].	45
5.7	Computer-drawn flow through a circular cylinder, where streamlines are black and potential lines blue. Plotted using MATLAB.	45
5.8	Schematic of source-sink pair in uniform flow. Adapted from "Fluid Mechanics," by F.M. White, 2011 [White 2011].	46
5.9	Computer-drawn circle of radius a stream function with 500 contour lines using MATLAB.	46
5.10	Computer-drawn vortex stream function with 20 contour lines using MATLAB.	47
5.11	Effect of circulation in the flow past a circular cylinder. $K/(c_0 e) = 1$. An inviscid downward lift, the <i>Magnus force</i> [Magnus 1853], given by the Kutta-Joukowski Theorem, is developed normal to the free stream. Extracted from "Fluid Mechanics," by F.M. White, 2011 [White 2011]. . .	48
5.12	Computer-drawn C_p with 15 contour lines using MATLAB's <code>contourf</code> function.	50
6.1	Transition downstream of Tollmien-Schlichting Waves, passing from two-dimensional to three-dimensional and finally, turbulent on the far right side. Extracted from "An Album of Fluid Motion," by M. Van Dyke, 1982, Parabolic Press Stanford [Van Dyke 1982].	52
6.2	Results returned from XFOIL for NACA 2412 profile. Dashed lines represent inviscid calculations, coloured lines viscous calculations.	52
6.3	Three airfoil profiles plotted using MATLAB.	54
6.4	Eppler 387 airfoil profile plotted using MATLAB.	54
6.5	E387 lift and drag curves plotted using MATLAB.	56
6.6	Generic lift curve explaining the occurrence of the maximum. Extracted from "Aircraft Performance and Design," by J. D. Anderson, 1999 [Anderson Jr. 1999b].	56

6.7	E387 C_l/C_d plotted using MATLAB.	56
6.8	E387 Lilienthal polar diagram plotted using MATLAB.	57
6.9	S 809 airfoil profile plotted using MATLAB.	57
6.10	S809 lift and drag curves plotted using MATLAB.	58
6.11	S809 C_l/C_d plotted using MATLAB.	59
6.12	S809 Lilienthal polar diagram plotted using MATLAB.	59
6.13	Example of XFOIL polar save file.	61
7.1	Lilienthal, C_l vs α , C_l vs X_{tr} , C_l/C_d vs α and C_m vs α graphs clock-wise, from left to right.	64
7.2	Optimized blade for S809 airfoil with 10 sections. Computed using QBLADE.	65
7.3	Power coefficient <i>vs</i> tip speed ratio ($TSR = \lambda$). <i>N.b.</i> , maximal value attained for $\lambda = 7$	65
8.1	Velocity magnitude according to y/D for the plane $x = 1 \times diameter(D)$. Plotted using MATLAB.	71
8.2	Velocity magnitude according to y/D for the planes $x = 1.5D, 1.6D, \dots, 2.0D$ (near-tower). Plotted using MATLAB.	71
8.3	Velocity magnitude according to y/D for the planes $x = 2D, 3D, \dots, 7D$ (far-tower). Plotted using MATLAB.	72
8.4	Decomposition of velocity vectors.	73
8.5	Yaw angle variation along y -axis for Ox plane $x = 0.75D$. Plotted using MATLAB.	74
8.6	Yaw angle variation along y -axis for Ox planes $x = 1.0D, \dots, 3.0D$. Plotted using MATLAB.	74
8.7	Schematic of decomposition of the absolute velocity and angle relations.	75
8.8	Decomposition of velocity vectors.	75
8.9	Definition of $y = 0$ in respect to airfoil.	76
8.10	Generation of lift and drag.	77
8.11	Value of c_x/c_0 along y -axis for a gap of $1D$	78
8.12	Value of c_y/c_0 along y -axis for a gap of $1D$	80
8.13	Value of c/c_0 along y -axis for a gap of $1D$	81
8.14	Value of α along y -axis for a gap of $1D$	82
8.15	Variation of velocity vector components along y -axis.	82
9.1	C_l <i>vs</i> α full curve for $-7^\circ \leq \alpha \leq 25^\circ$. Plotted using MATLAB. The dashed box represents the close-up zoomed area.	85
9.2	C_l <i>vs</i> α graph close-up. Plotted using MATLAB.	85
9.3	C_l <i>vs</i> α full curve for $-7^\circ \leq \alpha \leq 25^\circ$ with limit values for C_l , for several gaps. Plotted using MATLAB. The dashed box represents the close-up zoomed area.	86
9.4	C_l <i>vs</i> α close-up with limit values for C_l for several gaps. Plotted using MATLAB. <i>N.b.</i> , $C_{l,min}$ for $gap = 0D$ hasn't been presented, as it would hinder the visualization of the other circles.	87
9.5	C_d <i>vs</i> α full curve for $-7^\circ \leq \alpha \leq 25^\circ$ with limit values for C_d for several gaps. Plotted using MATLAB. The dashed box represents the close-up zoomed area.	88

9.6	C_d vs α close-up with limit values for C_d for several gaps. Plotted using MATLAB.	88
9.7	Value of C_t along y -axis for $gap/D = 1$	90
9.8	Value of C_n along y -axis for $gap/D = 1$	90
9.9	Comparison of C_t values along y -axis for different gaps.	91
9.10	Comparison of C_n values along y -axis for different gaps.	91
9.11	C_l vs α full curve for $-7^\circ \leq \alpha \leq 25^\circ$ with limit values for C_l , for some twist angles, γ . Plotted using MATLAB. The dashed box represents the close-up zoomed area.	93
9.12	C_l vs α close-up with limit values for C_l , for several twist angles, γ . Plotted using MATLAB.	93
9.13	C_d vs α full curve for $-7^\circ \leq \alpha \leq 25^\circ$ with limit values for C_d , for some twist angles, γ . Plotted using MATLAB. The dashed box represents the close-up zoomed area.	94
9.14	C_d vs α close-up with limit values for C_d , for several twist angles, γ . Plotted using MATLAB.	94
9.15	Values of α along y -axis for some twist angles.	95
9.16	Value of C_t along y -axis for some twist angles.	96
9.17	Value of C_n along y -axis for some twist angles.	96
9.18	Value of c_x/c_0 along y -axis for several gaps for the potential theory formulation (full line), as well as for Bak's formulation (dashed line).	98
9.19	Value of c_y/c_0 along y -axis for several gaps for the potential theory formulation (full line), as well as Bak's formulation (dashed line).	99
9.20	Value of α along y -axis for $gap = 1D$	100
9.21	Value of C_t along y -axis vs α for $gap = 1D$	100
9.22	Value of C_n along y -axis vs α for $gap = 1D$	101
10.1	Axial velocity (c_x) calculated with the Bak-Model ($C_d = 1.1$) and with the potential flow model for 3 different gaps. Extracted from "Aerodynamic coupling of rotor and tower in HAWTs," by A. Gómez and J.R. Seume, 2009 [Gómez and Seume 2009a]	106
10.2	Tangential velocity (c_y) calculated with the Bak-Model ($C_d = 1.1$) and with the potential flow model for 3 different gaps. Extracted from "Aerodynamic coupling of rotor and tower in HAWTs," by A. Gómez and J.R. Seume, 2009 [Gómez and Seume 2009a]	106
10.3	Steady tangential force coefficient, C_t , along blade spanwise position. Computed using QBLADE.	107
10.4	Steady axial force coefficient, C_n , along blade spanwise position. Computed using QBLADE.	107
10.5	Steady normal force coefficient, C_n , for a varying angle of attack, for the steady inviscid TIM and a dynamic model. Extracted from "Load pulses on wind turbine structures caused by tower interference," by A. Gómez and J.R. Seume, 2009 [Gómez and Seume 2009b]	108

Intentionally blank page.

Nomenclature

Variables with Latin notation

Symbol	Description	Unit
a	Axial induction factor	[-]
A_0	Cross-sectional area far upstream	[m^2]
A_d	Cross-sectional area at actuator disc	[m^2]
A_{ij}	Influence of vorticity components of panel j on the control point on panel i	[-]
A_r	Cross-sectional area of rotor	[m^2]
A_w	Cross-sectional area at far wake	[m^2]
b	Line source/sink length, Iteration number	[m] , [-]
B_i	Influence of the free stream on panel i	[-]
c	Local absolute velocity	[m/s]
c_0	Undisturbed, free-stream velocity	[m/s]
c_d	Velocity at actuator disc	[m/s]
c_i	Surface tangential velocities at the center of the panel i	[m/s]
c_{local}	Local velocity	[m/s]
c_r	Radial velocity	[m/s]
c_{rel}	Velocity relative to the airfoil/blade section	[m/s]
c_s	Surface velocity	[m/s]
c_{sound}	Speed of sound	[m/s]
$c_{s,j}$	Surface velocity at the center of panel j	[m/s]
c_w	Velocity at far wake	[m/s]
c_x	x velocity component	[m/s]
c_y	y velocity component	[m/s]
c_z	z velocity component	[m/s]
c_θ	Circumferential velocity	[m/s]
$c_{\theta,s}$	Circumferential velocity at cylinder surface	[m/s]
C_d	Drag coefficient	[-]
$C_{d,0}$	Drag coefficient in undisturbed case	[-]
$C_{d,max}$	Maximal drag coefficient	[-]
$C_{d,min}$	Minimal drag coefficient	[-]
C_{df}	Friction drag coefficient	[-]
C_{dp}	Pressure drag coefficient	[-]
C_l	Lift coefficient	[-]

$C_{l,0}$	Lift coefficient in undisturbed case	[-]
$C_{l,max}$	Maximal lift coefficient	[-]
$C_{l,min}$	Minimal lift coefficient	[-]
C_m	Moment coefficient	[-]
C_n	Normal force coefficient	[-]
C_p	Pressure coefficient	[-]
C_{pi}	Surface pressure coefficient	[-]
C_P	Power coefficient	[-]
$C_{P,max}, C_{P,Betz}$	Maximal power coefficient (Betz limit)	[-]
C_t	Tangential force coefficient	[-]
$C_{t n,\gamma=0}$	Tangential/normal coefficient value for zero twist angle	[-]
$C_{t n,\gamma\neq0}$	Tangential/normal coefficient value for a non-zero twist angle	[-]
Ca	Cavitation number	[-]
CV	Variation coefficient	[-]
D	Tower diameter	[m]
e	Cylinder radius	[m]
Eu	Euler number	[-]
F	Reaction force	[N]
F_d	Drag force (by unit of length)	[N/m]
F_l	Lift force (by unit of length)	[N/m]
F_n	Normal force	[N]
F_t	Tangential force	[N]
Fr	Froude number	[-]
g	Body acceleration (gravity)	[m/s ²]
j	Number of repeating variables	[-]
k	Number of dimensionless variables	[-]
K	Vortex strength	[-]
l	Length	[m]
L	Chord	[m]
L_{char}	Characteristic length	[m]
Ma	Mach number	[-]
\dot{m}	mass flow rate	[kg/s]
n	Number of variables	[-]
N_{crit}	Critical number in envelope method	[-]
p	Pressure	[Pa]
p_0	Upstream pressure	[Pa]
\dot{p}_0	Inwards momentum flow rate	[Pa/s]
p_{d-}	Pressure left of actuator disc	[Pa]
p_{d+}	Pressure right of actuator disc	[Pa]
p_s	Pressure at cylinder surface	[Pa]
p_w	Pressure at far wake	[Pa]
\dot{p}_w	Outwards momentum flow rate	[Pa/s]
p_∞	Freestream pressure	[Pa]
P_t	Power (due to tangential force) as felt in airfoil	[W]
\dot{q}	Line source/sink flowing rate	[m ³ /s]
\dot{Q}	Doublet strength	[-]

r	Radius	$[m]$
R	Reaction force vector, Tower/Rotor Radius	$[N]$, $[m]$
Re	Reynolds number	$[-]$
$Re_{undisturbed}$	Reynolds number in tower-free case	$[-]$
\overline{Re}	Mean Reynolds number	$[-]$
S	Normalized increase/decrease	$[-]$
St	Strouhal number	$[-]$
T	Thrust	$[N]$
$T(\%)$	Range	$[-]$
u	Circumferential velocity (airfoil)	$[m/s]$
w	Relative velocity	$[m/s]$
\dot{W}	Power	$[W]$
Wb	Weber number	$[-]$
x_i	Airfoil surface point coordinate	$[m]$
X_{tr}	Laminar/turbulence transition point	$[m]$
z	height	$[m]$

Variables with Greek notation

Symbol	Description	Unit
α	Angle of attack	$[^{\circ}]$
α_0	Angle of attack in tower-free case	$[^{\circ}]$
β	Yaw angle	$[^{\circ}]$
γ	Vorticity, Twist angle	$[1/s]$, $[^{\circ}]$
γ_0	Vorticity strength	$[1/s]$
γ_j	Vorticity strength at panel j	$[1/s]$
Γ	Circulation	$[m^2/s]$
δ	Dirac delta	$[-]$
Δp	Pressure variation	$[Pa]$
Δx	Distance between center of tower and rotor-plane	$[m]$
θ	Angle in radians	$[rad]$
λ	Tip speed ratio	$[-]$
λ_0	Absolute tip speed ratio	$[-]$
λ_R	Tip speed ratio at rotor radius	$[-]$
μ	Dynamic viscosity	$[Ns/m^2]$
ν	Kinematic viscosity	$[m^2/s]$
ξ	Curl or rotational	$[-]$
Π	Power products (Pi-groups)	$[-]$
ρ	Density	$[kg/m^3]$
σ	Source strength, Standard deviation	$[1/s]$, $[-]$
Υ	Angle between w and y -axis	$[^{\circ}]$
ϕ	Potential function, Angle between circumferential and relative velocity	$[m^2/s]$, $[^{\circ}]$

ψ	Stream function	$[m^2/s]$
ψ_{body}	Stream function at body surface	$[m^2/s]$
ω	Rotational speed	$[rad/s]$

Operators with another notation

Symbol	Description	Unit
∇	Nabla, diferential operator	$[-]$
∇^2	Laplacian	$[-]$

Abbreviations

BEM	Blade element momentum method
CFD	Computational fluid dynamics
DTU	<i>Danmarks Tekniske Universitet</i> , Technical University of Denmark
EM	Engineering methods
FAST	Fatigue, aerodynamics, structures, and turbulence
HAWC2	Horizontal axis wind turbine code
HAWT	Horizontal axis wind turbine
LE	Leading edge
MIT	Massachusetts Institute of Technology
NASA	National Aeronautics and Space Administration
NREL	National Renewable Energy Lab
RANS	Reynolds averaged Navier-Stokes
SST	Shear stress transport
TE	Trailing edge
TIM	Tower interference model
TSR	Tip speed ratio
VAWT	Vertical axis wind turbine
WECS	Wind energy conversion systems

Part I

Introduction and Background

Chapter 1

Introduction to Wind Turbines

1.1 Why Wind Turbines?

Energy presents itself as one of the leading challenges facing modern societies [Van Kuik and Peinke 2016]. The World's energy consumption has been increasing, a fact which leaves the energy industry facing burgeoning challenges related to the energetic transition from a fossil fuel to a non-carbon-based economy, driven by environmental and security factors, the latter mostly connected to geopolitical issues [Dorian *et al.* 2006]. Over the past few years, notwithstanding many tumultuous setbacks of varying magnitude, a growing scientific, political and societal consensus has risen, which has led many nations to adopt increasingly ambitious measures [Rogelj *et al.* 2016] to prevent calamitous greenhouse gases emissions, culminating in the Paris Agreement [UNFCCC. 2015].

In spite of the complex political climate which permeates modern societies where, depending on the general outlook, some will think that either too little or too much has been done to enhance this transition into renewable forms of energy, there has been an undeniable increase in the number of scientists, policy-makers and general public members who've become invested in these energetic alternatives. This has been translated into a societal shift which has put renewable energy technologies, and in particular wind energy, in an underlined position, leading to an outstanding growth in its market-share [AWEA 2011] and new demands [Lopion *et al.* 2018]. In the specific case of wind energy, garnered through wind turbines, apart from the factors mentioned above, increased acceptance-rates [Scherhauer *et al.* 2017], an initial small base [Dorian *et al.* 2006], the relatively high job creation [Hansen 2015] and effective policies, such as feed-in tariffs [Pena *et al.* 2017], have led to considerable increments, becoming an increasingly relevant energy-source [Best and Burke 2018].

As such, the study of wind turbines is highly desirable, not only because of the growth recently found in the development of these technologies, but also due to it being a field rich in challenges, most of the times of a multi-disciplinary nature, and whose development is decidedly impactful on the combined efforts to provide a lasting resolution to many of the issues grappling modern societies.

1.2 Wind Turbine History and Blade Geometry

1.2.1 History and Types of Wind Turbines

When contemplating current wind turbines, one often overlooks the millennia of incremental developments that have led to these modern devices (*vd.* Fig. 1.1). One might even have in mind an image of a dutch windmill or of Don Quixote courageously/foolishly charging against a giant/windmill [Cervantes 2017], but, in fact, the development of wind-based technologies is much older than what our collective memory would lead us to believe, purportedly having been around since the 9th century (with the Persian mill) [Hills 1996].

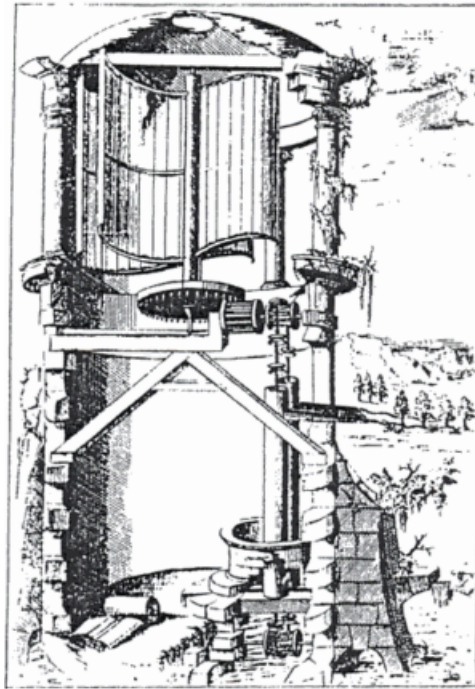


Figure 1.1: Earliest known illustration of a windmill by Jacques Besson (1578) [Russo 1948]. Extracted from "Power From Wind: a History of Windmill Technology," by R.L. Hills, 1996, Cambridge University Press [Hills 1996].

Contemporary wind turbine designs are highly indebted to the early pioneers, as many of the current models are heavily based on traditional models, and their development can be seen as incremental advances after early attempts of adaptation of more archaic models to generate electricity, as exemplified by the work of Poul la Cour [Nissen 2011].

As to their classification (in terms of their orientation), wind turbines can be divided into two major categories: Vertical Axis Wind Turbines (VAWT) or Horizontal Axis Wind Turbines (HAWT). The first type of wind turbines have a vertical rotation-axis (*vd.* Fig. 1.2-1.4), and are seemingly quite advantageous when compared to HAWTs, as they work independently of wind direction. However, due to greater load fluctuations on the blades owing to the half-revolution operation under wake conditions, which result in aerodynamic fatigue loads, VAWTs are more prone to earlier component failure [Schafarczyk 2014].

The most commonly commercially-used wind turbines [Schubel and Crossley 2012]

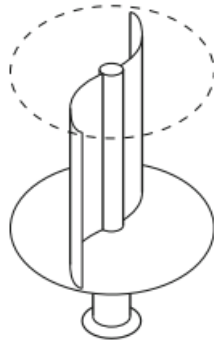


Figure 1.2: Savonius-Rotor [Savonius 1981]. Extracted from "Introduction to Wind Turbine Aerodynamics," by A.P. Schaffarczyk, 2014, Springer Verlag [Schaffarczyk 2014].

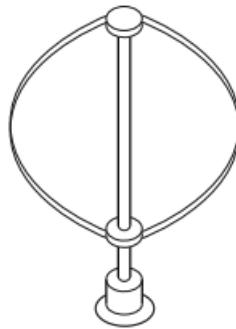


Figure 1.3: Darrieus-Rotor [Darrieus 1931]. Extracted from "Introduction to Wind Turbine Aerodynamics," by A.P. Schaffarczyk, 2014, Springer Verlag [Schaffarczyk 2014].

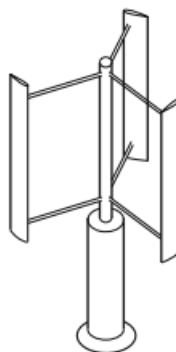


Figure 1.4: H-Darrieus-Rotor [Darrieus 1931]. Extracted from "Introduction to Wind Turbine Aerodynamics," by A.P. Schaffarczyk, 2014, Springer Verlag [Schaffarczyk 2014].

are then wind turbines whose rotating-axis is horizontal (*vd.* Fig. 1.5), whose main constituent parts are the hub, rotor (blades attached to hub), nacelle and tower.

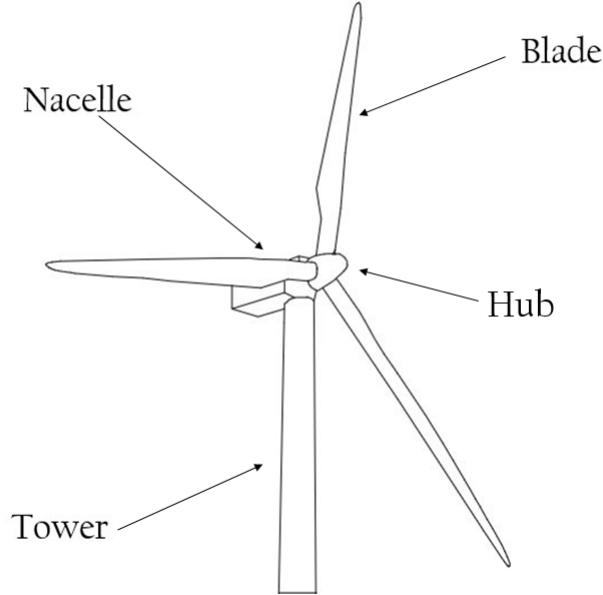


Figure 1.5: Schematic of wind turbine constituent parts.

1.2.2 Blade Geometry

Of all the components comprising of a wind turbine, the rotor blade geometry is of the utmost importance, as HAWTs output is highly sensitive to changes in the blade profile. Figure 1.6 entails most of the nomenclature employed when discussing rotor blade geometry. The blade root is a thicker section, with longer chord length (distance between leading and trailing edge; the leading edge is the blade section that first encounters the inflowing air and the trailing edge is the last section of the blade) as, due to the small rotor radius, its relative wind speed is low, which causes a reduced lift (thus the need for longer chord lengths). The higher thickness is a result of the higher concentration of loads, thus, the need to ensure the structural integrity. Both the mid span and the tip are aerodynamically relevant, as these sections need to maximize the lift-to-drag ratio and slenderness, in order to cut-back on material.

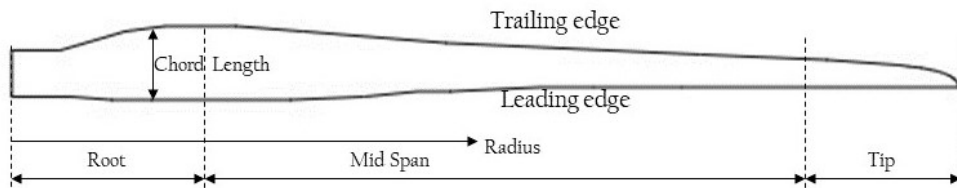


Figure 1.6: Schematic of horizontal axis wind turbine rotor blade.

Blade profiles can further be understood as sets of airfoils: cut-sections of the blade, as shown in Fig. 1.7. Note that, if one considers the blade radius, r , then the airfoil at $0,5r$ will necessarily be different from the airfoil at $0,75r$. This is exemplified by the FFA-W3-301 and DU93-W-210 airfoils in Fig. 1.7, which additionally shows the twist angle, necessary in large in wind turbines, as the incoming wind has much steeper angles close to the blade root, which twisting tries to correct to achieve optimal angles of attack.

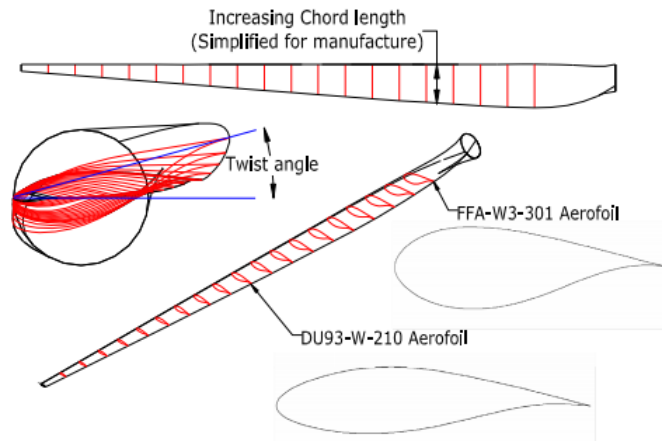


Figure 1.7: Blade Profile. Extracted from "Wind Turbine Blade Design," by P.J. Schubel and R.J. Crossley, 2012, Energies [Schubel and Crossley 2012].

It is also necessary to mention the airfoil geometry terminology, as represented in Fig. 1.8, which can be described as follows:

- Chord line - Straight line connecting the trailing and leading edge. *N.b.*, the chord is the measure of the chord line length.
- Camber line - The midway line between the upper and lower surfaces.
- Thickness - Varies throughout the airfoil. It must be noted that there are 2 conventions for its measurement: the American, which measures thickness as perpendicular to the camber line, and the British, which measures thickness as being perpendicular to the chord line.
- Camber - The asymmetry (distance) between the upper and lower surface (if there is symmetry, then camber = 0).
- Upper surface, or suction surface - Higher velocity/Lower pressure.
- Lower surface, or pressure surface - Lower velocity/Higher pressure.

The pressure difference between the lower- and upper surface generates a perpendicular force known as lift (F_l), which is the vertical component of the reaction force, F . The horizontal component is known as drag (F_d). These forces are dependent on the incoming wind velocity, c_0 and the angle of attack, α , the angle described between c_0 and the chord line.

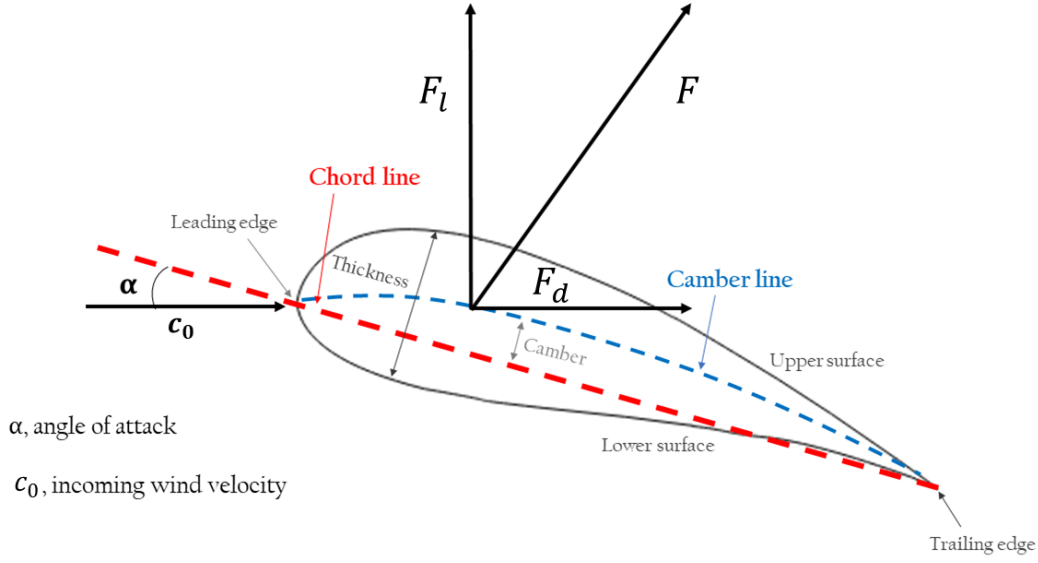


Figure 1.8: Schematic of common airfoil terminology and lift/drag forces.

Apart from the nomenclature employed when discussing wind turbine blades, one important characteristic related to the blades' geometry is the tip speed ratio, *viz.* the ratio between rotor blade velocity and the absolute velocity, as given by Eq. (1.1):

$$\lambda = \frac{\omega r}{c_0} \leq 9 \quad (1.1)$$

where, λ - Tip speed ratio.

ω - Rotational speed [rad/s].

r - Radius.

And c_0 - Absolute wind speed (local) in [m/s].

This dimensionless number is related to the blade geometry due to the inclusion of the blade radius in its formula and is essential for an appropriate rotor design, as efficiency, torque, mechanical stress and noise are all intertwined with this parameter. Higher tip speeds can lead to narrower blade profiles, as the chord lengths can be reduced, which can eventually lead to a reduction in the amount of material utilized. Nevertheless, they also induce increased aerodynamic forces, which may prove problematic when taking into account structural stability. Additionally, these higher tip speeds further increase mean noise (to the power sixth) [Oerlemans *et al.* 2007].

The tip speed ratio is a parameter which often appears when discussing wind turbines due to, as previously mentioned, the many areas in which it is employed. As such, there are numerous scientific articles concerned with this characteristic, wherein typical values for the tip speed ratio in modern HAWTs are studied, namely the maximal value of λ , which can rise up to 9 [Hau 2013].

1.3 Wind Turbine Aerodynamics and Tower Interference

Central to the prediction of performance and loads on the rotor blades (and, consequently, in airfoils, *vd.* Fig. 1.9), as well as other structures exposed to the wind, are wind turbine aerodynamics [Van Kuik and Peinke 2016], whose accurate modelling can allow improved power coefficients [Willis *et al.* 2018]. Integrated with the aerodynamic modelling are fluid-structure interactions (FSI) [Bazilevs *et al.* 2013], whose aeroelastic models are prerequisites for the design, development and optimization of wind turbines [Van Kuik and Peinke 2016]. Wind turbine aerodynamics are rather ubiquitous, influencing a myriad of parameters, from rotor blade geometry and power output [Mur-Amada and Bayod-Rújula 2007], up to entire wind farms [Kusiak and Song 2010, Wilson *et al.* 2018].

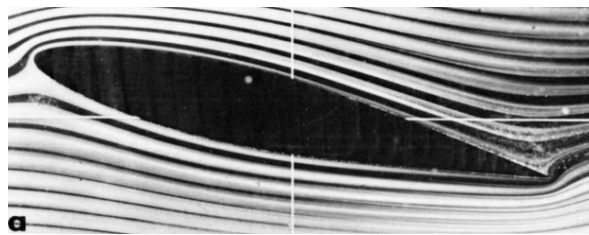


Figure 1.9: Hele-Shaw flow [Hele-Shaw 1898] past an inclined NACA 64A015 airfoil. Extracted from "An Album of Fluid Motion," by M. Van Dyke, 1982, Parabolic Press Stanford [Van Dyke 1982].

The aerodynamics of wind turbines are extremely complicated, mostly due to the unsteady nature of blade air loads, which arise from a multitude of factors, although this complexity isn't solely bounded to unsteadiness. Among others, we can identify phenomena such as atmospheric turbulence, yaw, ground boundary layer effects, directional and spatial variations in wind shear, thermal stratification, effects of an upstream unsteady, bluff body-like, wake from a support structure and blade-wake interactions as being responsible for the challenging nature of wind turbines' aerodynamics [Leishman 2002]. It is nonetheless clear that a better understanding of the aforementioned aerodynamic phenomena is critical for more efficient and lower-cost wind turbines.

Within the realm of the foregoing aerodynamic sources that may affect the air loads on a wind turbine, the effect of the tower on the flow through wind turbines' blades, also referred to as tower shadow or tower interference (hereafter mentioned as tower interference), has garnered the attention of many, particularly due to its periodicity, which has an influence in the expected lifetime.

Initially, tower interference wasn't necessarily connected with blade aerodynamics, but it was rather more closely associated with atmospheric sciences [Cermak and Horn 1968, Barthlott and Fiedler 2003] and anemometer measurements [Dabberdt 1968, Wucknitz 1977, Lubitz and Michalak 2018], but with the passing of years it has assumed a greater relevance within Wind Energy Conversion Systems (WECS).

Tower interference in upwind configurations (*vd.* Fig. 1.10) is caused by a low velocity flow field due to the presence of the tower, not being as severe as in downwind configurations where the rotor interacts with the tower wake, leading thusly to a quasi-steady aerodynamic response on the blades [Zahle *et al.* 2009].

Although a part of the literature seems to downplay the role of the tower effect in

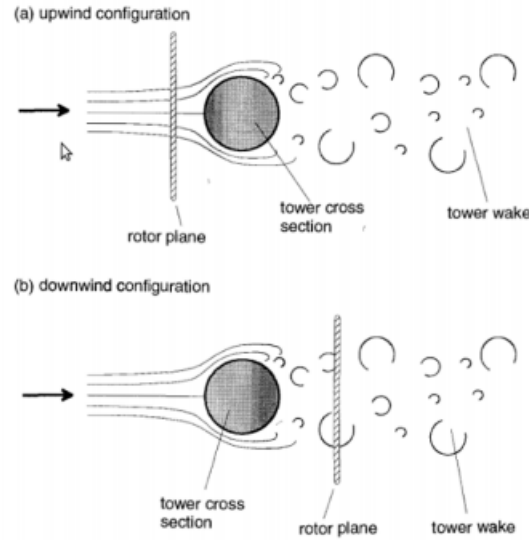


Figure 1.10: Schematic of upwind and downwind tower configurations. Extracted from "Evaluation of Tower Shadow Effects on Various Wind Turbines Concepts," by F. Zahle, H. A. Madsen and N. N. Sørensen, 2009 [Zahle *et al.* 2009].

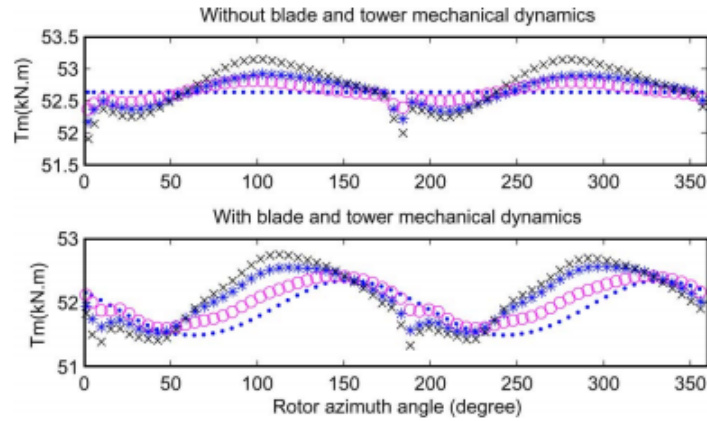


Figure 1.11: Effect of tower shadow on mechanical torque with and without blade and tower dynamics for different levels of tower interference (0 [...], 0.1 [o], 0.2 [*], 0.3 [×]). Extracted from "The Impact of Tower Shadow, Yaw Error, and Wind Shears on Power Quality in a Wind-Diesel System," by R. Fadaeinedjad, G. Moschopoulos and M. Moallem, 2009 [Fadaeinedjad *et al.* 2009].

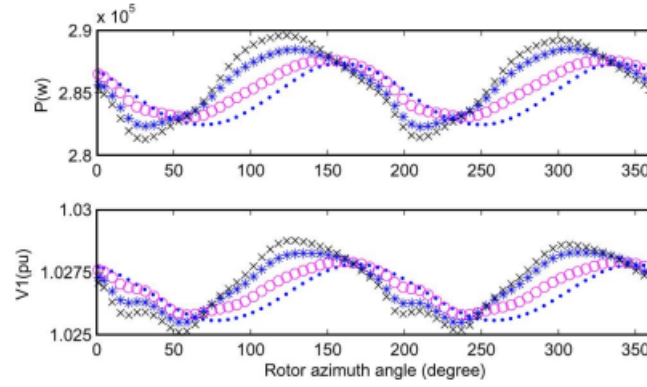


Figure 1.12: Effect of tower shadow on output power and voltage with and without blade and tower dynamics for different levels of tower interference (0 [...], 0.1 [o], 0.2 [*], 0.3 [×]). Extracted from "The Impact of Tower Shadow, Yaw Error, and Wind Shears on Power Quality in a Wind–Diesel System," by R. Fadaeinedjad, G. Moschopoulos and M. Moallem, 2009 [Fadaeinedjad *et al.* 2009].

upwind rotor wind turbines [Wang and Coton 2001], focusing mostly in wake dynamics [Eriksen and Krogstad 2017, Cline and Crawford 2010], some going as far as considering it negligible [Munduate *et al.* 2004], the effect of the tower in upwind configurations has concrete repercussions due to the low Reynolds Number, spanning from the aerodynamic torque and power output in WECS (*vd.* Fig. 1.11 and 1.12) [Dolan and Lehn 2006, Mur-Amada and Bayod-Rújula 2007, Sintra *et al.* 2014, Fadaeinedjad *et al.* 2009], to aeroelasticity [Hansen *et al.* 2006], maintenance concerns [Leishman 2002] and fatigue [Pedersen *et al.* 2012]. Its accurate modelling can provide useful insights to the wind turbine industry, wherein better predictive tools could be used to maximize wind turbine efficiency and reduce overall costs, as well as providing a better understanding of its wide ranging effects on control systems and final grid power quality.

1.4 Dynamic Stall in Wind Turbines

Wind turbines, as mentioned, face many non-linear aerodynamic instabilities, such as wind shear and turbulence, which generate a time-dependent inflow, inducing unsteady airloads. They are particularly susceptible to aerodynamic unsteadiness as, due to low rotor rpm (and subsequently, low tip speeds), these inflow instabilities can result in significant changes in the blade element's angle of attack [Pereira *et al.* 2013]. This unsteadiness must be taken into account when designing major components of wind turbines, as the correct prediction of dynamic (and even mean) loads is of the utmost importance when envisioning modern designs, where there's an ever-expanding demand for longer lifespans and tighter fatigue control. One of the sources of this unsteadiness in the inflow is precisely tower interference [Butterfield *et al.* 1991], which introduces periodical changes on the inflow conditions (alteration of the Reynolds number) and angle of attack.

An integral component in understanding dynamic airloads lies with a phenomenon commonly referred to as dynamic stall (*vd.* Fig. 1.13), which arises when there is a

sudden unsteady change on the angle of attack, where, due to turbulence and viscosity, there is a periodic massive separation of the airflow off the surface of the airfoil, followed by a reattachment.



Figure 1.13: Airflow separation from airfoil as characteristic in stall. Adapted from "Le Tunnel Hydrodynamique au Service de la Recherche Aéronautique," by H. Werlé, 1974, ONERA [Werlé 1974].

Essentially, as the separation point moves towards the leading edge, a shear layer that follows the separation point's motion is formed. This shear layer presents a formation commonly known as the Kelvin-Helmholtz instability [Thomson (Lord Kelvin) 1871, von Helmholtz 1868] (*vd.* Fig. 1.14), stemming precisely from a velocity shear. When the separation point is close enough to the leading edge, the final shear layer is formed and the Kelvin-Helmholtz instability rollers are paired up, generating a dynamic stall vortex, which, due to total vorticity conservation, means that the trailing edge stops shedding vortices.



Figure 1.14: Kelvin-Helmholtz instability of superposed streams. Both streams move to the right, but the upper one does so with a superior velocity. Adapted from "An Album of Fluid Motion," by M. Van Dyke, 1982, Parabolic Press Stanford [Van Dyke 1982].

In the last stage the dynamic stall vortex is convected downstream, as, due to the instability of the shear layer, a trailing edge vortex is formed, which bolsters the detachment of dynamic stall vortex. Even though throughout the process the lift coefficient might slightly increase, at later stages it plummets.

Although the past decades have seen an impressive rise in computational fluid dynamics capabilities and employment (the least of which to investigate the difficultly predicted unsteady aerodynamic loads which arise from the effects of dynamic stall in airfoils), the still high computational cost remains prohibitive for engineering applications. This has been traditionally surmounted through the use of empirical or semi-empirical models [Wang and Zhao 2015], based on Theodorsen's potential flow approximation to

the unsteady lift and pitching moment [Theodorsen 1935], as exemplified by ONERA's state-space model [Petot 1989], which has been adapted to wind turbines [Rapin and Ortun 2007].

Nevertheless, one of the most widely used models is Leishman-Beddoes' [Leishman and Beddoes 1989], as it has fewer empirical parameters and more explicit physical meaning [Wang and Zhao 2015], comprising of three subsystems:

1. Attached flow model for the unsteady airloads;
2. Separated flow model for the non-linear airloads;
3. Dynamic stall model for the leading edge vortex-induced airloads.

Several adaptations of the Leishman-Beddoes model have been carried throughout the years, but one of particular interest, due to its robustness, is Hansen's model [Hansen *et al.* 2004].

1.5 Betz Limit

Aside the several sources of aerodynamic unsteadiness associated with wind turbines, when discussing these technologies it is also vital to introduce the aerodynamic performance expected to be achieved by a wind turbine rotor. In order to predict said performance of wind turbine rotors the simplest model possible to be employed is the Lancaster-Betz-Joukowski law [Van Kuik 2007], more commonly known as Betz limit [Betz 1920, Betz 1926].

The application of this simple one-dimensional momentum theory, although known for providing the maximum power coefficient (Betz limit), also allows to predict, for an ideal rotor, the thrust coefficient and the rotor-induced variations on the local flow field during the extraction of energy in wind turbines (*vd.* Fig. 1.15).

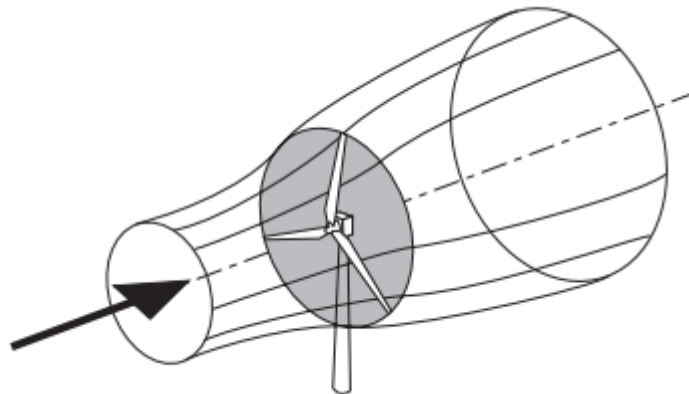


Figure 1.15: Energy extraction by stream tube in a wind turbine. Extracted from "Wind Energy Handbook," by T. Burton, D. Sharpe, N. Jenkins and E. Bossanyi, 2011 [Burton *et al.* 2011].

The first step in the analysis of the aerodynamic behaviour of a wind turbine is to consider it as an actuator disc [Froude 1889] (*vd.* Fig. 1.16), an infinitely thin disc

which models the rotor. This approach requires certain assumptions, as described by Manwell [Manwell *et al.* 2010]:

- homogenous, incompressible (ρ constant), one-dimensional, steady state fluid flow;
- no frictional drag;
- an infinite number of blades;
- uniform thrust over the disc or rotor area;
- a non-rotating wake;
- the static pressure far upstream and far downstream of the rotor is equal to the undisturbed ambient static pressure

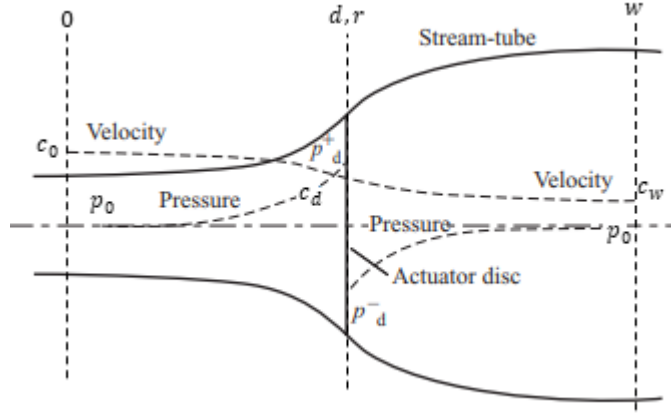


Figure 1.16: Actuator disc and stream tube. Adapted from "Wind Energy Handbook," by T. Burton, D. Sharpe, N. Jenkins and E. Bossanyi, 2011 [Burton *et al.* 2011].

As evidenced by Fig. 1.16, the stream tube suffers an expansion downstream, explained by the necessity of keeping the mass flow rate constant. Using Burton's notation [Burton *et al.* 2011]:

$$\dot{m} = \rho A_0 c_0 = \rho A_d c_d = \rho A_w c_w \quad (1.2)$$

where, 0 refers to far upstream conditions, d at the actuator disc, w at the far wake, ρ is density, A is the cross-sectional area and c is velocity. If we consider the inwards flow momentum $\dot{p}_0 = \dot{m} \cdot c_0$ (where p stands for momentum) and the outward flow momentum, $\dot{p}_w = \dot{m} \cdot c_w$ we can promptly conclude that there must be a force exerted by the turbine onto the in-flowing air and, conversely, the opposing force [Newton 1687] that the wind exerts on the wind turbine, with the same magnitude, and commonly know as thrust, T [Schaffarczyk 2014].

As such we have:

$$T = \dot{m}(c_0 - c_w) \quad (1.3)$$

this force can be understood as a pressure drop ($\Delta p = p_d^+ - p_d^- = T/A_r$, where A_r is the swept area of the rotor. *N.b.*, we can speak here of a rotor, instead of a disc, as we are concerned with wind turbines, but they are equivalent).

We can thusly apply Bernoulli's equation [Bernoulli 1738] to 2 control volumes ($0 \rightarrow d^-$ and $d^+ \rightarrow w$). For the stream tube upstream of the disc:

$$p_0 + \frac{1}{2}\rho c_0^2 = p_{d^-} + \frac{1}{2}\rho c_d^2 \quad (1.4)$$

And for the stream tube downstream of the disc:

$$p_{d^+} + \frac{1}{2}\rho c_d^2 = p_w + \frac{1}{2}\rho c_w^2 \quad (1.5)$$

If we now solve Δp using Equations (1.4) and (1.5) we obtain:

$$\Delta p = \frac{1}{2}\rho (c_0^2 - c_w^2) \quad (1.6)$$

which in turn leads us to the thrust:

$$T = \frac{1}{2}\rho A_r (c_0^2 - c_w^2) \quad (1.7)$$

Now, if one considers the mass flow rate as $\dot{m} = \rho \dot{c} = \rho A_r c_d$ and combining equations (1.3) and (1.7) we get:

$$c_d = \frac{c_0 + c_w}{2} \quad (1.8)$$

which is the same to say that the velocity in the rotor plane is the average between upstream and downstream velocities, and is also known as Froude's Law [Schaffarczyk 2014].

Additionally, we can think of the fractional decrease in the wind velocity between the free stream and the rotor plane as being induced by the actuator disc. This is commonly know as the axial induction factor, or inflow factor, a , and given by:

$$a = \frac{c_0 - c_d}{c_0} \quad (1.9)$$

There is, thus, an induced velocity at the rotor, $-a \cdot c_0$, that, when superimposed with the free stream velocity yields the velocity at the rotor. Also, it is noteworthy to consider that if $a = 1/2$, then the wind velocity post-rotor is zero, which implies that this theory is only valid for $0 \leq a \leq 1/2$.

Furthermore, Equation (1.9) allows us to additionally simplify Equation (1.8), as well as the expression for c_w :

$$c_d = c_0(1 - a) \quad (1.10)$$

$$c_w = c_0(1 - 2a) \quad (1.11)$$

As previously stated, the force on the air is:

$$T = \Delta p A_r \quad (1.12)$$

which, through further simplifications based on the conjugation of Equations (1.10) and (1.11), and considering the power output as $T \cdot c_d$, yields the final expression for the power output:

$$\dot{W} = \frac{1}{2} \rho A_r (c_0^2 - c_w^2) c_d = 2 \rho A_r c_0^3 a (1 - a)^2 \quad (1.13)$$

We can also express this nondimensionally, through the power coefficient, which represents the fraction of the power in the wind that is extracted by the rotor. It is defined as:

$$C_P = \frac{\text{Rotor Power}}{\text{Wind Power}} = \frac{\dot{W}}{\frac{1}{2} \rho A_d c_0^3} \quad (1.14)$$

Conjoining Equations (1.13) and (1.14) we obtain:

$$C_P = 4a(1 - a)^2 \quad (1.15)$$

the maximum value of C_P is attained when:

$$\frac{dC_P}{da} = 0 \quad (1.16)$$

which yields $a = 1/3$. We have, thus (for $a = 1/3$):

$$C_{P,max} = C_{P,Betz} = \frac{16}{27} = 0,593 \quad (1.17)$$

$C_{P,max}$ is also known as Betz limit, which indicates the maximum achievable power coefficient on a wind turbine rotor. This limit can be explained through the smaller area of the cross-section of the full, free stream velocity air when compared to the disc, seeing that the stream-tube must expand upstream of the actuator disc [Burton *et al.* 2011] (*vd.* Fig. 1.15). Even though real cases have always fallen under Betz limit [Aichinger 2012], to try to avoid this, diffuser augmented wind turbine models have been created, in order to increase the mass flow [De Vries 1979].

We can, finally, write the equation which gives the expected maximal power output of a wind turbine, where the influence of both the speed and rotor diameter become evident:

$$\dot{W} = \frac{16}{27} \times \frac{1}{2} \rho \left(\frac{\pi D^2}{4} \right) c_0^3 \quad (1.18)$$

with, D the rotor diameter.

Chapter 2

State-of-the-art in Predictive Methods

After being introduced to the fundamentals of wind turbines, it is now indispensable to comprehend which are the different methods employable in the study of these technologies, their applicability, advantages, disadvantages, frontier of the knowledge and previous applications concerning tower interference. As such, this chapter comprises of a short description of the different methods employed in the calculation of loads or other aerodynamic characteristics in wind turbine airfoils and a comparison of their relative advantages. However, it must be noted that a thorough knowledge of aerodynamic models on its own is insufficient to determine mechanical loads and stresses in wind turbine rotors. For this, one must consider the interaction between the turbine components' response to the loads and how this conversely influences external loads, in what is known as aeroelasticity [Snel 2003].

Three different methods (or, more accurately, classes of methods) will be presented in the ensuing sections: the Blade Element Momentum Method, which was the first method conceived, but also Computational Fluid Dynamics (CFD) and 'Engineering Methods' (EM), which have seen a growing applicability, particularly since the new millenium.

Although there have been numerous comparisons of each method, as exemplified by the influential National Renewable Energy Laboratory's (NREL) Unsteady Aerodynamics Experiment, tested in NASA Ames' wind tunnels [Simms *et al.* 2001], which has served as an important benchmark, it is important to note that these three methods aren't interchangeable and that a one-to-one comparison is impossible: they all require different amounts of inputs and return different levels of information as related to the flow and, as such, ought to be employed judiciously.

2.1 Blade Element Method (BEM)

Traditionally the primary method applied to the aerodynamic analysis of wind turbine rotors [Lackner *et al.* 2013] has been the Blade Element Momentum Method (BEM). First introduced by Glauert [Glauert 1935] as a refinement of William Froude's blade element momentum theory, it combines one-dimensional momentum theory (which doesn't take into account the rotor's geometry) with local events in blades (so-called blade element considerations) [Hansen 2015]. Some of the assumptions made by BEM are that there

is radial non-dependency (each element can be treated separately) and that, in each annular element (discretization of the 1-D Momentum Theory Streamtube), the force from the blades exerted on the flow is constant. This yields a rotor with an infinite number of blades, which is corrected by a factor known as Prandtl's tip-loss, allowing the consideration of a finite number of blades.

Essentially, the Blade Element Momentum method states that there will be a wind velocity differential between upstream and downstream (wake region); thus, there will be a momentum loss generated by locally produced axial loads by the blade passing flow, inducing a pressure difference in the blade section [Hansen *et al.* 2006].

At its core, the BEM method sets itself to determine induced velocities and thus, the local angles of attack and, provided it has values for the lift and drag coefficients, it will return the lift and drag forces, and additionally the torque and axial force. It is, nonetheless, important to comprehend that, unlike in other applications, lift can't be understood as a perpendicular force to the velocity as seen from the airfoil. To better understand this conceptualization Fig. 2.1 provides a schematic for the decomposition of lift and drag into normal and tangential forces.

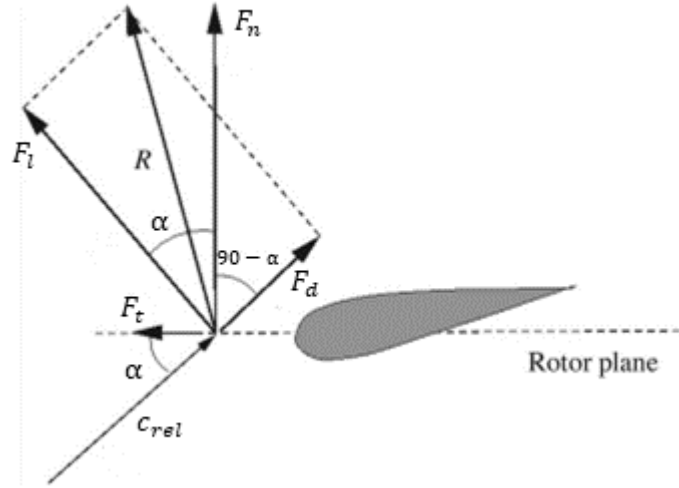


Figure 2.1: The local loads on a blade; \mathbf{R} is the vector sum of the lift and the drag. F_t and F_n are the tangential and normal components of \mathbf{R} , respectively. Adapted from "Aerodynamics of Wind Turbines," by M. Hansen, 2015 [Hansen 2015].

Nevertheless, if we consider a more simplified approach, where c_{rel} , the velocity relative to the blade section, has the same direction as c_0 , the lift and drag forces can be expressed by the Equations (2.1) and (2.2):

$$F_l = 1/2 \rho c_0^2 L C_l \quad (2.1)$$

$$F_d = 1/2 \rho c_0^2 L C_d \quad (2.2)$$

with, F_l - lift force by unit of length.
 F_d - drag force by unit of length.

ρ - density.

c_0 - incoming velocity.

L - chord (airfoil length).

For all that is aforementioned, BEM is considered a model of some simplicity, which allows it to be computationally cheap and, thus, extremely fast. However, its validity isn't universal: in the presence of strong non-axisymmetric flows the vector normal to the rotor plane isn't parallel to the wind vector, in a situation commonly referred to as yaw misalignment, which leaves the BEM method unable to provide accurate predictions [Leishman 2002]. The same happens under wake conditions, or other three-dimensional phenomena (the BEM theory is two-dimensional).

To take this into consideration, semi-empirical corrections must be made, such as Glauert's and Shen's tip correction [Sun *et al.* 2016]. Various modifications to the classical BEM model have been made, particularly to take into account unsteadiness, such as dynamic inflow or dynamic stall models, being the Unsteady Blade Element Momentum method a natural development of the classical BEM method. Due to the unsteady nature of the inflowing wind caused by atmospheric phenomena (such as gusts), wind shear and the tower's presence, an unsteady BEM method is required for realistic computations. It must be noted, nonetheless, that, for non-existing yaw misalignment, the induced velocity equations are identical to those of the classical BEM method.

The Blade Element Momentum method also requires reliable airfoil data [Hansen *et al.* 2006], and there are uncertainties related to the incorporation of nonlinear airfoil characteristics [Tangler 2002].

Notwithstanding all of its limitations, the Blade Element Momentum Method, when complemented with the necessary engineering add-ons, captures many of the physical aspects of wind turbines and the improvement of such a simplified model is a key challenge for years to come [Hansen 2015, Van Kuik and Peinke 2016].

As to implementations of BEM applied to tower interference, there have been, throughout the years, some attempts, such as Noyes *et al.* [Noyes *et al.* 2018] and Fadaeinedjad *et al.* [Fadaeinedjad *et al.* 2009], although these studied downwind configurations. Additionally, the National Renewable Energy Laboratory (NREL) aeroelastic simulation code FAST (Fatigue, Aerodynamics, Structures, and Turbulence), whose aerodynamic component AeroDyn comprises of a quasi-steady approach based on the works of Bak and Powles [Jonkman *et al.* 2015], can also be used for upwind configurations.

Another BEM-based code, this time developed by the Technical University of Denmark at Risø DTU, which includes a tower interference model, is the Horizontal Axis Wind Turbine Code (HAWC2). This aeroelastic code, written mostly in FORTRAN, but also with interfaces with other programming languages [Garzon *et al.* 2010], additionally accounts for tower interference, as described in its user's manual [Larsen and Hansen 2007].

Finally, Dolan and Lehn [Dolan and Lehn 2006] have also produced a paper in which the wind turbine tower interference in an upwind configuration is investigated, focusing mostly on the calculation of the wind speed.

2.2 Engineering Methods (EM)

The cluster of methods hereby presented are the so-called engineering methods, also known as potential flow models (the former, borrowed from J.G. Leishman [Leishman 2002], was selected as it is a more all-embracing term, but also considering that the latter expression might be confusing, as in the scope of this work the potential flow theory will be employed for another application). The engineering methods are, thus, a category of methods encompassing free and fixed vortex methods (sometimes also referred to as Prandtl's lifting-line theory [Prandtl 1918]), and panel methods (*vd.* Fig. 2.2).

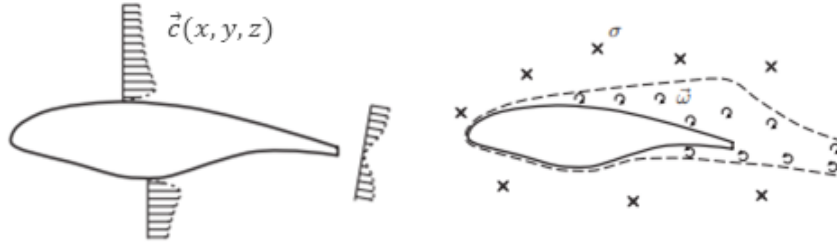


Figure 2.2: Flow field representations. Extracted from "Development of a Wind Turbine Aerodynamics Simulation Module," by A. Van Garrel, 2003, Energy Research Center of the Netherlands, ECN [Van Garrel 2003].

Essential to all of these methods is the notion that there are two possible representations of the flow field, as embodied by Fig. 2.2, which can be described either through the velocity vector, \vec{c} , or through the distribution of sources, σ , and vortices, γ , in the flow domain. Both representations are equivalent, seeing that $\sigma = \vec{\nabla} \cdot \vec{c}$ and $\vec{\gamma} = \vec{\nabla} \times \vec{c}$, but the velocity field associated with field distribution of sources and vortices is unfortunately described as "*induced* velocity" [Drela 1998]. This velocity field (with sources and vortices, presented on the right-side of Fig. 2.2) can be approximated through several methods (*vd.* Fig. 2.3).

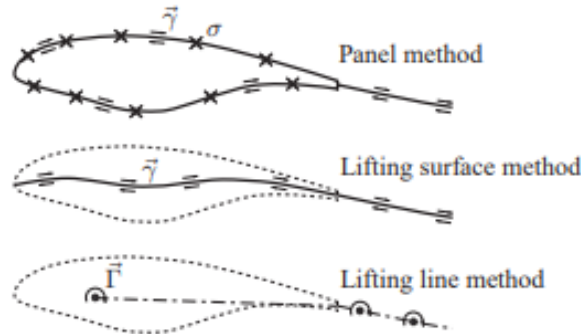


Figure 2.3: Flow field approximations. Extracted from "Development of a Wind Turbine Aerodynamics Simulation Module," by A. Van Garrel, 2003, Energy research Center of the Netherlands, ECN [Van Garrel 2003].

2.2.1 Lifting-Line Theory

The first of these methods to be presented is the lifting line method, which has been widely applied since its early inception in the beginning of the twentieth century by Lanchester [Lanchester 1908] and Prandtl [Prandtl 1918] (The lifting surface method won't be discussed in this work; for further information see Kerwin [Kerwin 2001]). Essentially, it applies Prandtl's lifting line theory, where it is stated that, instead of a spanwise lift distribution, one might represent this as spanwise circulation (Γ) distribution. So, the lift generated locally by flow past the blades induces a bound circulation which allows us to determine the blade vortex strength. The relationship between the bound circulation and the lift is given by the Kutta-Joukowski theorem [White 2011], as given by Eq. (2.3):

$$F_l = \rho c_0 \Gamma \quad (2.3)$$

with, c_0 - velocity.

Γ - circulation.

ρ - density.

F_l - lift force by unit of length (when lift is mentioned, it is always implied that it is by unit of length).

It is important to note that here lift isn't a vertical force when one takes into account the entirety of the wind turbine, as it is usually considered. When applied to Prandtl's lifting-line theory in wind turbines, Eq. (2.3) becomes:

$$F_l = \rho c_{Rel} \Gamma \Rightarrow \Gamma = 1/2 c_{Rel} F_l C_l \quad (2.4)$$

with, c_{Rel} - velocity relative to the blade section.

L - chord.

C_l - lift coefficient.

Additionally, if one possesses the knowledge of the strength and position of the vortices, among other variables, such as the line's Dirac delta, δ , the induced velocity can be discovered through the Biot-Savart Law [Branlard and Gaunaa 2015]. In some models, bound circulation is found through airfoil data table look-up (just like in the BEM method).

2.2.2 Panel Methods

It is also possible to obtain the integral representation of the potential flow field with regard to the singularity of distribution [Hansen *et al.* 2006], as stated by Green's Theorem [Green 1828]. This allows the potential flow solution of an airfoil to be modeled as the discretization of the surface contour through the use of panels (there isn't one sole technique, but rather, several different configurations).

Essentially, panel methods execute two separate calculations: the inviscid panel method that predicts flow velocities/pressure, and the viscous boundary layer theory that predicts surface flow displacement and friction-induced momentum loss (the most

accurate would be to iterate the results of both solutions, but due to numerical difficulties, this isn't always followed).

Following the panel discretization configuration as presented in Fig. 2.4, based on straight (between the surface points j and $j + 1$) panels with a linear distribution of vorticity (of strength γ_0) between end points (γ_{j+1} and γ_j) and defined free stream conditions (c_0 , velocity, and α , angle of attack), a simplified panel method calculation procedure is exemplified (for greater detail, see Brederode [Brederode 2014]).

This method requires certain boundary conditions, such as no flow through the surface at the center of each panel ($c_{s,j} = 0$, which produces N equations, requiring the imposition of a Kutta condition at the trailing edge [Kutta 1910]).

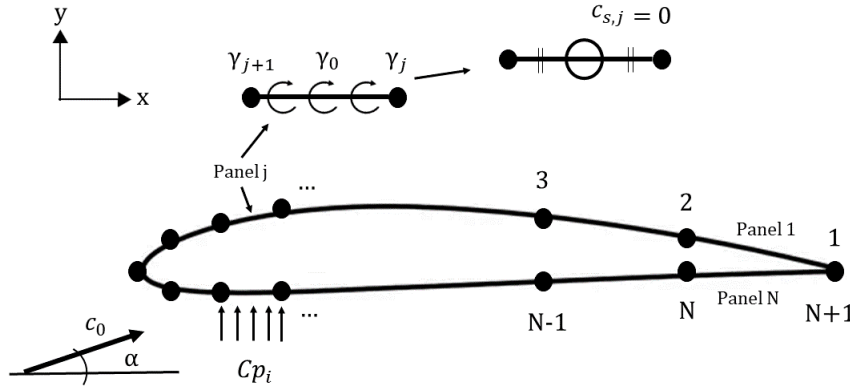


Figure 2.4: Inviscid panel method airfoil discretization. Adapted from "2D Panel Methods," by Aerodynamics for Students, 2019 [Aerodynamics for Students 2019].

An additional boundary condition can be described by Eq. (2.5), at panel i :

$$c_s = \sum_{j=1}^{N+1} (A_{ij} \cdot \gamma_j) + B_i c_0 = 0 \quad (2.5)$$

with, A_{ij} - influence of vorticity components on panel j on the control point on panel i . B_i - Influence of the free stream on panel i . This will lead to a system of linear equations whose solution is the distribution of strengths, which allows the calculation of surface tangential velocities at the center of the panel (c_i) and the surface pressure coefficients (Cp_i), with:

$$Cp_i = 1 - \frac{c_i^2}{c_0^2} \quad (2.6)$$

In addition, assuming a small α , and L , the airfoil's chord, the lift and moment coefficients (which will be the sum of the panel moments about the 1/4 chord point) can be calculated:

$$C_l = \sum_{i=1}^N C_{p_i} \cdot \frac{(x_i - x_{i+1})}{L} \quad (2.7)$$

$$C_m(1/4L) = \sum_{i=1}^N C_{p_i} \cdot \frac{(x_i - x_{i+1})}{L} \cdot \left(\frac{(x_{i+1} + x_i)}{2L} - \frac{1}{4} \right) \quad (2.8)$$

Engineering methods' (EM) popularity has drastically risen within the wind turbine aerodynamic analysis community in the last decade because they present several advantages when compared to classical BEM-, or CFD-methods, particularly their modularity, allowing the inclusion of a myriad of validated sub-component models of difficultly modelled physical effects. An example would be the use of Wagner's function or Küssner's function [Marzocca *et al.* 2001] which, coupled with Duhamel's superposition, models tower interference as a gust normal to the blade-chord, providing a transient lift [Munduate *et al.* 2004] (it takes into account the unsteadiness). Many phenomena such as stall and unsteady aerodynamics are usually modelled semi-empirically, which means table look-ups and simplified equations, but with this approach, sub-component validation is possible, as well as its further upgrade when a deeper understanding of the underlying physics is provided. Engineering methods, thus, capture most of the critical physics without the necessity for semi-empirical corrections (such in BEM) or the high computational costs of computational fluid dynamics, embodying a compromise between them [Lackner *et al.* 2013].

Nevertheless, some issues arise with this class of models, such as the correct coupling of the different sub-component models. Another drawback is that, even though engineering methods are computationally cheaper than computational fluid dynamics, they are, by no means, inexpensive when compared to BEM (even though their results should be, in principle, better) [Leishman 2002]. Also, these models face difficulties when trying to simulate the generation of loads and vorticity over the rotor blade, or when including the diffusion of the wake and the interaction between multiple wakes and with the atmospheric boundary layer [Van Kuik and Peinke 2016].

Even though engineering methods are usually applied without a tower interference model [Cline and Crawford 2010], they have also been applied in tower interference scenarios with good results, be it in Vertical Axis Wind Turbines (VAWTs), as in the case of Simão Ferreira [Ferreira 2009], or in downwind HAWTs, as exemplified by Munduate and Coton [Munduate *et al.* 2004] or Chattot [Chattot 2008], but also in upwind configurations, in the case of the latter [Chattot 2006].

Nevertheless, as evidenced by some authors [Cline 2011], engineering methods require further validation and their development has been one of the primary efforts of the wind turbine aerodynamic analysis community over the last two decades.

2.3 Computational Fluid Dynamics (CFD)

The final method being presented is also, as aforementioned, usually regarded as the one possessing the higher-fidelity (when compared to BEM and EM), known as Computational Fluid Dynamics (CFD). Although one can only speak of a dissemination in the adoption of CFD within recent decades, its earliest developments can be traced back

to the 1920's with Lewis Fry Richardson's finite differences and divided physical space in cells calculations [Richardson 2007], which, although failing spectacularly, resembles modern CFD in its methodology. Despite initial developments, it is just in the 1960's that the first computers model fluid flows, specifically as in the work of Los Alamos National Lab's T3 group, which in a short span of time developed a myriad of fluid flow simulating numerical methods [Harlow 2004], and is nowadays considered a seminal pivoting point for CFD.

In spite of its rich history and high number of different methods and models, CFD methods can be generally described as presenting the numerical solutions of either the Navier-Stokes [Schlichting and Gersten 2016] or the Eulerian [Tietjens and Prandtl 1957] equations through the use of a grid, with the latter being simplified Navier-Stokes equations through the removal of the viscous terms. If we further removed the vorticity-related terms, we would attain the potential flow equations, which will be discussed in detail in Chapter 5. Thus, based on these equations and the discretization of the physical space, the results CFD attains are usually consistent and physically realistic, surpassing BEM's capabilities in many cases [Sørensen and Kock 1995]. However, CFD still faces many challenges, particularly turbulence (even though Reynolds Averaged Navier-Stokes, RANS, as with $k-\varepsilon$ [Launder and Spalding 1983] and $k-\omega$ SST [Menter 1993] and models, among others, have tried to tackle this issue) and separation, as in dynamic stall and vortical wake.

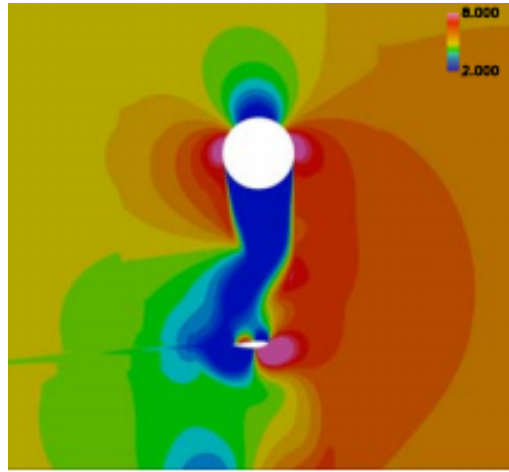


Figure 2.5: Snapshot of axial velocity. Extracted from "Evaluation of Tower Shadow Effects on Various Wind Turbines Concept," by F. Zahle, H. A. Madsen and N. N. Sørensen, 2009 [Zahle *et al.* 2009].

As computational process capacities have exponentially increased in the last decades, so has CFD's capabilities and process speed. Nonetheless, Moore's Law [Moore 1965], that used to define future generation processors scaling has been redefined to a more conservative outlook [DeBenedictis 2017, Kahng 2010], which might mean a limited growth-rate for these methods.

Regardless of future computational developments, large-volume calculations (as in full turbine geometry), aeroelastic computation and design of wind turbines are still far from CFD's reach, due to its great computational costs (*i.e.* CFD is rather slow when

compared to other models). It must be additionally noted that, even though much hope is delegated to CFD, as of this moment, computational costs aren't the sole hindrance. Some literature suggests that the solutions attained by CFD aren't always the best for certain particular cases [Morgado *et al.* 2016].

Additionally, for tower interference, there have been successful implementations of CFD models that gave interesting insight into very specific phenomena [Lin and Shieh 2010, Yu and Kwon 2014], allowing the study of aerodynamic details of the rotor, such as the blade tips and the root section [Hansen *et al.* 2006], but when considering more generalized investigations, this method often achieves results similar to BEM or engineering methods, with an increased computational cost.

Within the multiple articles delving into tower interference whose methodology applies CFD, two articles from A. Gómez and J. Seume [Gómez and Seume 2009a, Gómez and Seume 2009b] are central for the understanding of the potentialities of CFD when applied to tower interference, and can serve as trustworthy benchmarks due to CFD's expected high accuracy.

2.4 Comparison

Having presented the three main methods applied in the calculation of airloads on turbine rotors, it is now crucial to perform a comparative analysis of each one, which Table 2.1 resumes through the advantages and disadvantages of each model, as well as applicability.

Table 2.1: Comparison of different methods

Method	Advantages	Disadvantages
BEM	Computationally cheap Fastest code Predicted longevity Captures most of the crucial physical phenomena	Undesirable under yawed conditions Unsuitable for 3-D phenomena Requires reliable airfoil data Requires semi-empirical corrections
CFD	Usually gives best results Great margin of improvement Higher fidelity	Computationally expensive Difficulties in turbulence and separation Unsuitable for full-geometry calculations
EM	Computationally cheaper than CFD No need for semi-empirical corrections (sometimes) Modularity of sub-components	Computationally more expensive than BEM Correct coupling isn't always possible Still face aerodynamic difficulties

That said, some caveats must be made. For one, the previous sections must be regarded as making one unified statement: there isn't one model that can affirm its results

are universally valid (even though Navier-Stokes solvers offer the most exact solution in the majority of situations), which requires a judicious selection of which model one must implement. Although all methods are capable of offering information as related to the loads on the turbine rotor, they all have different input needs and the amount of end-information varies: Rotor performance is mainly calculated through BEM, but the lift and drag coefficients can't be obtained through this model and, while both EM and CFD provide the lift and drag coefficients, CFD offers information related to an entire volume, whereas EM solutions, depending on the method, are related to either a line or a surface which intends to approximate the airfoil's geometry.

Additionally, it is the author's belief that a hermetic perception of the models might be prejudicial. Last years have seen a greater coupling of different methods, interweaving high- and low-fidelity models [Van Kuik and Peinke 2016]. Hence CFD in conjunction with experiments has been used to improve basic understanding of the very complex aerodynamic phenomena, such as rotating lifting structures, for example, which leads to improved 'engineering methods' models of the classical BEM-based codes [Snel 2003, Sant 2007]. An example of a CFD- and experiment-induced improvement would be the semi-empirical Leishman-Beddoes model for dynamic stall, whose classical model didn't account for a trailing-edge vortex [Wang and Zhao 2015].

As an example, one could take Gómez and Seume's correction of the traditional BEM methods (whose implementation was done through an in-house Matlab developed code, Windkast) for tower interference through the use of 2D CFD simulations [Gómez and Seume 2009a, Gómez and Seume 2009b]. As evidenced by Fig. 2.6, the new model allows a corrected calculation of the flapwise bending moment at the blade root, being the result of the integration of the element loads (*N.b.* the azimuth represents the 360° blade rotation, with the tower present at 90°).

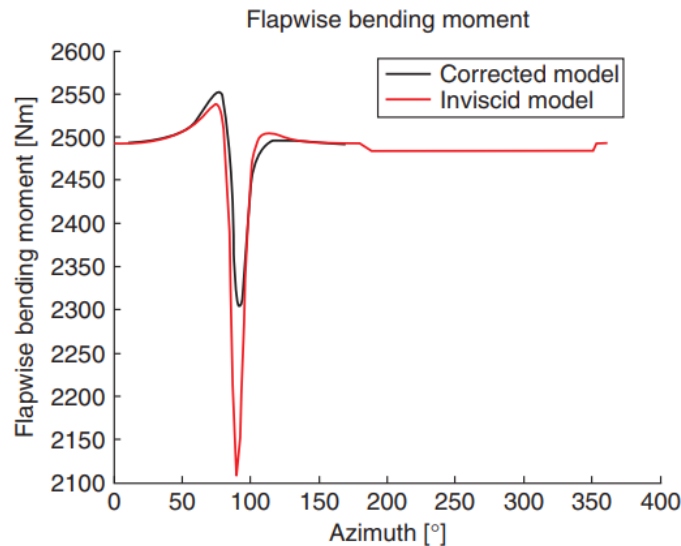


Figure 2.6: Comparison of the flapwise bending moment for the test blade calculated using the original BEM code and the corrected one. Extracted from "Load pulses on wind turbine structures caused by tower interference," by A. Gómez and J.R. Seume, 2009 [Gómez and Seume 2009b].

Perhaps the most crucial comparative study between different tower interference models based on the different predictive methods is Lackner [Lackner *et al.* 2013], referred to as Tower Interference Models (TIM), where 2D and 3D engineering method-based codes, as well as BEM codes, such as AeroDyn, are placed in comparison. CFD wasn't, naturally, used, seeing that the calculations involved the entirety of the turbine's tower geometry. The results obtained for the attachment point and induced velocity are shown in Fig. 2.7 and Fig. 2.8, respectively, where the vertical position is related to the tower position.

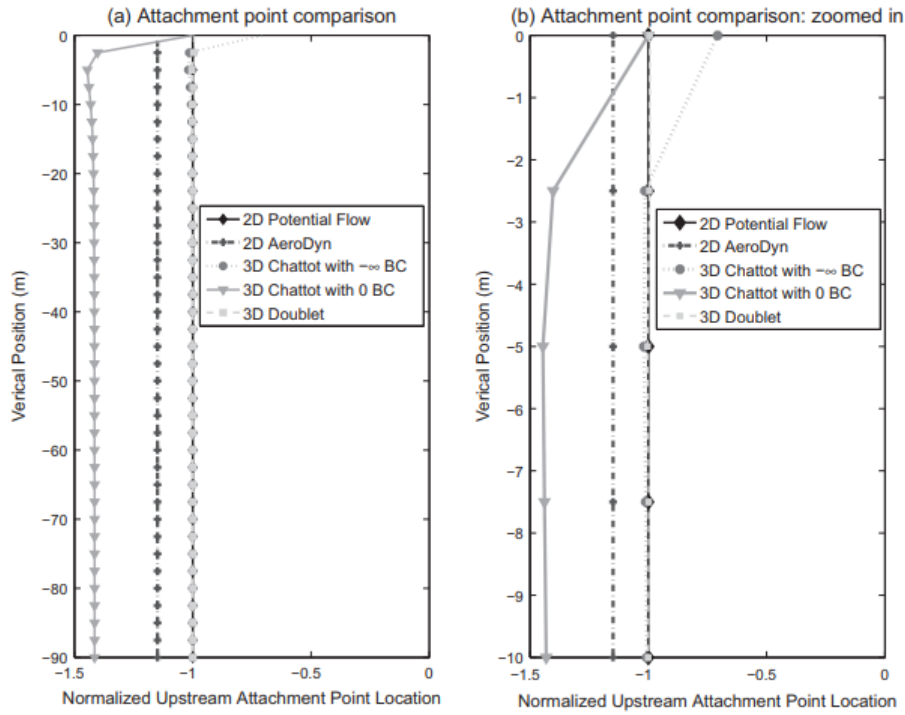


Figure 2.7: Location of attachment point for different TIMs. Extracted from "On 2D and 3D potential flow models of upwind wind turbine tower interference," by M.A. Lackner, N. deVelder and T. Sebastian, 2013 [Lackner *et al.* 2013].

Lackner [Lackner *et al.* 2013] sums his results as pointing towards the superfluous nature of 3D tower interference models, given that these present identical results to 2D models in regions of interest and are, withal, much more computationally intensive and with a difficult implementation, whilst, at the same time, not taking into account the presence of the nacelle.

Additionally, it stated that the main issue with the BEM-based code, AeroDyn, be it in the over-prediction of the attachment point or of the induced velocity, was due to the additional drag term. Nevertheless, AeroDyn's results are in no manner antithetical to the ones obtained with other TIMs. In this regard, it would be desirable to understand the cost/benefit relationship between computationally cheaper BEM codes and their EM counter-parts.

Finally, when looking at overarching research being carried through, the current trend seems to be the improvement/enlargement of low fidelity models (BEM based) with either high fidelity- (CFD) or intermediate fidelity-models add-ons (engineering methods, such

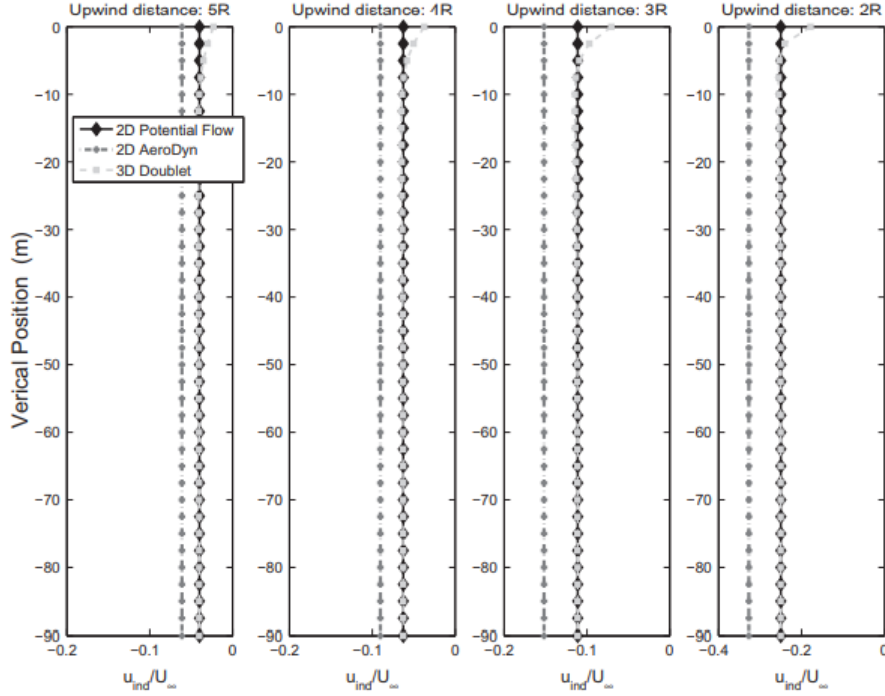


Figure 2.8: Induced velocity in the x -direction for various TIMs. Extracted from "On 2D and 3D potential flow models of upwind wind turbine tower interference," by M.A. Lackner, N. deVelder and T. Sebastian, 2013 [Lackner *et al.* 2013].

as free vortex) [Scheepers *et al.* 2018], or the direct implementation of intermediate fidelity-models.

For all of the aforementioned characteristics of each method, their advantages and disadvantages, it quickly becomes apparent that BEM can not be used for the current application, as the calculation of the lift and drag coefficients is an integral part of the present work, but also that CFD isn't an adequate method, as it is computationally too expensive and its employment isn't really justified by the requirements of this thesis (especially when considering a quasi-steady approach). Therefore, an Engineering Method ought to be select, with the choice falling upon a panel-based method known for its robustness, XFOIL (later address in Chapter 6).

Chapter 3

Objectives and Lecture Guide

The main objective of the work developed in the scope of this thesis is to investigate the upstream influence the presence of the tower has on the flow on the blade section aerodynamics, employing simplified methods entailing a quasi-steady approach. This influence is to be quantified through coefficients that relate to the main forces taking place in the airfoil of a wind turbine's blade. We can, subsequently, define in broad lines the objectives of this work:

- Identify the main mechanisms and effects concerning aerodynamic tower-rotor interference for HAWTs based on an extensive literature search.
- Distinguish the different methods applicable to wind turbine aerodynamic computations, their respective advantages and specific areas of applicability.
- Perform a dimensional analysis in order to identify the main parameters of influence.
- Develop, implement, validate and discuss a generic 2D model that calculates the upstream effect of the tower as a circular cylinder.
- Use the program XFOIL, automating the end-result attainment process, to study the upstream effect of the tower flow on the blade section aerodynamics.

This thesis is comprised of five main parts, which are summarily described below, as to provide the reader with a helpful lecture guide.

Part I — Introduction and Background In this part an introduction to wind turbines is made, emphasizing its importance on the modern world and spanning through most of the main nomenclature and physical phenomena expected to be found in these structures. These fundamentals of geometry and aerodynamics are gradually expanded in complexity until a thorough overarching literature review is presented, with a distinct focus on tower interference implementations. The objectives of the study, as well as a lecture guide, are additionally provided.

Part II — Software and Methods In the second part of this document the different methods and software (MATLAB, XFOIL, QBLADE) are presented, with a particular attention to a firm physical and mathematical background and formulation.

The methodology employed in the establishment of these tools, which will later be the base for the developed model, is also described in detail, alongside with a progressive validation and critique of such methods and methodology.

Part III — Model and Results This part contains the actual implemented model, where some methodological aspects are also discussed, as to enable an accurate understanding of the outputs, which also are presented in this part, under the Results section. As required, model validation is performed in several steps of the process, and the results of these validations, together with the comprehensive final results, are discussed in depth. These also include enhancements to the original model, as with Bak's model, and enlargements of scope of the study of the original model, as with the variations in the twist angle.

Part IV — Discussion In this part the results are compared to the reference literature and debated in relation to their verisimilitude and shortcomings.

Part V — Conclusions In this final section the main conclusions withdrawn from the work carried through in the present thesis are provided. Lastly, an outlook on possible future directions of research on the subject is presented.

Part II

Software and Methods

Chapter 4

Dimensional Analysis

One of the most powerful tools at the disposal of engineers and scientists and whose employment, although not adding anything new, is relevant in the scope of this work, as it will greatly simplify the analysis and understanding of the end-results, is dimensional analysis, whose main motivation factor is the possibility of reducing large data outputs to a set of curves, or even to one single curve, when properly nondimensionalized [White 2011].

In very plain terms, dimensional analysis attempts to reduce the number and complexity of variables necessary to the description of given problems/physical phenomena. If we possess n variables, dimensional analysis will reduce them to k dimensionless variables, *i.e.*, the reduction is $n - k = 1, 2, 3, \dots$, depending on the complexity of the problem [White 2011]. If $n - k = 1$, then we have a single curve.

From dimensional analysis we obtain dimensionless numbers. These numbers are algebraic expressions, such as fractions, where the total physical dimension is equal to the unity [Ruzicka 2008].

In the beginning of Spurk's *Dimensionsanalyse in der Strömungslehre* [Spurk 2013], the following citation from Hershey [Hersey 1966] introduces us to dimensionless numbers: "The magic numbers in the engineering sciences today are the dimensionless numbers". Indeed, their usefulness is vast, not only greatly simplifying equations and reducing the number of necessary variables, but also contributing with physical explanations to the understanding of the phenomena under study.

When describing the physical world and phenomena we can speak of seven fundamental physical quantities (measured by their corresponding units), from which all other quantities are derived [Ruzicka 2008]. These are: mass, length, luminous intensity, temperature, time, electrical current and amount of substance, measured in kilogram, meter, candela, kelvin, second, ampere and mole, respectively. In fluid mechanics the physical quantities usually involved are mass M , length L , time T and occasionally, temperature θ , more commonly known as the $MLT\theta$ system. Sometimes the $FLT\theta$ system is alternatively used, with F , force, replacing mass.

4.1 Buckingham's Π -Theorem

A powerful dimensional analysis tool that allows the attainment of dimensionless groups [Brederode 2014] is Buckingham's Π -theorem [Buckingham 1914], wherein a procedure

to determine dimensionless groups (Π , power products) is prescribed, which is shortly described in the following steps:

1. List and count all variables (be them dependent, independent or already dimensionless), obtaining the total number of n variables.
2. List the primary dimensions of the n dimensions, using either the $MLT\theta$ or $FLT\theta$ system.
3. Find the number of repeating variables j , usually the number of primary dimensions involved in the problem. Thus, the number of dimensionless variables expected will be $k = n - j$.
4. Select of the repeating variables, which appear in each Π -group. Though this selection might be somewhat arbitrary, it is nonetheless suggested to adopt the ensuing good practices:
 - Not to select the dependent variable.
 - All primary dimensions should be represented.
 - The repeating variables shouldn't form a Π -group on themselves.
 - Variables with the same dimensions (or just changing in exponent) shouldn't be selected.
 - Dimensionless variables shouldn't be selected.
 - Choose the variables with simplest, more basic dimensions.
5. Formulation of the Π -groups. These are formed by multiplying the j repeating variables, each raised to an unknown exponent, found by making the Π to be dimensionless, by the remaining variables. Some common practices are:
 - Start with the dependent variable.
 - Readjust the Π -groups to fit into the literature's pattern, such as adding factors, exponents or inverting the fraction.
6. Finalize the Π -groups' formulation by putting the first Π -group as a function of the others.

4.2 Application on the Tower of a Wind Turbine

If one considers the tower of a wind turbine as being essentially a circular cylinder, then the analysis of the flow through a circular tower, can be performed through the application of dimensional analysis to 4 important variables that seem to be at play (*vd.* Fig. 4.1), namely:

- Incoming velocity, c_0 .
- Air density, ρ .
- Dynamic viscosity, μ .

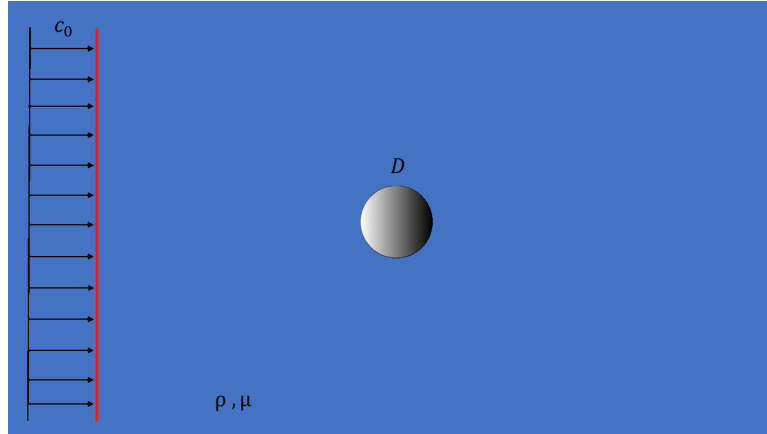


Figure 4.1: Schematic of variables involved in a flow through a circular tower.

- Tower diameter, D .

After identifying the variables, we can revert to Section 4.1 and follow its prescriptions as to apply Buckingham's Π -theorem:

1. $F = f(c_0, \rho, \mu, D)$ which yields $n = 6$. *N.b.*, F represents a force.

	Variable	Units
	F	MLT^{-2}
2.	c_0	MT^{-1}
	ρ	ML^{-3}
	μ	$ML^{-1}T^{-1}$
	D	L

3. Seeing that the primary dimensions involved in the problem are M, L and T we have that $j = 3$, which yields $k = n - j = 6 - 3 = 3$. Thus, we are expecting 3 or less Π -groups.
4. We do not select the dependent variable, F , nor the dynamic viscosity, μ , seeing that, from the remaining variables, they are the less basic.
5. Construction of the Π -groups.

The first Π -group will be:

$$\Pi_1 = F(c_0)^a \rho^b D^c \quad (4.1)$$

From which:

$$\left\{ M^0 L^0 T^0 \right\} = \left\{ \left(\frac{ML}{T^2} \right) \left(\frac{L}{T} \right)^a \left(\frac{M}{L^3} \right)^b (L)^c \right\}$$

Yielding the set of equations:

$$\begin{cases} 0 &= 1 + b \\ 0 &= 1 + a - 3b + c \\ 0 &= -2 - a \end{cases} \quad (4.2)$$

The solution of Eq. (4.2) gives us the exponents: $a = -2$, $b = -1$ and $c = -2$, thus Eq. (4.1) becomes:

$$\Pi_1 = \frac{F}{(c_0)^2 \rho D^2} \quad (4.3)$$

Following the same steps, but with

$$\Pi_2 = \mu (c_0)^a \rho^b D^c$$

gives us:

$$\Pi_2 = \frac{\mu}{c_0 \rho D} \quad (4.4)$$

We can invert Eq. (4.4) to a more common form:

$$\Pi_2 = \frac{c_0 \rho D}{\mu} \quad (4.5)$$

6. Finally, we have:

$$\frac{F}{c_0^2 \rho D^2} = \text{function of} \left(\frac{c_0 \rho D}{\mu} \right)$$

Π_2 is a dimensionless number extremely important in fluid mechanics, known as Reynolds number [Reynolds 1883], which gives valuable information regarding the behaviour of the flow of newtonian fluids:

$$Re = \frac{c_0 \rho D}{\mu} \quad (4.6)$$

4.3 Dimensionless Numbers

The methodology previously exemplified in Section 4.2 can be applied to a myriad of different variables, yielding several different dimensionless numbers: Table 4.1 duly performs a quick resume of some of the most important dimensionless numbers in fluid mechanics, although many others exist (such as Eötvös number [von Eötvös 1910] or Rossby number [Warn *et al.* 1995]).

Nevertheless, as stated by White (2011) [White 2011]: "If there is no free surface, Fr, Eu, and We drop out entirely, except for the possibility of cavitation of a liquid at very

Table 4.1: Dimensionless groups.

Number	Formula	Physical Meaning
Reynolds	$Re = \frac{\rho c L}{\mu}$	Ratio between inertial forces and viscous forces.
Froude [Hager and Castro-Orgaz 2016]	$Fr = \frac{c^2}{gL}$	Ratio between inertial forces and gravitational force. Only relevant in free-surface flows.
Weber	$Wb = \frac{\rho c^2 L}{\gamma}$	Ratio between inertial forces and surface tension. Only relevant in free-surface flows.
Strouhal [Strouhal 1878]	$St = \frac{\omega L}{c}$	Ratio between oscillation and mean velocity. Only relevant in oscillating flows.
Euler	$Eu = \frac{p_0 - p_w}{\rho c^2}$	Ratio between the pressure and inertial forces. Characterizes energy losses in the flow (p_0 and p_w are the upstream and downstream pressures, respectively).
Cavitation number	$Ca = \frac{p - p_v}{\frac{1}{2} \rho c^2}$	Ratio between the difference of a local absolute pressure from the vapor pressure and the kinetic energy. Characterises the potential of the flow to cavitate (phenomenon in which sudden changes of pressure lead to the formation of small vapor-filled cavities)
Pressure Coefficient	$C_p = \frac{p - p_0}{\frac{1}{2} \rho c^2}$	Ratio between static and dynamic pressures.
Lift Coefficient	$C_l = \frac{L}{\frac{1}{2} \rho c^2 A}$	Ratio between lift and dynamic forces. Relevant for airfoil.
Drag Coefficient	$C_d = \frac{D}{\frac{1}{2} \rho c^2 A}$	Ratio between drag and dynamic forces. Relevant for airfoil.

small Eu . Thus, in low-speed viscous flows with no free surface, the Reynolds number is the only important dimensionless parameter."

4.4 Reynolds Number in Wind Turbines

Concerning the most common Reynolds numbers found when considering wind turbines, these can range widely, from 3×10^3 to 3×10^4 (approximately) in the case of very small scale wind turbines [McTavish *et al.* 2013], up to a massive value of 25×10^6 in the case of a putative 20 MW wind turbine (which, with the increase in size of the wind turbine rotors, isn't far-fetched) [Ceyhan 2012].

It ought to be noted that these values for the Reynolds number are attained when in characteristic length, L_{char} (simply defined as L in Tab. 4.1), considered is the airfoil's

chord length, $L_{char} = L$. As such:

$$Re = \frac{\rho c L_{char}}{\mu} = \frac{\rho c L}{\mu} \quad (4.7)$$

Ignoring extreme values, when considering most commercial wind turbines one can speak of a Reynolds number ranging from 10^6 to 10^7 [Ge *et al.* 2014]. Nevertheless, with the evolution of the industry (*vd.* Fig. 4.2), it is increasingly prevailing to encounter wind turbines operating under Reynolds numbers above 10^7 [Pires *et al.* 2016].

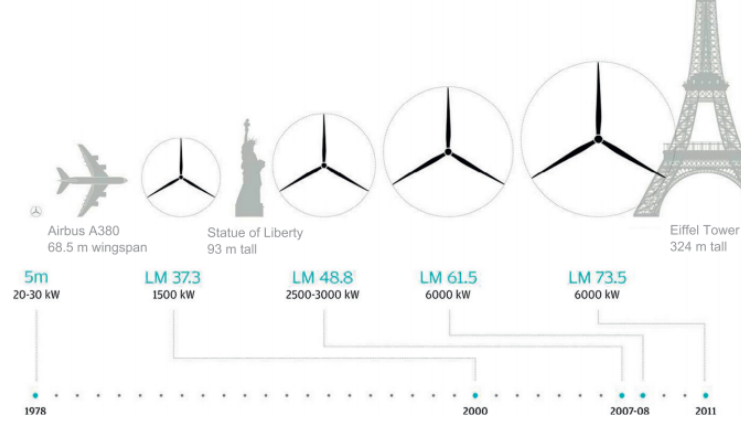


Figure 4.2: Evolution of wind turbine rotor blades. Extracted from "Design of a fibrous composite preform for wind turbine rotor blades," by J. Zangenberg, P. Brøndsted and M. Koefoed, 2013 [Zangenberg *et al.* 2014].

This increase has positive impact on the aerodynamic response of the airfoil as, for high Reynolds numbers, there is a decrease on the drag-coefficient and, conversely, an increase on the lift coefficient, resulting on a larger lift-to-drag ratio (*vd.* Fig. 4.3 in which the optimal $\alpha \approx 5^\circ$); all these factors result in a better airfoil performance [Ge *et al.* 2014].

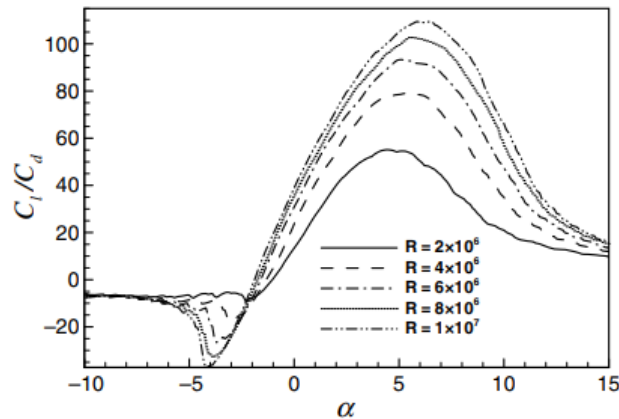


Figure 4.3: Lift-to-drag ratio for a DU00-W2-401 airfoil. Extracted from "Reynolds number effect on the optimization of a wind turbine blade for maximum aero-dynamic efficiency," by M. Ge, D. Tian and Y. Deng, 2014 [Ge *et al.* 2014].

Chapter 5

Potential Flow Theory

5.1 Theoretical Background

An essential component of the predictive tools employed to determine the loads induced onto Wind Energy Conversion Systems (WECS), particularly when considering the effect of the tower, is the modelling through the use of the potential flow theory. Even though presenting an outlook that does not reflect the actual physical reality, as actual fluids aren't frictionless, it is still highly valuable for such applications [Sørensen *et al.* 2002]. Several books have been solely dedicated to potential theory applied to fluid mechanics, such as Wermer [Wermer 1981] or Ransford [Ransford 1995], but the methodology carried through will be based mostly on White [White 2011].

Assuming that the changes of pressure in the flow are sufficiently small, we can assume that the density, ρ , is constant; this assumption characterises an incompressible flow [Brederode 2014]. In the particular case of a frictionless (viscous effects are neglected) and irrotational (at low-speeds) flow [White 2011], the momentum equation for a newtonian fluid with constant density and viscosity (Eq. (5.1)), the incompressible flow Navier-Stokes equations, which are second-order nonlinear partial differential equations, is reduced to Euler's equation for inviscid flow (Eq. (5.2)).

$$\rho \frac{d\mathbf{c}}{dt} = \rho \mathbf{g} - \nabla p + \mu \nabla^2 \mathbf{c} \quad (5.1)$$

$$\rho \frac{d\mathbf{c}}{dt} = \rho \mathbf{g} - \nabla p \quad (5.2)$$

with, ρ - density.

\mathbf{c} - velocity vector.

p - pressure.

μ - dynamic viscosity.

\mathbf{g} - body acceleration vector acting on the continuum (such as gravity).

∇ - differential operator, known as nabla, $\nabla = \frac{\partial}{\partial x} + \frac{\partial}{\partial y} + \frac{\partial}{\partial z}$ (gradient).

∇^2 - Laplacian, $\nabla^2 = \nabla \cdot \nabla$ (divergence of the gradient).

The acceleration term can be subdivided as follows:

$$\frac{d\mathbf{c}}{dt} = \frac{\partial \mathbf{c}}{\partial t} + (\mathbf{c} \cdot \nabla) \mathbf{c} \quad (5.3)$$

The second term exhibits the following vector identity [Aris 1989]:

$$(\mathbf{c} \cdot \nabla) \mathbf{c} = \nabla(\tfrac{1}{2}c^2) + \xi \mathbf{c} \quad (5.4)$$

with, $\xi = \text{curl } \mathbf{c}$, fluid vorticity, also known as rotational ($\text{rot } \mathbf{c}$ or $\nabla \times \mathbf{c}$).

If we combine Eq. (5.2), (5.3) and (5.4), divide by ρ and integrate along a streamline of an irrotational flow ($\vec{\xi} = 0$) we get, for any two points 1 and 2:

$$\int_1^2 \frac{\partial c}{\partial t} ds + \int_1^2 \frac{dp}{\rho} + \frac{1}{2}(c_2^2 - c_1^2) + g(z_2 - z_1) = 0 \quad (5.5)$$

with ds - the arch length along the streamline.

Eq. (5.5) is Bernoulli's equation for unsteady frictionless flow along a streamline. Now, assuming that we are in the presence of incompressible steady irrotational flow, Eq. (5.5) can be reduced to:

$$\frac{p}{\rho} + \frac{1}{2}c^2 + gz = \text{constant} \quad (5.6)$$

which is the reduced momentum equation, the same constant holding throughout the entirety of the flow field. From vector analysis, a vector whose rotational is zero ($\xi = 0$) must be the gradient of a scalar function [Aris 1989]:

$$\nabla \times \mathbf{c} \equiv 0 \mapsto \mathbf{c} = \nabla \phi \quad (5.7)$$

with, ϕ - velocity potential function, where $\phi = \phi(x, y, z, t)$, a solution of the Navier–Stokes equations for inviscid, incompressible and irrotational fluids [Joseph 2003]. The knowledge of ϕ , introduced by Lagrange in 1788 [Anderson Jr. 1999a], immediately yields the cartesian velocity components:

$$c_x = \frac{\partial \phi}{\partial x} \quad , \quad c_y = \frac{\partial \phi}{\partial y} \quad , \quad c_z = \frac{\partial \phi}{\partial z}$$

It is important to mention that lines with constant ϕ are known as potential lines.

Under this framework we can get Bernoulli's unsteady irrotational equation (Eq. (5.5)), crucial for the analysis of accelerating flow fields:

$$\frac{\partial \phi}{\partial t} + \int \frac{dp}{\rho} + \frac{1}{2}|\nabla \phi|^2 + gz = \text{constant} \quad (5.8)$$

which for a steady irrotational flow yields:

$$\frac{\partial \phi}{\partial t} + \frac{p}{\rho} + \frac{1}{2}c^2 + gz = \text{constant} \quad (5.9)$$

with, $c = |\nabla \phi|$. Also relevant is the combination of the incompressible continuity equation, $\nabla \cdot \mathbf{c}$, with Eq. (5.7):

$$\nabla \cdot \mathbf{c} = \nabla \cdot (\nabla \phi) = 0 \quad (5.10)$$

or, also denoted as:

$$\nabla^2 \phi = \frac{\partial^2 \phi}{\partial x^2} + \frac{\partial^2 \phi}{\partial y^2} + \frac{\partial^2 \phi}{\partial z^2} \quad (5.11)$$

Thus, the continuity equation leads to Eq. (5.11), the widely know Laplace's equation. This equation is valid if the stream Mach number is less than 0.3 (Mach number, $Ma = c_{local}/c_{sound}$, with c_{local} , local flow velocity and c_{sound} , speed of sound), which essentially represents low-speed flows.

One notable property of the velocity potential is that if the flow is both irrotational and described by only two space coordinates, then the potential lines will be perpendicular everywhere in the flow to the streamlines (curves tangent to the velocity vector, indicating the direction of travel of a massless flow particle). This is known as the orthogonality between potential lines and streamlines (*vd.* Fig. 5.1).

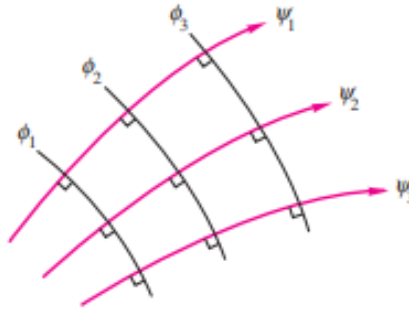


Figure 5.1: Orthogonality between potential lines and streamlines in an inviscid flow. Extracted from "Fluid Mechanics," by F.M. White, 2011 [White 2011].

In a flow solely described by two space coordinates the stream function, ψ , is an alternative approach for the description of an incompressible flow in Oxy :

$$c_x = \frac{\partial \psi}{\partial y} \quad , \quad c_y = -\frac{\partial \psi}{\partial x}$$

Additionally, the irrotationality leads to Laplace's equation for the stream function:

$$\frac{\partial^2 \psi}{\partial x^2} + \frac{\partial^2 \psi}{\partial y^2} = 0 \quad (5.12)$$

The boundary conditions for the stream function are the known velocity of the free stream ($\frac{\partial\psi}{\partial x}$ and $\frac{\partial\psi}{\partial y}$) and no flow through a solid surface ($\psi_{body} = \text{const}$). When both, ϕ and ψ exist, simultaneously, the potential and stream functions are known as conjugate harmonic functions [Chattot and Hafez 2015].

5.1.1 Elementary Plane Flow Solutions

Many solutions for the velocity potential make use of the superposition principle and rely on elementary solutions. As such, three are introduced: a uniform flow in the x -direction, a line source or sink and a doublet.

Uniform flow

A uniform flow consists of a constant velocity field, $\vec{c} = c_x\hat{i} + c_y\hat{j}$. Hence, a uniform flow in the x -direction can be described as $\mathbf{c}_0 = (c_0, 0)$. This yields:

$$\begin{aligned} c_x = c_0 &= \frac{\partial\phi}{\partial x} = \frac{\partial\psi}{\partial y} \\ c_y = 0 &= \frac{\partial\phi}{\partial y} = -\frac{\partial\psi}{\partial x} \end{aligned} \quad (5.13)$$

Now, if we integrate the expressions from Eq. (5.13) discarding the integration constants, as they do not affect the flow velocities, we obtain the well-known expressions for the stream and potential functions:

$$\phi = c_0x \quad , \quad \psi = c_0y \quad (5.14)$$

It is evident from the expressions of Eq. (5.14) that the orthogonality between streamlines and potential lines is ensured (vd. Fig. 5.2). Additionally it is easily shown that the uniform flow is both irrotational ($\xi \equiv \nabla \times \vec{c} = 0$) and to have zero divergence ($\nabla \cdot \vec{c} = 0$), satisfying Laplace's equation for the potential function, $\nabla^2\phi = 0$ and for the stream function $\nabla^2\psi = 0$, respectively.

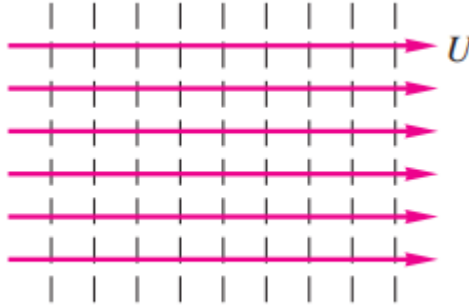


Figure 5.2: Uniform stream. Solid lines are streamlines and dashed lines are potential lines. Extracted from "Fluid Mechanics," by F.M. White, 2011 [White 2011].

Line Source or Sink

To correctly understand the concept of a line source one must think of the z -axis as a line of length b from which there is an outward (source) or inward flow (sink), which has a flowing rate, \dot{q} ($\dot{q} > 0$, source; $\dot{q} < 0$, sink). If we perform a cut-section of the z -axis we obtain Fig 5.3. Fig. 5.4 is a computer-generated drawing of a source using the contour feature of MATLAB.

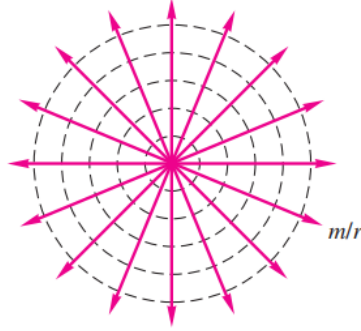


Figure 5.3: Line Source schematic. Solid lines (radial spokes) are streamlines and dashed lines (circles) are potential lines. Extracted from "Fluid Mechanics," by F.M. White, 2011 [White 2011].

It is, then, appropriate to work with plane polar coordinates (r, θ) , the distance and the polar angle of a point to the source/sink, respectively. Thus, and for simplicity with $b = 1$, the velocity expressed in polar coordinates is:

$$c_r = \frac{\dot{q}}{2\pi} \frac{1}{r} = \frac{\dot{m}}{r}, \quad c_\theta = 0 \quad (5.15)$$

with, $\dot{m} = \dot{q}/2\pi$ a constant, positive for a source, negative for a sink.

c_r , radial velocity.

c_θ , circumferential velocity.

Additionally the potential and stream functions are given by the following equation:

$$\phi = \dot{m} \ln r, \quad \psi = \dot{m} \theta \quad (5.16)$$

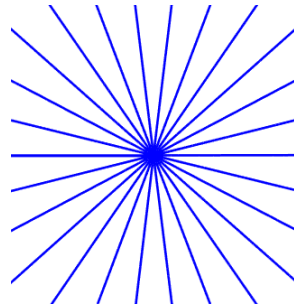


Figure 5.4: Computer-drawn source stream function with 25 contour lines using MATLAB.

Doublet

A doublet (*vd.* Fig 5.5) is a source-sink pair of $\pm\dot{q}$ strength located symmetrically at $(\pm l, 0)$. If we allow l to approach zero, while at the same time maintaining the product $\dot{Q} \equiv l\dot{q}$ constant (which implies the increase of the strengths of the source and sink) then we obtain a doublet of $\dot{Q} = \lim_{l \rightarrow 0, \dot{q} \rightarrow \infty} l\dot{q}$ strength.

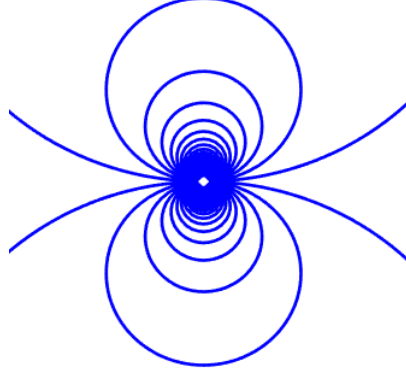


Figure 5.5: Computer-drawn doublet stream function with 100 contour lines using MATLAB.

Thus, the velocity components will be:

$$c_r = \frac{-\dot{Q} \cos \theta}{r^2} \quad , \quad c_\theta = \frac{-\dot{Q} \sin \theta}{r^2} \quad (5.17)$$

and the results for the potential and stream functions:

$$\phi = \dot{Q} \frac{\cos \theta}{r} \quad , \quad \psi = -\dot{Q} \frac{\sin \theta}{r} \quad (5.18)$$

The stream and potential functions can also be represented in Oxy coordinates:

$$\phi = -\frac{\dot{Q}y}{x^2 + y^2} \quad , \quad \psi = -\frac{\dot{Q}x}{x^2 + y^2} \quad (5.19)$$

5.2 Circular Cylinder

As previously stated, a crucial part when calculating the loads in wind turbines is the modelling of the flow through the tower. Some assumptions and simplifications are necessary, namely: incompressible, frictionless and irrotational flow and that the tower can be correctly approximated by a circular cylinder (*vd.* Fig. 5.6).

We are, thus, in the presence of a paradigmatic problem of elementary fluid dynamics [Crowdy 2006]: the potential flow past a circular cylinder, which is reduced to a circle in a 2-D plane. In order to satisfy the circle's boundary condition we superimpose a uniform flow with a doublet [Parkinson and Jandali 1970], which produces the ensuing flow field:

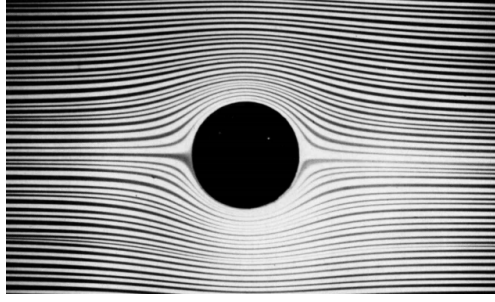


Figure 5.6: Hele-Shaw flow [Hele-Shaw 1898] past a circle. Extracted from "An Album of Fluid Motion," by M. Van Dyke, 1982, Parabolic Press Stanford [Van Dyke 1982].

$$c_r = c_0 \cos \theta - \dot{Q} \frac{\cos \theta}{r^2} \quad (5.20)$$

$$c_\theta = -c_0 \sin \theta - \dot{Q} \frac{\sin \theta}{r^2} \quad (5.21)$$

in return, the potential and stream functions are:

$$\phi = \left(c_0 r + \frac{\dot{Q}}{r} \right) \cos \theta \quad (5.22)$$

$$\psi = \left(c_0 r - \frac{\dot{Q}}{r} \right) \sin \theta \quad (5.23)$$

From Eq. (5.23) we can verify that $\psi = 0$ for $r = e$, which is the flow past a circular cylinder of radius e (*vd.* Fig. 5.7, this is attained if we equal $c_0 r$ with \dot{Q}/r , which yields $r = \sqrt{\dot{Q}/c_0} = e$).

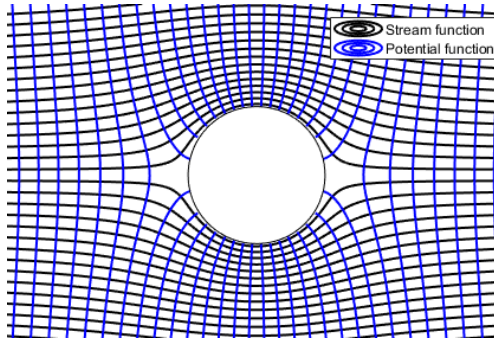


Figure 5.7: Computer-drawn flow through a circular cylinder, where streamlines are black and potential lines blue. Plotted using MATLAB.

Likewise, Eq. (5.22) and (5.23) inform us regarding the doublet's strength, which is $\dot{Q} = c_0 e^2$, which satisfies the tangency condition at the surface of the cylinder, ensuring that $c_r = 0$.

Eq. (5.22) and (5.23) can be viewed as a particular case of a closed-body (the net source outflow equals the net sink inflow), the *Rankine oval* [Rankine 1854]. This cylindrical-shaped body consists on the superimposition of a source-sink pair, parallelly aligned to a uniform flow, as exemplified by Fig. 5.8 (*n.b.*: in this figure $a = l$). Its governing stream function is:

$$\psi = c_0 r \sin \theta + \dot{m}(\theta_1 - \theta_2) \quad (5.24)$$

with, $\dot{m} = \dot{Q}/2\pi$.

The stream function is plotted in Fig. 5.9. It must be noted that the oval is the line $\psi = 0$ and that streamlines within the oval are uninteresting. The geometry of the oval (its length and height), depend on on the relative strength of the source and stream, the ratio $\dot{m}/(c_0 l)$.

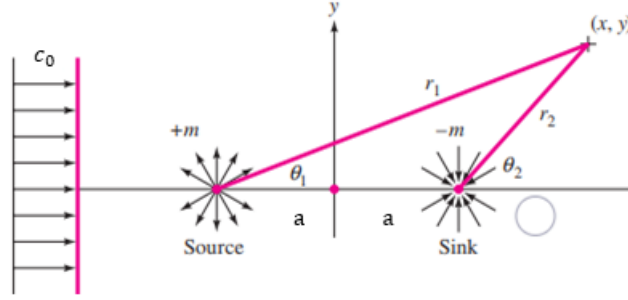


Figure 5.8: Schematic of source-sink pair in uniform flow. Adapted from "Fluid Mechanics," by F.M. White, 2011 [White 2011].

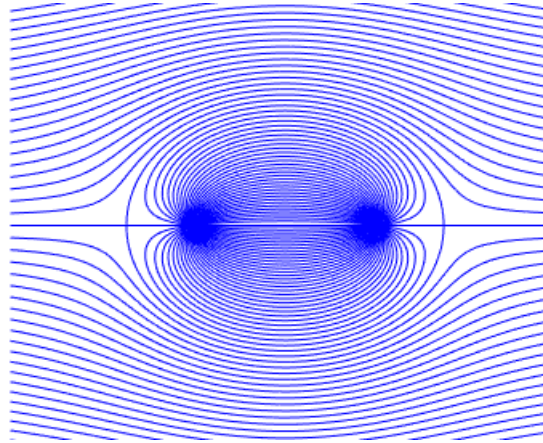


Figure 5.9: Computer-drawn circle of radius a stream function with 500 contour lines using MATLAB.

When $\dot{m}/(c_0 l) \rightarrow \infty$, then the oval becomes a circle and the relative maximal velocity, $c_{max}/c_0 \rightarrow 2$. In this case, Eq. (5.20) and (5.21) for the surface of the cylinder ($r = a$)

become:

$$c_r = 0 \quad , \quad c_\theta = -2c_0 \sin \theta \quad (5.25)$$

This yields that the maximum speed shall occur for $\theta = \pm 90^\circ$ with a value of $2c_0$ and that the minimum speed, which is characterized by the stagnation line, is 0. The stagnation points can be found for $c_\theta(e, \theta_s) = 0$, which immediately presents two possible solutions, $\theta_s = 0^\circ$ or $\theta_s = 180^\circ$.

Additionally, Eq. (5.20), (5.21), (5.22) and (5.23) can be further generalized, as the flow past a circular cylinder of radius e can also be given by the superposition of the uniform flow, a doublet of strength $\dot{Q} = c_0 e^2$ and a potential vortex (purely circulating steady motion, of strength K or $K/(Ue)$; only one function c_θ is irrotational, which is commonly known as free-vortex).

For a free vortex (*vd.* Fig. 5.10):

$$c_r = 0 \quad , \quad c_\theta = \frac{K}{r} \quad (5.26)$$

$$\psi = -K \ln r \quad , \quad \phi = K\theta \quad (5.27)$$

There is a clear symmetry between Eq. 5.27 and Eq. (5.16), being the vortex a sort of reversed source.

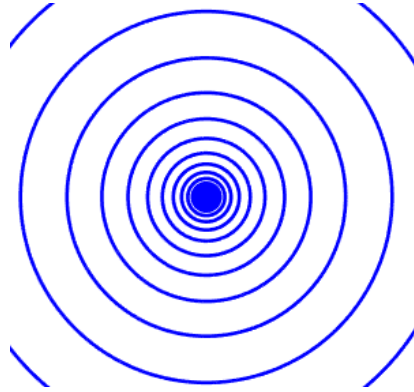


Figure 5.10: Computer-drawn vortex stream function with 20 contour lines using MATLAB.

The vortex, albeit being irrotational almost everywhere, it is not so in its origin, where the vorticity $\nabla \times \mathbf{c}$ is infinite, which results in the existence of a line integral known as fluid circulation, Γ (existent around a vortex center and previously mentioned in Section 2.2). For the closed curve C and arc length ds we have:

$$\Gamma = \int_C \mathbf{c} \cdot d\mathbf{s} = \oint_C c \cos \alpha ds \quad (5.28)$$

Usually, in an irrotational flow, $\Gamma = 0$. However, for a vortex $\phi = K\theta$, $\Gamma = 2\pi K$. Finally,

this yields the generalised equations:

$$\begin{aligned} c_r &= c_0 \cos \theta - \dot{Q} \frac{\cos \theta}{r^2} \\ c_\theta &= -c_0 \sin \theta - \dot{Q} \frac{\sin \theta}{r^2} - \frac{\Gamma}{2\pi} \frac{1}{r} \end{aligned} \quad (5.29)$$

$$\psi = c_0 \sin \theta \left(r - \frac{e^2}{r} \right) - K \ln \frac{r}{e} \quad (5.30)$$

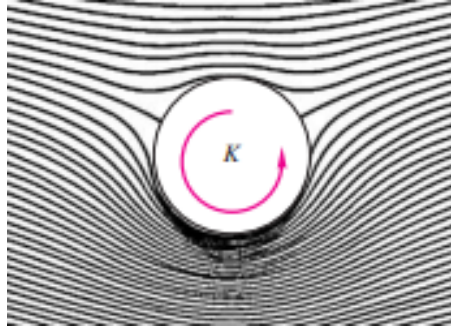


Figure 5.11: Effect of circulation in the flow past a circular cylinder. $K/(c_0 e) = 1$. An inviscid downward lift, the *Magnus force* [Magnus 1853], given by the Kutta-Joukowski Theorem, is developed normal to the free stream. Extracted from "Fluid Mechanics," by F.M. White, 2011 [White 2011].

Naturally, in the case of the wind turbine tower, the circulation Γ is 0 (there is no free vortex), which reduces the set of equations, Eq (5.29) to (5.20) and (5.20) and and (5.30) to (5.22) and (5.23). Furthermore, as previously mentioned, if $r = e = \sqrt{Q/c}$, then Eq. (5.20), (5.21), (5.22) and (5.23) are reduced to:

$$\psi = c_0 r \left(1 - \frac{e^2}{r^2} \right) \sin \theta \quad (5.31)$$

$$\phi = c_0 r \left(1 + \frac{e^2}{r^2} \right) \cos \theta \quad (5.32)$$

$$c_r = c_0 \left(1 - \frac{e^2}{r^2} \right) \cos \theta \quad (5.33)$$

$$c_\theta = -c_0 \left(1 + \frac{e^2}{r^2} \right) \sin \theta \quad (5.34)$$

Finally, the pressure field can be attained through Bernoulli's equation (note the non-inclusion of the gravitic term, which doesn't contribute):

$$p_\infty + \frac{1}{2} \rho c_0^2 = p_s + \frac{1}{2} \rho c_{\theta,s}^2 \quad (5.35)$$

with, p_∞ - free stream pressure.

p_s - cylinder surface pressure.

$c_{\theta,s} - c_\theta$ at cylinder surface .

If we substitute $c_{\theta,s} = -2c \sin \theta$ (from Eq. (5.25)), the velocity at the surface of the cylinder:

$$p_s = p_\infty + \frac{1}{2}\rho c_0^2(1 - 4\sin^2 \theta) \quad (5.36)$$

This can also be expressed through a pressure coefficient, C_p [Brederode 2014]:

$$C_p = \frac{p - p_\infty}{\frac{1}{2}\rho c_0^2} \quad (5.37)$$

Applying Bernoulli's equation to Eq. (5.37) yields:

$$p - p_\infty = \frac{1}{2}\rho(c_0^2 - c^2) \quad (5.38)$$

Thus, and for $c = c_s$, c_s the cylinder surface velocity:

$$C_p = 1 - \left(\frac{c_s}{c_0}\right)^2 \quad (5.39)$$

which leads to:

$$C_p = 1 - 4\sin^2 \theta \quad (5.40)$$

This equation could let us believe that the cylinder would have zero drag, F_d , more commonly know as d'Alembert's paradox [d'Alembert 1752]. Although this is clearly antithetical to real fluid flows, the inviscid theory is still valid, mostly because of Prandtl's boundary-layer theory [Schlichting and Gersten 2016].

Additionally, experimental results show that this model has some agreement for regions between 0° and 90° , but it is lost for other regions due to the effect of viscous forces that give rise to separation. As we are discussing upstream tower effect, this is not relevant.

Finally, the pressure coefficient can be calculated for the entirety of the field if we substitute $c_{\theta,s}$ in Eq. (5.35) with c_θ from Eq. (5.34) . Eq. (5.38) will have a different $p - p_\infty$, which will ultimately yield:

$$C_p = 1 + \frac{\sin \theta \left(1 + \frac{e^2}{r^2}\right)}{c_0} \quad (5.41)$$

Eq. (5.41) can be plotted, as exhibited by Fig. 5.12 (*N.b.* the circle was filled in gray, seeing that the pressure coefficient has no physical meaning in that region).

As previously mentioned, the potential flow theory is of the utmost importance for the tower interference model, as all information regarding the incoming velocity vector is dependent on this formulation. The potential flow theory allows us, for a given distance from the tower, to know the velocity vector magnitude and direction (through its decomposition), which is essential to determine the angle of attack the blade will face, and also serve as input/boundary conditions for the XFOIL calculations.

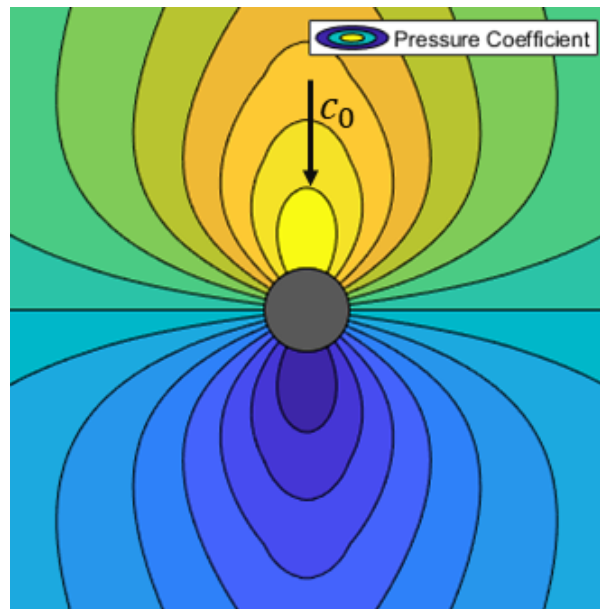


Figure 5.12: Computer-drawn C_p with 15 contour lines using MATLAB's `contourf` function.

Chapter 6

XFOIL

6.1 Introduction to XFOIL

In order to assess the flow conditions for a given airfoil, along with the lift, drag and pressure coefficients, the free software XFOIL [Drela 1989] was selected, in the form of the 6.99. version.

Designed by Mark Drela integrated within MIT's Daedalus human-powered project [Langford 1989], it is notorious for its low computational cost, and thus, faster solutions and robustness, important characteristics when one considers the amount of calculations the tower interference model will require.

Based on high order panelling methods with a Kármán-Tsien compressibility correction [von Kármán 1941, Tsien 1939], and presenting a fully coupled viscous/inviscid interaction method [Mauclère 2009] computed through a global Newton method, hailing from Drela's ISES code [Drela and Giles 1987], it is particularly suited for subsonic airfoils, as the ones found in wind turbines.

The XFOIL panel method superimposes source distributions on the airfoil and wake as to permit the modeling of the viscous layer (represented by a two-equation lagged dissipation integral method) influence on the incompressible potential flow. It additionally determines the drag from the wake momentum thickness far downstream.

The transition point determination criteria is based on the e^n -Method (Envelope-Method [Heinzelmann 2011]), which assumes the superimposition of a sinusoidal, time-dependent disturbance [Baines *et al.* 1996], known as Tollmien-Schlichting waves [Tollmien 1929, Schlichting 1933] (*vd.* Fig. 6.1), to the undisturbed, parallel flow, from which, and due to a no-slip condition boundary condition (a form of Dirichlet's boundary condition [Dirichlet 1889]), a Blasius boundary layer arises [Blasius 1908]. The e^n method is only adequately applicable if the Tollmien-Schlichting waves are the dominant transition-initiating mechanism [Drela 1989].

The parameter n , which in XFOIL is designated as N_{crit} , is the "logarithm of the amplification factor of the most-amplified frequency which triggers transition" [Drela 1989], and whose value depends on the operating-ambient disturbance level. If the amplitude of the biggest discontinuous frequency exceeds e^n , then it is assumed that transition has occurred, and the flow is fully turbulent [Aichinger 2012]. Table 6.1 reflects the typical values for n .

The standard value for N_{crit} is $n = 9$, which, unless further indication, was also the value used in this work's computations. This factor (and transition in general) mightn't

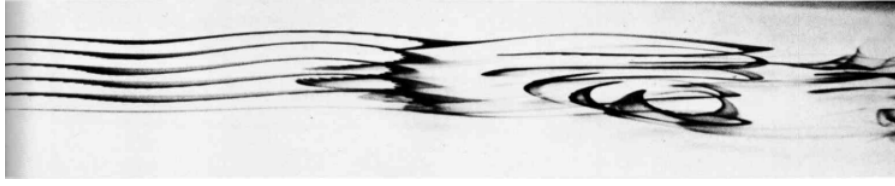


Figure 6.1: Transition downstream of Tollmien-Schlichting Waves, passing from two-dimensional to three-dimensional and finally, turbulent on the far right side. Extracted from "An Album of Fluid Motion," by M. Van Dyke, 1982, Parabolic Press Stanford [Van Dyke 1982].

Table 6.1: Typical values of n . Adapted from Drela [Drela 1989].

Situation	n
Sailplane	12-14
Motor glider	11-13
Clean wind tunnel	10-12
Average wind tunnel	9
Dirty wind tunnel	4-8

seem of the utmost importance when considering the high Reynolds numbers typically found on modern wind turbines, but for consistency, it was selected as it represents the typical value of a smooth wing surface in a low turbulence environment [Selig 2003].

For a given Reynolds number (Re), Mach number (Ma) and angle of attack (α), XFOIL provides the pressure coefficient distribution, C_p , lift coefficient, C_l , drag coefficient, C_d , moment coefficient, C_m and lift-to-drag ratio F_l/F_d , in a pop-up window, as exemplified by Fig. 6.2. It also returns in the command screen the last iteration, which includes the point of transition (X_{tr}) in the suction and pressure surfaces, in addition to the friction drag coefficient, C_{df} , and the pressure drag coefficient, C_{dp} .

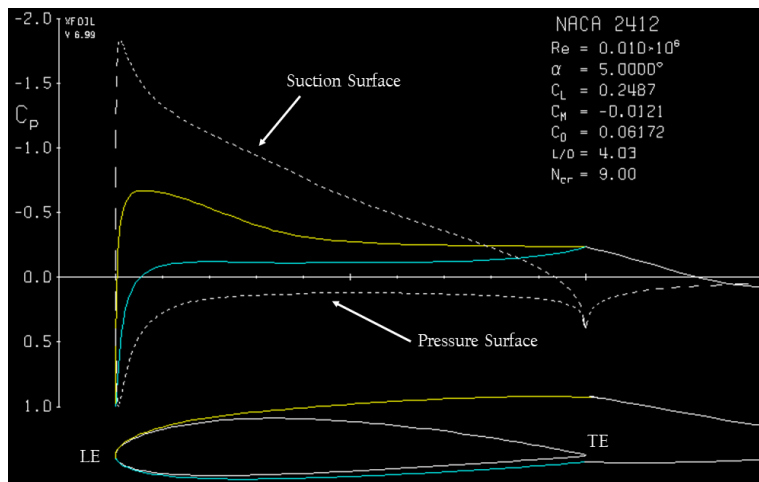


Figure 6.2: Results returned from XFOIL for NACA 2412 profile. Dashed lines represent inviscid calculations, coloured lines viscous calculations.

XFOIL also is able to perform calculations for several α (α varies between two values with a certain increment) and save α , C_l , C_d , C_m , C_{dp} and X_{tr} (for both upper and lower surfaces) into an output **.txt* file, so long as the auto point accumulation is toggled (**PACC** command) in order to activate the polar calculation.

Finally, the convergence of the solution might not be achieved, which implies that no output file is written. This is usually due to boundary layer separation and stall regions [Schlichting and Gersten 2016]. Thus, the range of α for which convergence is look for, as well as the Reynolds number, should be empirically tested, to better understand the limits of the flow solver. Additionally, specific points can also impede convergence, which requires preliminary computation to force convergence [Mauclère 2009]. It is thus advisable to sequence runs with small increments.

6.2 MATLAB Interfaces

It was decided that a better visualization of the results would be capacitated by the implementation of several MATLAB interfaces. Moreover, the use of MATLAB could further automate the processes, sparing time and labour.

MATLAB [Moler 2004] (portmanteau of matrix laboratory) is a numerical computing environment widely popular among scientists and engineers, particularly in the areas of algebraic calculations, numerical analysis and imaging and signal processing, integrating computation, visualization, and programming as well as presenting a modern programming language environment with data structures and object-oriented programming, to name a few [Houcque 2005]. As such, and due to its numerous toolboxes and the easy visualization-enabling graphics, MATLAB seems to be the perfect suit for many scientific applications, the present one included.

6.2.1 Airfoil Selection and Benchmarks

An initial MATLAB script was developed as to allow a proper visualization of the airfoil profiles, uploaded into XFOIL's work environment as **.dat* files. Airfoils are usually defined by a table containing two columns, both dimensionless numbers: the first relates the x -axis value to the chord length, L , and the second the y -axis value related to L . The table's x/L values must start on one of the extremities (be it at the leading edge, $x/L = 0$, or at the trailing edge, $x/L = 1$, as in Table 6.2), achieve the other edge and return to the initial point.

Table 6.2: Abridge NACA 2415 airfoil coordinate table.

x/L	y/L
1.00000	0.00157
...	...
0.00000	0.00000
...	...
1.00000	-0.00157

Airfoils also belong to numerous families, such as Delft University's DU-series [Bertagnolio *et al.* 2001], the National Advisory Committee for Aeronautics' NACA-series

[Abbott *et al.* 1945], the National Renewable Energy Lab's (NREL) S-series, based on the designs of Somers [Somers 1997] and Eppler's E-series [Eppler 1990], among many others. Three different airfoil profiles plotted using MATLAB are presented in Fig. 6.3.

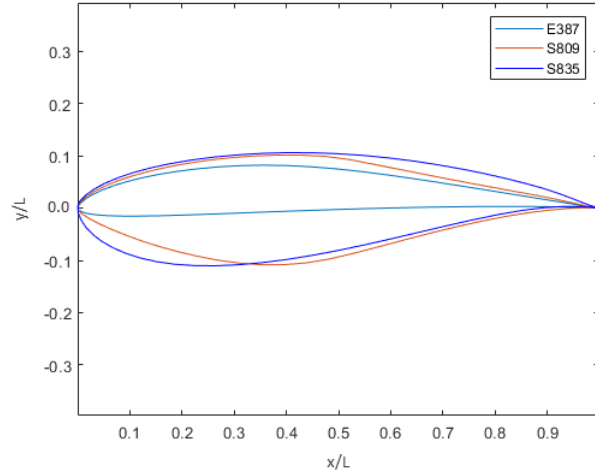


Figure 6.3: Three airfoil profiles plotted using MATLAB.

The MATLAB airfoil profile interface script can additionally present the maximum thickness (and corresponding x/L), as exemplified by Fig. 6.4. Note that this maximum thickness value is commonly referred in the literature as a percentage. As such, one can say that Fig. 6.4 exhibits the 9% thick Eppler 387 airfoil.

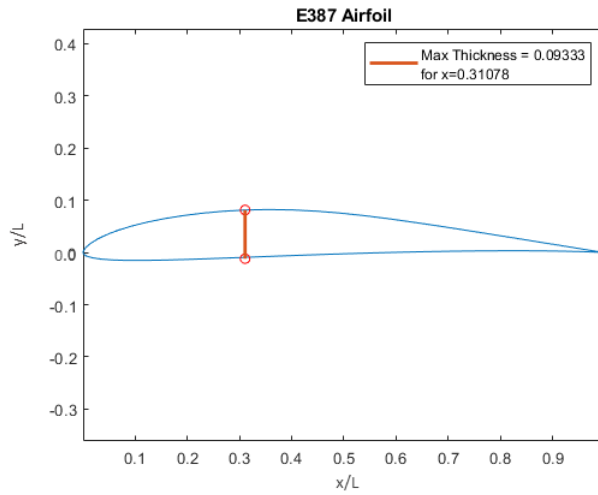


Figure 6.4: Eppler 387 airfoil profile plotted using MATLAB.

Another MATLAB interface implemented allowed the visualization of the outcomes emerged from the XFOIL procedure such as, angle of attack, lift coefficient, drag coefficient, and so on. This script loads the outcome save file from XFOIL's polar procedure, stemming from the automatic polar accumulation (**PACC**), and subsequently saves each of the output variables (α, C_l, C_d, \dots) into a corresponding array, which can be used into further calculations, or post-processing, including plotting.

Eppler 387

It was decided that an initial benchmark of the visualization-interface would be performed for Eppler's E387 airfoil, designed in the 1960s for model sailplanes. It has been widely regarded as an important benchmark for research in low Reynolds number airfoil aerodynamics [Coder and Maughmer 2014] and experimental results for this profile are plentiful (the 1980s NASA Langley Research Center LTPT's data are still the standard against which most of the experimental data is compared to [McGhee *et al.* 1988]).

The following procedure was executed:

1. Load E387's *.dat file extracted from **Airfoil Tools** [Airfoil Tools 2019] onto XFOIL's workspace;
2. Enter plain airfoil's name as E387;
3. Re-panel the airfoil with **PPAR**. 160 where selected (**N**-command). **PANE** can also be used;
4. Activate operating conditions menu (**OPER**) and toggle viscous mode (**visc** or **v**);
5. Enter Reynolds number, $Re = 2 \times 10^5$;
6. Activate polar with **PACC** and enter save and dump file's names;
7. Compute flow for $-5^\circ \leq \alpha \leq 15^\circ$ with a step of 0.1 using **ASEQ**;
8. Polar save file is loaded into MATLAB workspace as well as experimental results;
9. C_l vs α , C_d vs α , C_l/C_d vs α and C_l vs C_d graphs are plotted.

It must be added that, despite Langley's longevity, the experimental results chosen to juxtapose against XFOIL's results where Selig's Pennsylvania State University (Penn State) experimental results [Selig *et al.* 1995].

Fig. 6.5 presents the the computed lift and drag coefficients plotted as a function of the angle of attack, along with Penn State's experimental results. Additionally, Fig. 6.6 explains the physical meaning behind the plummet of the lift curve: for high α flow separation occurs (which means that for a portion of the airfoil the wind speed decreases, and conversely, the pressure increases), which causes a decrease on lift, a phenomenon called stall.

Fig. 6.7 represents the lift/drag coefficient ratio conjointly with the maximum value for said ratio and which is the corresponding angle of attack at which this value is attained.

The final graph plotted is the drag polar relationship (C_l vs C_d) represented in Fig. 6.8 in the polar graph, also know as the Lilienthal polar diagram [Anderson Jr. 1999b] (from the German term "*Lilienthal'sche Polardiagramm*").

What one can observe from all of the aforementioned figures is a decent concordance between the experimental results and XFOIL's results, particularly evident in Fig. 6.5. What is evidenced in Fig. 6.7 and 6.8 is, naturally, that a small misalignment between both curves in Fig. 6.5 will suffer an increase as C_l and C_d are divided and compared, respectively. It must be noted that XFOIL can only provide results pre-separation, which implies that a higher trustworthiness is to be expected for smaller angles of attack.

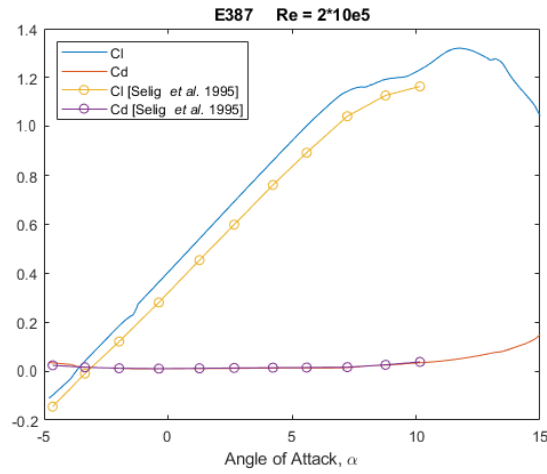


Figure 6.5: E387 lift and drag curves plotted using MATLAB.

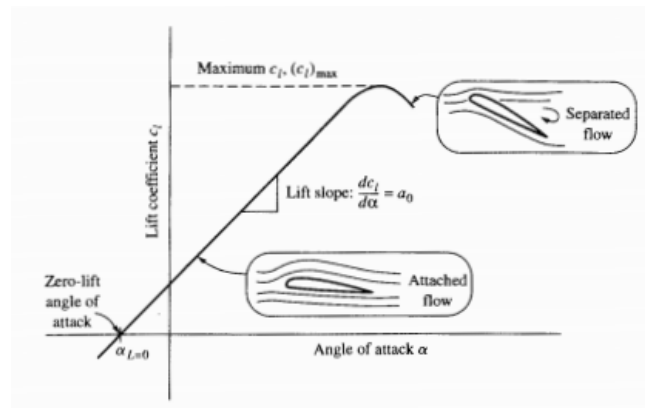


Figure 6.6: Generic lift curve explaining the occurrence of the maximum. Extracted from "Aircraft Performance and Design," by J. D. Anderson, 1999 [Anderson Jr. 1999b].

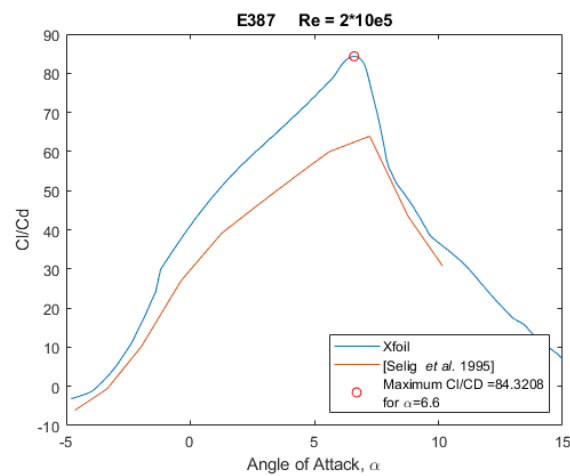


Figure 6.7: E387 C_l/C_d plotted using MATLAB.

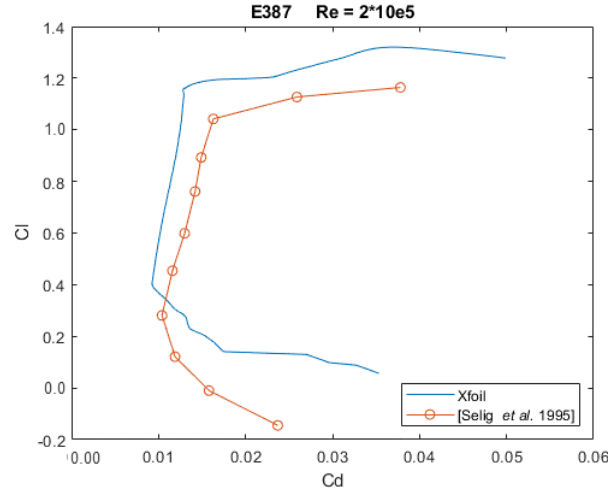


Figure 6.8: E387 Lilienthal polar diagram plotted using MATLAB.

6.2.2 S809 Profile

The airfoil profile selected to study the tower interference was the S809 (*vd.* Fig. 6.9), a 21 % thick (right in the transition between mid-span and tip [Van Rooij and Timmer 2004]) airfoil designed by Somers at NREL with the objectives of restrained maximum lift, insensitive to roughness, and low profile drag [Somers 1997]. The S809 airfoil is commonly approached by the specialized literature [Gomes *et al.* 2018], as its design was especially intended for HAWT applications.

This particular airfoil was selected as there are, not only trustworthy CFD analysis of tower interference using S809 which can serve as blueprints [Gómez and Seume 2009b, Gómez and Seume 2009a], but also experimental data from NREL's Phase VI, a widely accepted benchmark [Hand *et al.* 2001].

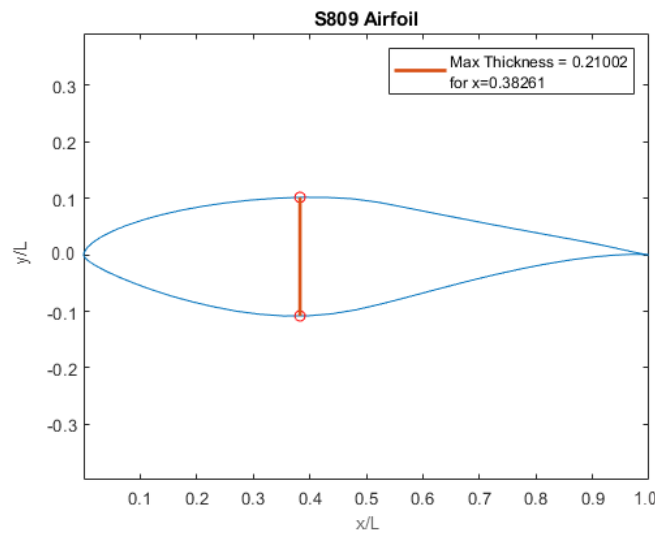


Figure 6.9: S 809 airfoil profile plotted using MATLAB.

Fig. 6.10, 6.11 and 6.12 are fruit of the MATLAB visualization-interface and where generated from the polar save file proceeding from XFOIL, as enumerated in Section 6.2.1, with two notable differences, besides the name of the **.dat* file and airfoil name: $Re = 10^6$ and $-7^\circ \leq \alpha \leq 20^\circ$. These numerical results are compared to the data set provided by Somers [Somers 1997] and obtained at the Delft University of Technology (DUT) Low Speed Laboratory low-turbulence wind tunnel with a Reynolds number of 10^6 . NREL also makes available publicly the experimental results from Ohio State University [NREL 2012], but as Wolfe [Wolfe and Ochs 1997] points out, these are "essentially identical".

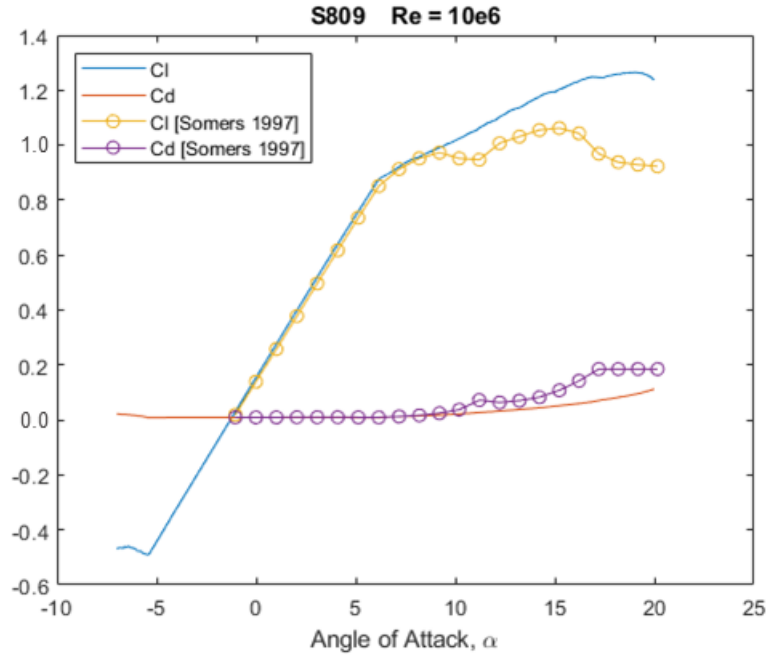


Figure 6.10: S809 lift and drag curves plotted using MATLAB.

As evidenced by the aforementioned figures, there is a good agreement, especially when one considers $0^\circ \leq \alpha \leq 8^\circ$, the smaller angles. As Fig. 6.10 shows, after this window ($0^\circ \leq \alpha \leq 8^\circ$, which is further evidenced by Fig 6.12, wherein both curves diverge after $C_l = 1.0$, the value at which the same happens in Fig. 6.10), the experimental results become less stable, and XFOIL's curve can not fully account for these changes. This clearly show us that, in spite of presenting a good agreement for smaller angles, XFOIL is still based on a, albeit robust, panel method, which doesn't always yields the most accurate results. Nevertheless, as it will be seen in Part III, the input angles of attack are within this desired window for α .

6.2.3 MATLAB-XFOIL Interface

As previously stated in the beginning of Section 6.2, MATLAB was used to automate the attainment of XFOIL's outcomes, and further calculate utilizing these values. As such, MATLAB preforms the necessary tower-induced velocity field computation, among others, and utilizes these results as input for XFOIL, opening it remotely, feeding it the

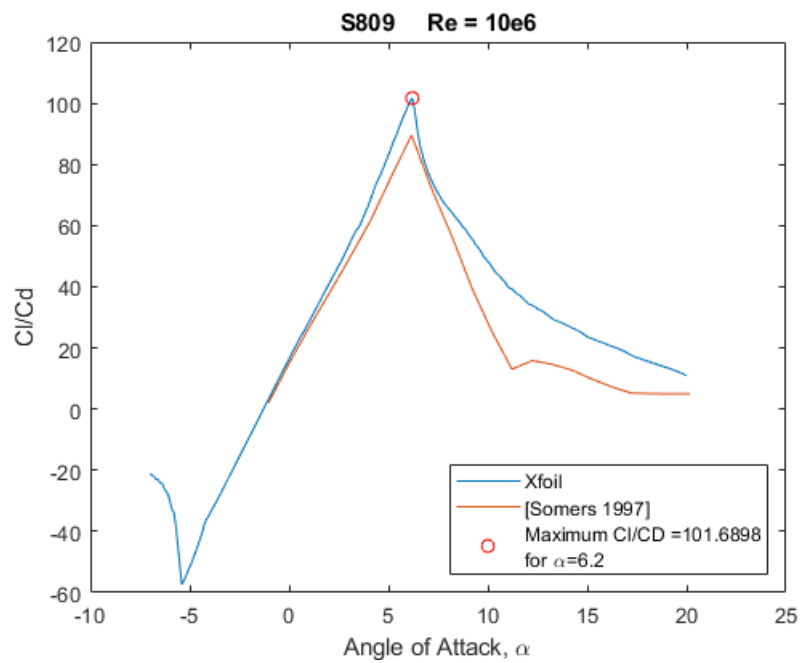
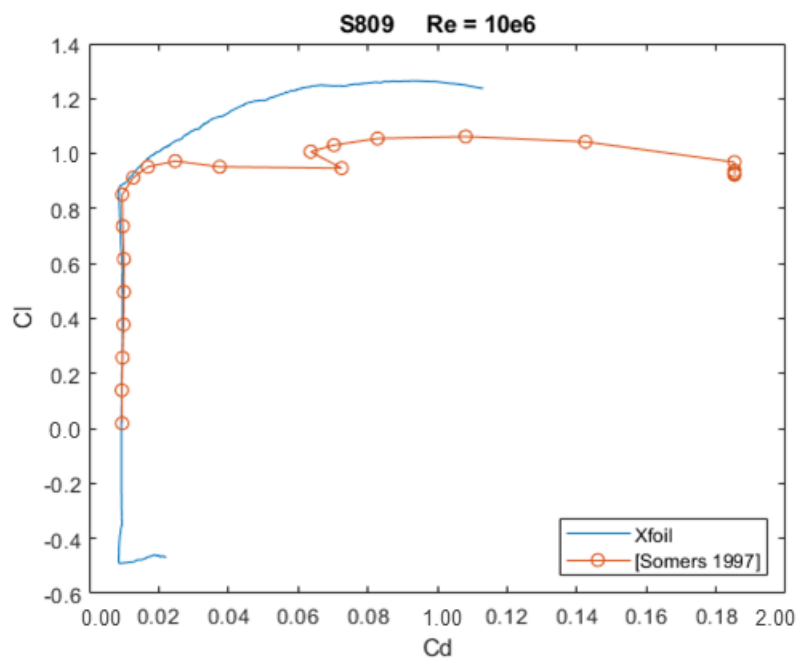
Figure 6.11: S809 C_l/C_d plotted using MATLAB.

Figure 6.12: S809 Lilienthal polar diagram plotted using MATLAB.

orders, closing and reading the outcomes, which are then utilized for further calculations.

The MATLAB code initially calculates, for fixed values of x , incoming velocity and λ , the polar coordinates which enable to compute the potential flow solutions around the tower for the radial and tangential velocity (which are further decomposed in the x - and y -axis components), and that amounts to the absolute value of the velocity through Pythagoras' Theorem.

It then performs the same calculations within a 'for' loop, whose iteration runs from the minimum up to the maximum value of y with a pre-determined, tower radius-dependent step. Within the 'for' loop other variables are computed, namely, ϕ , the angle described between w and u , the relative and circumferential velocity, respectively. The physical meaning of these variables will be further developed in Chapter 8 through their governing equations. It is, nonetheless, necessary to mention that w is directly applied into the calculation of Reynolds number:

$$Re = \frac{w \cdot L}{\nu} \quad (6.1)$$

with, L - airfoil chord length, and ν - kinematic air viscosity measured at 20°C ($15.06 \cdot 10^{-6} \text{ m}^2/\text{s}$)

After the calculations, MATLAB's commands **fopen** and **fprintf** are used, respectively, to create a writable **.txt* file, and to write in said file the orders that XFOIL shall read. The output text file is as follows:

Table 6.3: Sequence of XFOIL sequence orders.

Load *.dat	Loads airfoil coordinates form .dat file. * must be the name of a .dat file within MATLAB's folder containing just the coordinates of the airfoil and no header. In this case * = S809.
S809	Airfoil's name
Pane	Re-panels airfoil with 160 panels.
Oper	Opens operations menu.
Visc	Toggles viscosity-mode.
Re	Writes a Reynolds number (Re) as calculated in Eq. (6.1) (differs with each iteration)
Iter b	Selects b -number of iterations.
Pacc	Toggles polars.
Polars <i>i</i>	Names polar save file, with i = number of iteration.
Polard <i>i</i>	Names polar dump file, with i = number of iteration.
a h	Computes values for an angle of attack h , as given by 8.12 (differs with each iteration).
Pacc	Toggles polars off.
[-]	Blank line to exit operations menu.
Quit	Exits XFOIL.

This is proceeded by the MATLAB command **system('naca &')**, which calls a batch file, *naca.bat*, where it is written **XFOIL.exe < automat.txt** (the batch file, located in

the same folder as the MATLAB **.m* file, calls XFOIL and utilizes the recently created *automat.txt* as the input orders file.

Subsequently, the MATLAB program needs to upload the *i* polar save files generated by XFOIL into its workspace. This is accomplished by a 'for' loop with the same iteration parameters as the preceding one, in which MATLAB's `uigetfile` command is called, as well as a function, named `importXfoilfile`, whose sole input parameter is the file name, and has been written as to ignore the polar save file's headers and import just the data table (*vd.* Fig. 6.13).

```

XFOIL          Version 6.99

Calculated polar for: S809

1 1 Reynolds number fixed      Mach number fixed

xtrf =  1.000 (top)      1.000 (bottom)
Mach =  0.000      Re =  9.159 e 6      Ncrit =  9.000

alpha    CL      CD      CDp      CM      Top_Xtr  Bot_Xtr
-----
-7.331   -0.6609   0.01026  0.00515  -0.0311  0.5481  0.0021

```

Figure 6.13: Example of XFOIL polar save file.

Having uploaded the data from the polar save files the program, through the use of yet another 'for' loop with the same iteration parameters, extracts the different variables from each data table: α , C_l , C_d , C_m . It additionally calculates, for each iteration, the corresponding lift, drag, normal and tangential forces, but also the dimensionless normal and tangential force coefficients.

Finally, the program also plots the different variables into a myriad of graphs through the use of the interpolating MATLAB function `interp1` applying a spline method [Schoenberg 1946].

Intentionally blank page.

Chapter 7

QBlade

After the development of the MATLAB-XFOIL Interface, whose underlying Tower Interference Model and results will be discussed thoroughly in Part III, it was deemed desirable to obtain some additional information regarding the selected airfoil, S809, in a tower-influence-free calculation environment, namely the expected power output for the entire geometry of a wind turbine using said airfoil. For this, the open source software QBLADE was employed.

Created at the Technical University of Berlin’s Institute of Fluid Dynamics and Technical Acoustics, QBLADE was developed with the intent of generating a catch-all tool that would be able to perform all the necessary aerodynamic analysis of a wind turbine without the need to import, convert or process data from other sources, allowing airfoil design and analysis, lift and drag polar extrapolation, blade design and optimization and turbine definition and simulation [Marten *et al.* 2013].

QBLADE requires the integrated use of XFOIL for the design of custom airfoils and the computation of the lift and drag coefficient polars, which has been neatly done through a user-friendly graphical interface. It additionally utilizes the BEM method to simulate wind turbine performance, whose selection is justified by its cost-efficiency and reduced computational time requirement, whereas a CFD analysis of the entire geometry accounting for unsteadiness, three-dimensionality, and turbulence, amongst other phenomena, is simply too costly, as discussed in Section 2.4, narrowing its applicability to research environments [Marten and Wendler 2013]. Nevertheless, newer versions of the software have evolved to include a lifting-line free vortex wake algorithm, greatly improving convergence in VAWTs, but still lacking a structural model coupling [Marten 2016].

QBLADE’s user-friendliness and holistic approach mean that it is an extremely valuable tool for the analysis of wind turbines, and, perhaps most importantly, incredibly quick to utilize and implement, allowing, for this particular application, results cross-checking and validation for some assumptions, even though it can not take into account the tower’s influence. As such, we can define a routine that culminates in a full rotor BEM simulation:

1. Import airfoil coordinates saved **.dat* file;
2. Select airfoil direct analysis, where the analysis parameters are $Re = 10^6$, $-7^\circ \leq \alpha \leq 20^\circ$, $Ma = 0$ and $N_{crit} = 9$ (here we’ve employed the same parameters as in the original XFOIL analysis), instantly obtaining the Lilienthal, C_l vs α , C_d vs

X_{tr} , C_l/C_d vs α and C_m vs α graphs, as observable in Fig. 7.1:

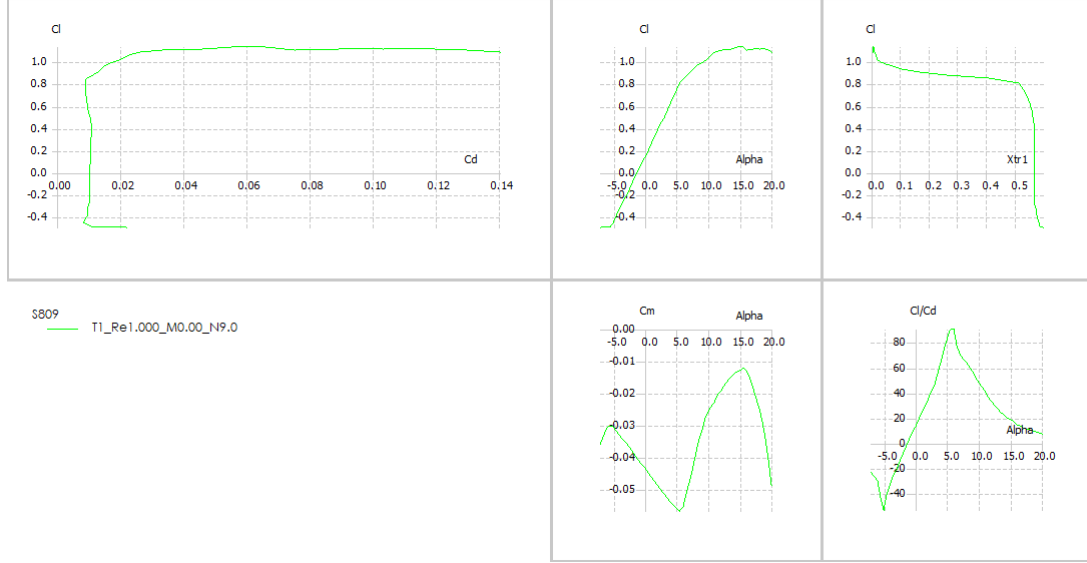


Figure 7.1: Lilienthal, C_l vs α , C_l vs X_{tr} , C_l/C_d vs α and C_m vs α graphs clock-wise, from left to right.

If we compare the graphs attained with figures 6.10, 6.11 and 6.12 we can quickly identify the overall agreement between both sets of figures, which further proves the high degree of conformity the visualization-interface possesses. One can additionally view the pressure vectors and boundary layer in the airfoil surface.

3. Select 360° with a Montgomerie extrapolation [Montgomerie 2004], generating a circular foil. This is necessary as QBLADE requires polar data for an entire revolution (360°);
4. Access HAWT rotor blade design, and start designing the blade through sections, one circular, the other with the desired airfoil (the latter ought to span 75-80 % of the blade, whilst the circular section is only applicable at the root side) and by altering the section diameter values. Optimize blade (twist angles of sections) for $\lambda = 7$ using Betz's method and introducing the value for α at which C_l/C_d is maximal (consulting the corresponding graph). The optimized blade (*vd.* Fig. 7.2) or rotor can be visualized.
5. Finally, a BEM simulation can be performed, which, in this case, has been done for the default values of Prandtl's tip- and root loss and Reynolds drag corrections. This yields a visualization-environment capable of displaying an assortment of graphs, where a double-click allows the selection of the x - and y -axis variables, enabling a rather large set of graphs, namely the normal- and tangential force coefficients as related to the blade radius (and for several λ), the torque and thrust coefficients as related to the tip speed ratio, λ , (defined in QBLADE as TSR) and the power coefficient, C_P , as related to λ (*vd.* Fig. 7.3).

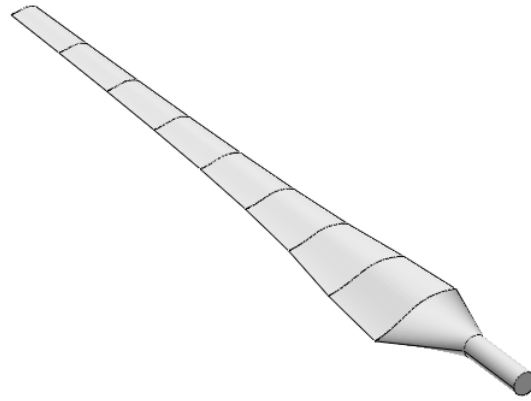


Figure 7.2: Optimized blade for S809 airfoil with 10 sections. Computed using QBLADE.

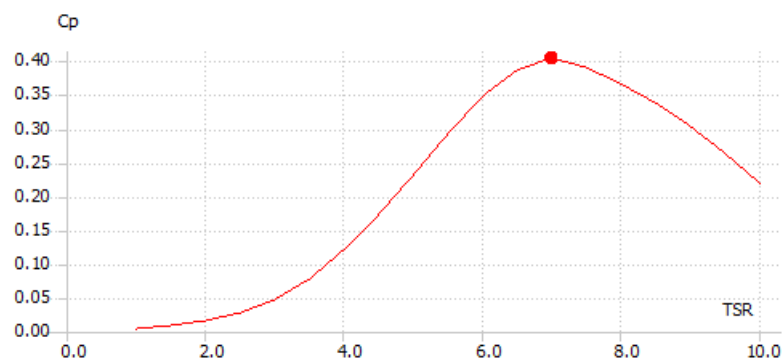


Figure 7.3: Power coefficient *vs* tip speed ratio ($\text{TSR} = \lambda$). *N.b.*, maximal value attained for $\lambda = 7$.

Intentionally blank page.

Part III

Model and Results

Chapter 8

Tower Interference Model

After having properly introduced all the necessary theoretical background assumptions, as well as the methods and tools to be employed, we can finally present the Tower Interference Model (TIM) developed in course of this thesis, which can be seen as the culmination of the practical application of all these previously presented terms, equations and software, combining the potential flow solutions around the circular cylinder with XFOIL's panel method to calculate the different aerodynamic loads, which will serve for further calculations.

As previously illustrated with greater detail in Chapter 5, this model will be based on the potential flow solutions for a circular cylinder. We proceed to recover some equations and figures previously presented in this chapter (appearing here unenumerated, as to avoid confusion), in order to facilitate the comprehension of the model, and preventing the reader from jumping between both chapters. As such, we begin with Eq. (5.22) and (5.23), which describe the potential and stream functions (obtained through the superposition of a uniform flow and a doublet, yielding the desired flow field):

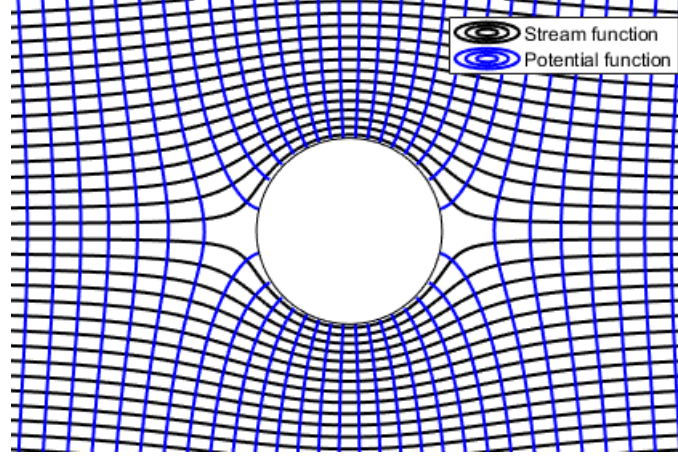
$$\phi = \left(c_0 r + \frac{\dot{Q}}{r} \right) \cos \theta \quad (5.22)$$

$$\psi = \left(c_0 r - \frac{\dot{Q}}{r} \right) \sin \theta \quad (5.23)$$

with, c_0 - Inflowing undisturbed velocity;
 r - radial coordinate;
 θ - angular coordinate;
 \dot{Q} - doublet strength ($\dot{Q} = ql$).

Here we recuperate Fig. 5.7, which plots the aforementioned functions (stream function in black, potential function in blue):

This figure represents both the stream and potential functions, encircling the tower, here as an idealized circular cylinder. The velocity in radial and circumferential components is described by Eq. (5.20) and (5.21):



$$c_r = c_0 \cos \theta - \dot{Q} \frac{\cos \theta}{r^2} \quad (5.20)$$

$$c_\theta = -c_0 \sin \theta - \dot{Q} \frac{\sin \theta}{r^2} \quad (5.21)$$

where $c = c_r \hat{r} + c_\theta \hat{\theta}$, the absolute wind velocity. As such, the absolute velocity magnitude can be calculated as given by Eq. (8.1):

$$c = \sqrt{c_r^2 + c_\theta^2} \quad (8.1)$$

Note that, the absolute velocity, c , can also be described as the vector sum of the relative velocity, w and circumferential velocity, u : $\vec{c} = \vec{w} + \vec{u}$, thus presenting the preferred nomenclature employed when dealing with turbomachinery. We can additionally observe the absolute velocity magnitude variation around the tower if we define a plane Ox at which we inspect its values throughout varying y , as observed in Fig. 8.1.

Perhaps most interestingly, Fig. 8.2 and 8.3 allow us to understand the impact the distance of the plane to the tower has on the velocity magnitude in near- and far-tower situations. The surge in velocity close to the center of the y -axis is due to concentration of streamlines, which causes the particles to move faster. Conversely, the velocity drops close to the center as we approach the stagnation streamline.

We can additionally revert the radial and circumferential components of Eq. (5.20) and (5.21) into the Cartesian system with the aid of a set of matrices that translate between polar and Cartesian coordinates:

$$\begin{pmatrix} \hat{i} \\ \hat{j} \end{pmatrix} = \begin{pmatrix} \cos \theta & -\sin \theta \\ \sin \theta & \cos \theta \end{pmatrix} \begin{pmatrix} \hat{r} \\ \hat{\theta} \end{pmatrix}$$

As such, the x and y velocity components shall be:

$$c_x = c_r \cos \theta - c_\theta \sin \theta \quad (8.2)$$

$$c_y = c_r \sin \theta + c_\theta \cos \theta \quad (8.3)$$

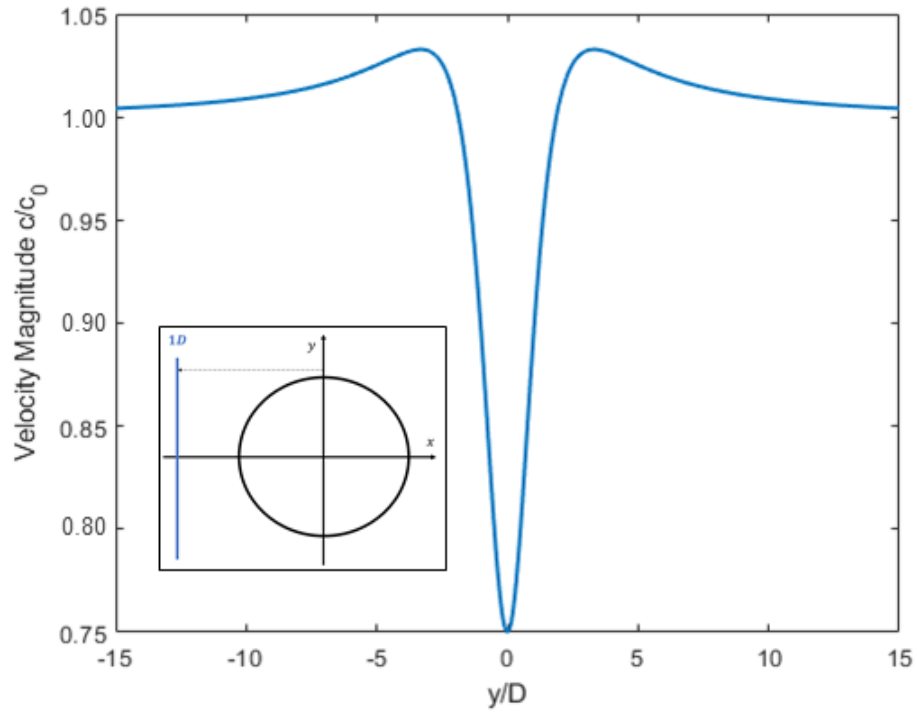


Figure 8.1: Velocity magnitude according to y/D for the plane $x = 1 \times \text{diameter}(D)$. Plotted using MATLAB.

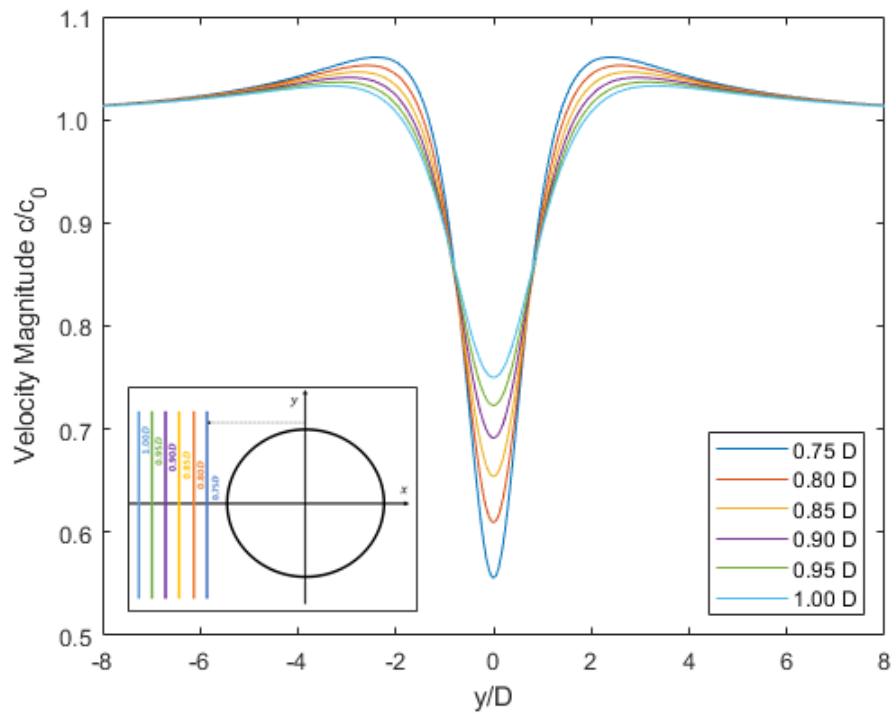


Figure 8.2: Velocity magnitude according to y/D for the planes $x = 1.5D, 1.6D, \dots, 2.0D$ (near-tower). Plotted using MATLAB.

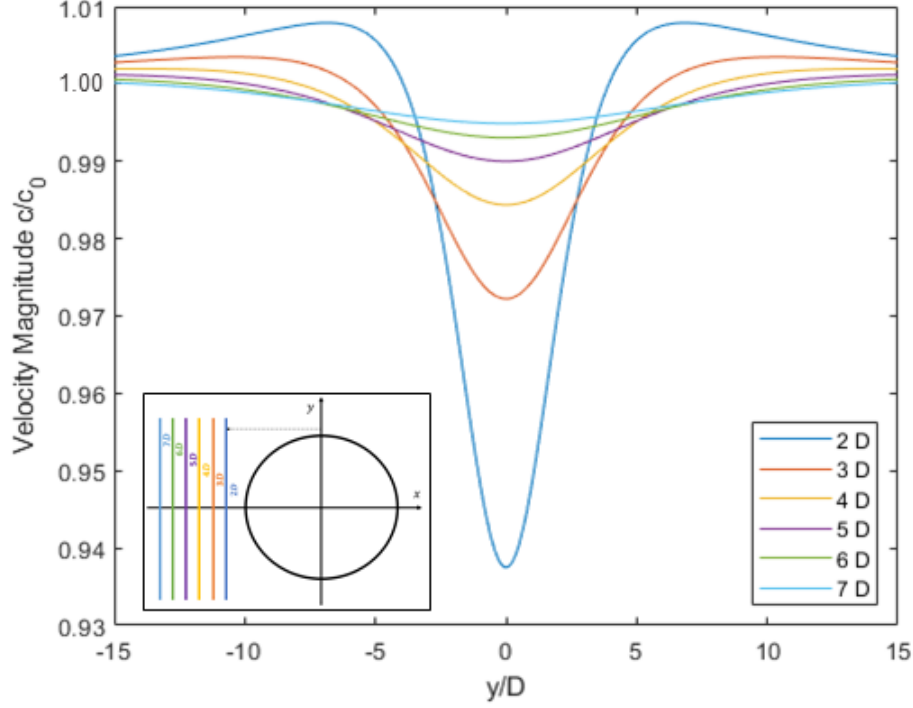


Figure 8.3: Velocity magnitude according to y/D for the planes $x = 2D, 3D, \dots, 7D$ (far-tower). Plotted using MATLAB.

Equations (8.2) and (8.3) relate the Cartesian velocity components with their polar counterparts in a simple and clear way. Nonetheless, it is desirable to also relate the Cartesian velocity components with Cartesian coordinates, as translated by Eq. (8.4) and (8.5) (normalized as to the free-stream undisturbed velocity, c_0):

$$\frac{c_x}{c_0} = 1 - \frac{(x^2 - y^2) R^2}{(x^2 + y^2)^2} \quad (8.4)$$

$$\frac{c_y}{c_0} = -2 \frac{xy R^2}{(x^2 + y^2)^2} \quad (8.5)$$

where, R is the tower radius.

These components can be represented schematically, as in Fig. 8.4, along with the relative velocity, $w = \sqrt{(u + c_y)^2 + c_x^2}$, and the circumferential velocity, $u = \lambda c_0$:

Fig. 8.4 allows us to equate a relationship between the absolute local wind velocity, c , and circumferential velocity, u , which, as previously mentioned (*vd.* Section 1.2.2), can be related through a dimensionless parameter that furthermore connects the circumferential velocity and the incoming undisturbed free-stream absolute velocity, the tip speed ratio, generally presenting global values between 6 and 9 [Hau 2013]. Despite this sizable range of values for λ , the calculations were performed for $\lambda = 7$, as this is typically the value for which maximal power output and loads are attained [Ragheb and Ragheb 2011], thus rendering studies for other values of λ unnecessary (this can be also verified by the BEM

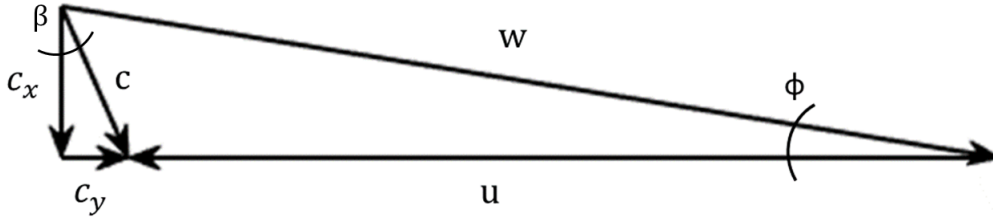


Figure 8.4: Decomposition of velocity vectors.

calculations performed by QBLADE in Chapter 7). We can define the tip speed ratio, resuming Eq. (1.1), in absolute terms as:

$$\lambda_0 = \frac{\omega r}{c_0} = \frac{u}{c_0} \quad (8.6)$$

which reverts locally to:

$$\lambda = \frac{u}{c} \quad (8.7)$$

Another important outtake from Fig. 8.4 is the clear introduction of an angle related to c_x and c_y , commonly referred to as *yaw angle*, β , which is the angle that the velocity vector, c , preforms with the stagnation streamline ($y = 0$). It is given by:

$$\beta = \arctan\left(\frac{c_y}{c_x}\right) \quad (8.8)$$

which can be presented in a more explicit relation as given by following equations:

$$c_x = c \cdot \cos \beta \quad (8.9)$$

$$c_y = c \cdot \sin \beta \quad (8.10)$$

We can then plot the variation of β along the y -axis for a given Ox plane (*vd.* Fig. 8.5), or several Ox planes (*vd.* Fig. 8.6).

It ought to be additionally noted that ϕ (*vd.* Fig. 8.4, an angle described between u and w , and not the potential function) isn't constant as, due to the changing nature of the yaw angle, β , c_x will increase/decrease, thus altering the value of ϕ , as proven by Eq. (8.11). As such, there is a relation between ϕ and β : $\phi = f(\beta)$.

$$\phi = \arctan\left(\frac{c_x}{u + c_y}\right) \quad (8.11)$$

It is now necessary to properly define the angle relations between the velocity decomposition previously schematized in Fig. 8.4 and the airfoil. Fig. 8.7 represents an airfoil whose chord line isn't collinear to the x -axis, but rather presents an angle, know as *twist angle*, γ . It also represents the angle of attack, α , in this case the angle between the relative velocity w and the chord line, but, instead of c being parallel to the y -axis,

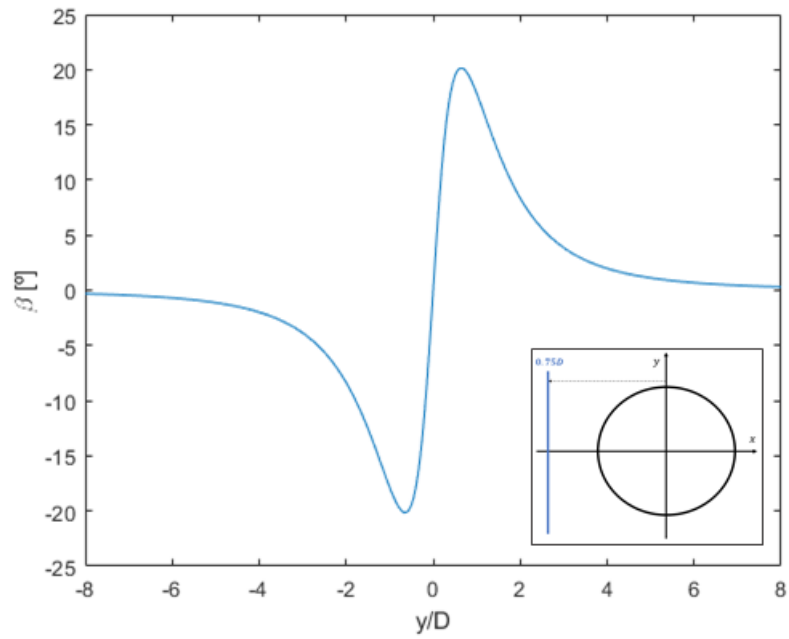


Figure 8.5: Yaw angle variation along y -axis for Ox plane $x = 0.75D$. Plotted using MATLAB.

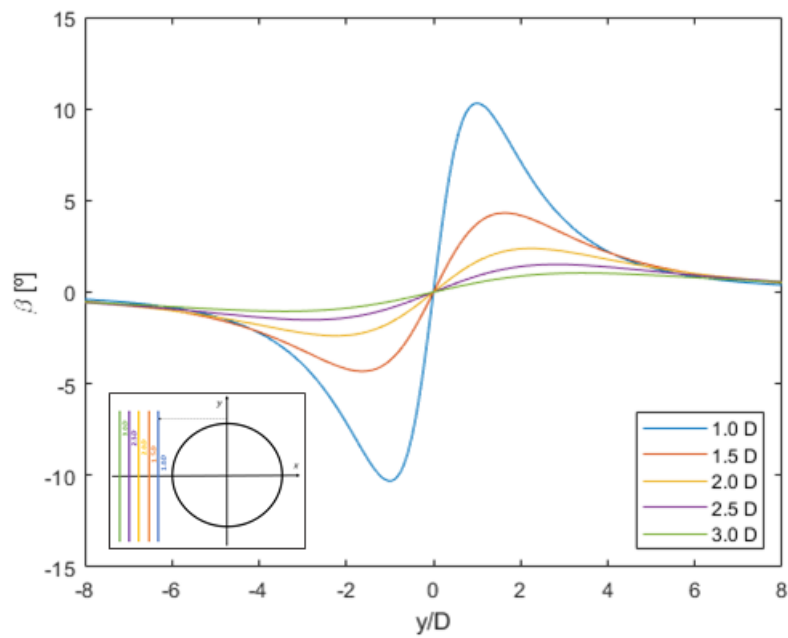


Figure 8.6: Yaw angle variation along y -axis for Ox planes $x = 1.0D, \dots, 3.0D$. Plotted using MATLAB.

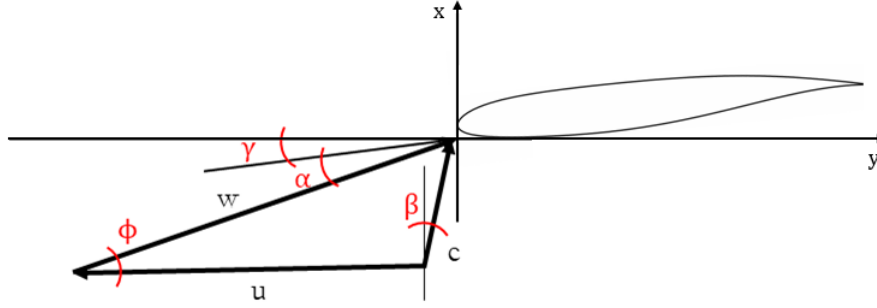


Figure 8.7: Schematic of decomposition of the absolute velocity and angle relations.

as in a far upstream situation, it possesses an angle, β , the aforementioned yaw angle. The presence of the yaw angle has, as previously discussed, an effect on ϕ .

Fig. 8.7, alongside Euclid's fifth postulate [Heath 1956], also known as the parallel postulate, can help us ascertain the relation between α and ϕ .

If we consider that $\gamma + \alpha + \Upsilon + \beta = \pi/2$, with Υ an aleatory angle described between w and the y -axis, and that $\Upsilon + \pi/2 + \phi + \beta = \pi$, we have a set of two equations which will, in the end, yield:

$$\alpha = \phi - \gamma \quad (8.12)$$

8.1 Coordinate System

Another step of the utmost importance is the way the coordinate system is formally defined, as this will affect the results and the way these can be physically understood.

Figure 8.8 details the axes selected (y up or to the right, x right or downwards facing), but also the definition of the level at which the calculations shall be realized.

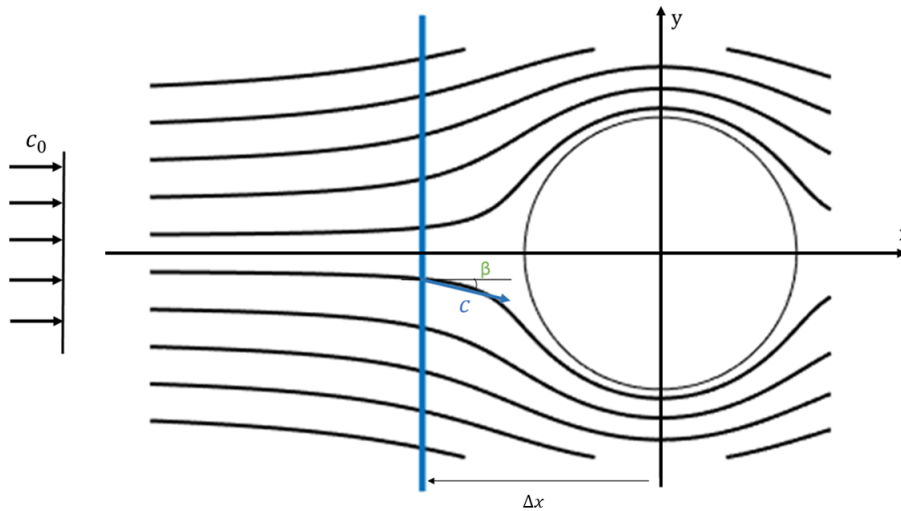


Figure 8.8: Decomposition of velocity vectors.

The reasoning behind the selection of this particular set of axes is two-fold: it was deemed desirable to have the x -axis pointing in the same direction as the inflowing velocity vector, c_0 , as this yields a positive value for the velocity, which has a physical meaning. The question of the level's physical meaning (represented by the blue line on the figure; on the negative region of the x -axis) isn't as pressing as the velocity's, as it represents dimensionless position relative to the tower ($\Delta x/D$). The second argument for the axes is concerned with the y -axis, and will be developed with the aid of Fig. 8.9.

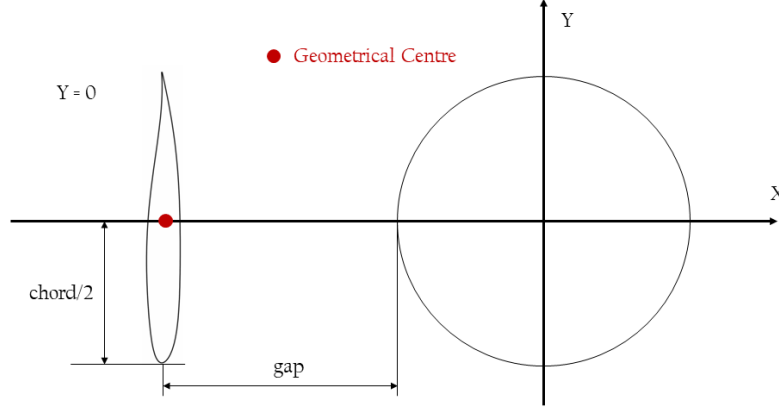


Figure 8.9: Definition of $y = 0$ in respect to airfoil.

As evidenced by the figure, it was arbitrated that $y = 0$ when the airfoil's geometrical centre is at $y = 0$ (as opposed to when the leading edge is at $y = 0$). This was select as the chord length was determined to be equal to the diameter, $L = D$, thus having a physical sense. The orientation of the y -axis selected is also related with the airfoil: if the airfoil has its leading edge pointing downwards (or left-pointing, if we rotate Fig. 8.9 $-\pi/2$), then its movement will be from up to down (or right to left in the $\pi/2$ rotated example), initiating its translational motion on the positive side of the y -axis.

It is additionally relevant to discuss the relationship between $\Delta x/D$, as exemplified in Fig. 8.8, and the gap (Fig. 8.9). Whilst $\Delta x/D$ establishes the Ox plane in relation to the centre of the tower, the gap comprises of the spacing between the tower and the airfoil, which seems to have, intuitively, more physical meaning. As such, they can be related through:

$$gap/D = (\Delta x/D - 1/2) \quad (8.13)$$

This relation can be transcribed to a useful look-up table, where both measurements are presented in the dimensionless form:

Table 8.1: Conversion table between $\Delta x/D$ and gap/D .

$\Delta x/D$	gap/D
0.5	0.0
1.0	0.5
1.5	1.0
2.0	1.5

8.2 Airfoil forces

The final convention that needs to be addressed is the one regarding the forces applied on the airfoil and their proper dimensionless form (*vd.* Fig. 8.10). It is known, from definition, that the lift force is perpendicular to the incoming relative velocity and the drag force its collinear, as represented in Fig. 8.10. Also noteworthy is the representation of the angle between the lift force and the y -axis (normal), ϕ .

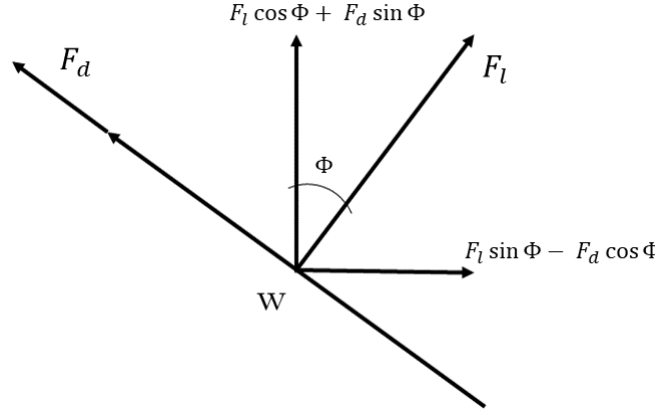


Figure 8.10: Generation of lift and drag.

Eq. (8.14) and (8.15) exemplify how one can obtain the lift- and drag force per unit of length, respectively, if the lift and drag coefficients are known beforehand. It ought to be noted that here the velocity employed in the formulae is the relative velocity, w , and L represents the chord length.

$$F_l = \frac{1}{2} \rho w^2 L C_l \quad [N/m] \quad (8.14)$$

$$F_d = \frac{1}{2} \rho w^2 L C_d \quad [N/m] \quad (8.15)$$

These forces can be expressed in terms of normal and tangential components, particularly relevant as they affect the deflection of the blades (through a bending moment) and the torque, respectively.

$$F_t = F_l \sin \phi - F_d \cos \phi \quad (8.16)$$

$$F_n = F_l \cos \phi + F_d \sin \phi \quad (8.17)$$

This can also be expressed in a dimensionless form, when normalized with respect to $1/2 \rho w^2 L$:

$$C_t = C_l \sin \phi - C_d \cos \phi \quad (8.18)$$

$$C_n = C_l \cos \phi + C_d \sin \phi \quad (8.19)$$

from which we have:

$$C_t = \frac{F_t}{\frac{1}{2}\rho w^2 L} \quad (8.20)$$

$$C_n = \frac{F_n}{\frac{1}{2}\rho w^2 L} \quad (8.21)$$

The tangential and normal coefficients are extremely important as they correlate with the torque and the loading of the tower respectively, integral to the understanding of the functioning and wear in wind turbines.

8.3 Intermediary Results and Model Validation

It is desirable to realize an intermediary validation of the model through the use of the MATLAB-XFOIL interface referenced in Chapter 6 in order to bring it into accordance with the selected coordinate system and conventions.

For this, preliminary intermediary results are attained for the Ox plane with a distance to the centre of the tower of $\Delta x/D = 1.5$, and thus a gap of $1D$, selected as to purportedly be in accordance with the clearance typically found in modern HAWTs. The absolute undisturbed free-flow velocity is also defined as $c_0 = 10$ [m/s] (relevant for the Reynolds number calculation and relative to the leading edge), the chord length was set to be equal to the diameter of the tower ($L = D$), and the twist angle made 0° ($\gamma = 0^\circ$).

We can start by analyzing Fig. 8.11, which shows us the evolution of the absolute velocity x -axis component normalized in relation to the undisturbed free-stream velocity, c_x/c_0 , along the y -axis for the fixed value of a gap of one tower diameter.

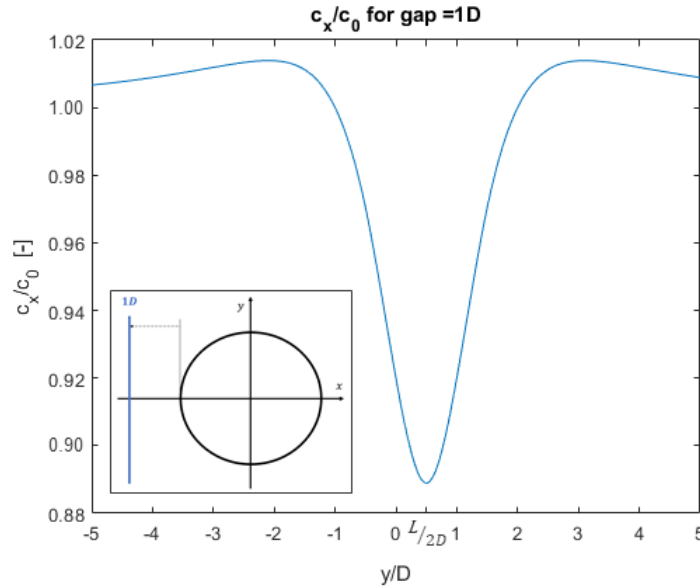


Figure 8.11: Value of c_x/c_0 along y -axis for a gap of $1D$.

It is visible afar in the y -axis, where the effect of the tower on the flow is more reduced, that c_x/c_0 tends to converge to the unity, clearly in accordance with what is previously postulated. We can formally prove this through the development of Eq. (8.4), in which we commence by normalizing the values for x and y by dividing by R :

$$\frac{c_x}{c_0} = 1 - \frac{\left(\left(\frac{x}{R}\right)^2 - \left(\frac{y}{R}\right)^2\right)}{\left(\left(\frac{x}{R}\right)^2 + \left(\frac{y}{R}\right)^2\right)^2} \quad (8.22)$$

Now, as we are in a Ox plane, we have a constant value for x , which, for simplicity's sake is chosen as $x = R$ (we also substitute y/R with y^*). We get:

$$\frac{c_x}{c_0} = 1 - \frac{1 - y^{*2}}{(1 + y^{*2})^2} \quad (8.23)$$

After this step, only one final transformation of the original equation is necessary, *i.e.*, dividing by y^{*4} :

$$\frac{c_x}{c_0} = 1 - \frac{\frac{1}{y^{*4}} - \frac{1}{y^{*2}}}{\left(\frac{1}{y^{*4}} + \frac{1}{y^{*2}}\right)^2} \quad (8.24)$$

We can finally determine the $\lim_{y^* \rightarrow \infty} c_x/c_0$ (the limit calculation steps are suppressed), whose physical meaning is the y -afar value of c_x/c_0 :

$$\lim_{y^* \rightarrow \infty} \frac{c_x}{c_0} = 1 \quad (8.25)$$

Thus, through Eq. (8.25), we can explain the evolution of the function $f(x) = c_x/c_0$ far from the tower and its convergence to unity, which is somewhat already intuitively known.

Apart from this behaviour in the far-field, two phenomena near-tower become apparent: there is dip in the value of the function c_x/c_0 , reaching it's minimal value at the stagnation streamline, as expected. It is also noticeable a rise of the value of c_x/c_0 before the plummet close to the stagnation streamline. As with the discussion in Fig. 8.2 and 8.3, the increase of velocity close to the minimal value is due to the concentration of streamlines next to the top and bottom of the tower cut-section. Fig. 8.11 also presents positive values, in conformity with the formulation presented in Fig. 8.8.

Perhaps the most interesting feature of this figure is its shifting towards the right by a factor of $L/2D$, which is in full accordance with the formulation outlined by Fig. 8.9: when the translation of the airfoil is considered and $Y = 0$ is held for the geometrical centre of said airfoil, then there is a shifting of the graph, and it is apparent that the airfoil faces 'sooner' the minimal velocity value. Nevertheless, there is a clear symmetry in relation to the $y = L/2D$ line.

The ensuing figure (*vd.* Fig. 8.12) emulates Fig. 8.11, but, instead of c_x/c_0 , it presents the normalized absolute velocity y -axis component, c_y/c_0 .

Again, there is an apparent positive shifting of the graph of $L/2D$ and a symmetry in regard to the $y = L/2D$ line, as well as an evident accordance with the axes selected

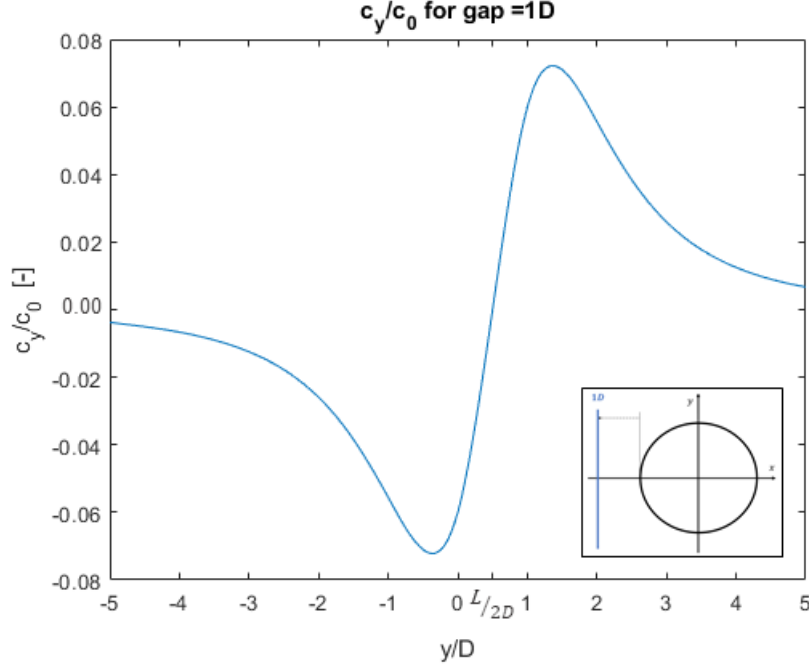


Figure 8.12: Value of c_y/c_0 along y -axis for a gap of $1D$.

in Fig. 8.8, as the graph also presents positive values for c_y in the positive part of the y -axis.

The convergence afar to 0 is also expected (proven as with c_x/c_0 , but beginning with Eq. (8.5), normalizing it and solving the limit $\lim_{y \rightarrow \infty} c_y/c_0$, which equals zero), along with the drastic increase and decrease in the proximity of the tower: as the yaw angle increases, so does the y velocity component (*vd.* Eq. (8.10)); however, close to the stagnation streamline this value drops as the absolute velocity is near zero. Most notably, there is an explicit connection between Fig. 8.12 and Fig. 8.5, thus further evidencing the clear influence of the yaw angle, β , in the y velocity component.

Another relevant intermediary output that completely mirrors Fig. 8.11 and is reminiscent of Fig. 8.1, is the absolute velocity magnitude variation along the y -axis, showed in Fig. 8.13 in a dimensionless form.

For the specific case of a gap of one tower diameter (c/c_0 at $x = 1.5D$) we can verify that there is a slight increase on the relative magnitude of the velocity of close to 1 % in near-tower and a dip of over 10 % at the potential flow stagnation streamline.

Another interesting point to be made is the evident mirroring of c_x present in the c/c_0 graph, which is explained by the magnitude of the yaw angle: for a $1D$ gap the maximal value of β is approximately 5° (*vd.* Fig. 8.6). Considering $c_x = c \cdot \cos \beta$ (Eq. (8.9)), in this specific case ($\beta = 5^\circ$), $c_x = 0.996 \cdot c$, thus explaining the apparent lack of influence of c_y (it ought to be further noticed that, even for the case of a Ox plane closer to the tower, as $\Delta x/D = 1$, which is the same as $gap/D = 0.5$, the maximal value of β will be close to 10° , whose cosine is 0.98, allowing us to extrapolate these assumptions for other planes, closer to the tower).

The final result one can utilize to verify the physical accordance of the model with

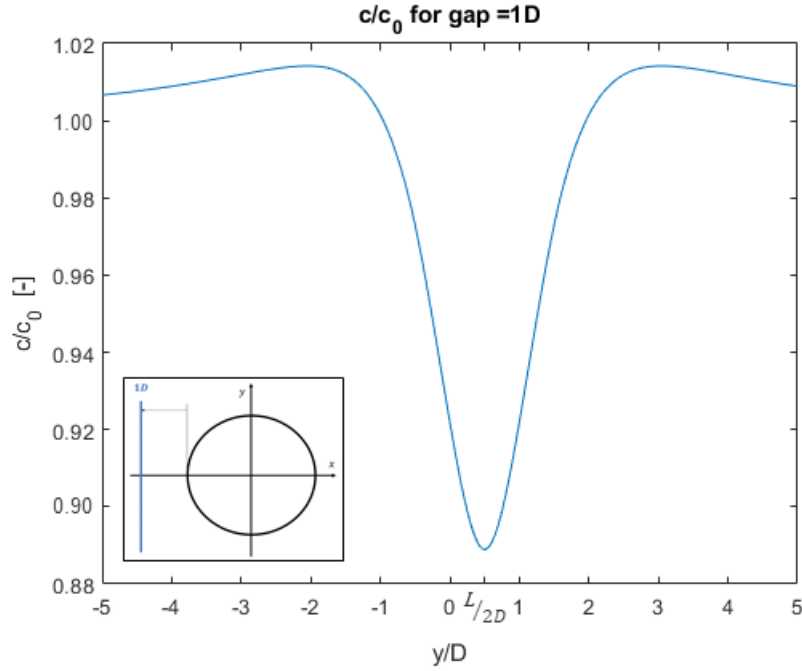


Figure 8.13: Value of c/c_0 along y -axis for a gap of $1D$.

the selected conventions is the progression of the angle of attack's value along the y -axis for a specific gap (*vd.* Fig. 8.14).

The aforementioned graph shifting is again evident in Fig. 8.14, as its minimum is attained for $y = L/2D$. There is also a clear convergence afar from the tower to a value of approximately 8.13° , identified on the y -axis of the graph as ϕ_0 . This is the value of ϕ for the undisturbed free-flow case, in which, returning to Eq. (8.11), $c_x = c_0$ and $c_y = 0$. We thus obtain $\phi = \arctan(1/7) = 8.13^\circ$. Considering Eq. (8.12) and that we've performed the calculations for a twistless case ($\gamma = 0$), we have $\alpha = \phi$.

Most interestingly, there is a clear asymmetry regarding the $y = L/2D$ line, as the left-side peak is noticeably higher than the right-side one, which hadn't been the case for the figures previously presented. This is better understood through the aid of Fig. 8.15.

Starting on the right-side of the figure, one would assume that, as the yaw angle, β , increases, so does c_x decrease, which would lead us to think that there would be a steady decrease of the value of α from ϕ_0 to the minimum, achieved at $L/2D$. However, we must also take into account that the absolute velocity magnitude also increases near-tower, as evidenced by Fig. 8.13. Naturally, as the velocity magnitude decreases, so does α . Even though in the stagnation streamline $\beta = 0$ (which means that $c = c_x$, no y component), due to the stark decrease of the velocity magnitude, this effect is not felt.

On the left-side of the y -axis there is an inversion on the sign of c_y , which will be negative. This inversion, combined with the fixed nature of u , means that there is an increase of ϕ , especially when compared to the right-side of the y -axis. Thus, the asymmetry is explained. As the flow is evaluated in positions increasingly more distanced from the tower, the yaw angle tends to zero (*vd.* Fig. 8.5), which in turn lead α to converge to the value of ϕ for c_0 (ϕ_0).

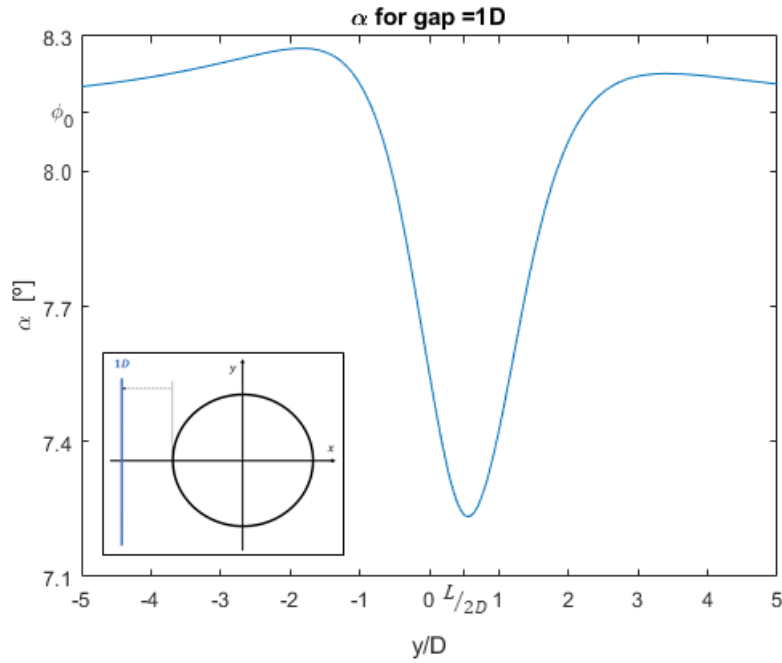


Figure 8.14: Value of α along y -axis for a gap of $1D$.

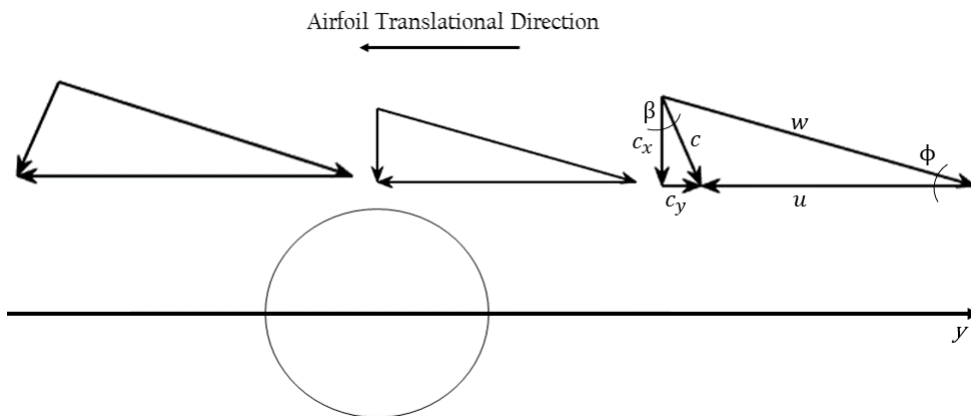


Figure 8.15: Variation of velocity vector components along y -axis.

Chapter 9

Results

In this section, the results acquired from the MATLAB-XFOIL-interface in Chapter 6 are presented and duly analyzed for their physical significance. These are performed for 4 different distances to the tower centre $x = 0.5D, 1.0D, 1.5D$ and $2.0D$, which can be expressed as gaps: $0.0D, 0.5D, 1.0D$ and $1.5D$.

One interesting idiosyncrasy of the model in its generality that is best mentioned sooner than later is an apparent paradox: this model adopts, simultaneously, an inviscid and a viscid formulation in its coupling, as the potential flow solutions around the tower neglect the viscous effects, but XFOIL's polar accumulation is predicated upon the existence of a viscous flow. Nevertheless, this isn't as grave as it might seem on a first look, as the potential flow solutions serve as boundary conditions for XFOIL's calculations, thus removing the paradoxical nature of this riddle.

9.1 Sensibility Study

Initially, a sensibility study was performed to understand the effect the change of explanatory variables have on the input variables of XFOIL.

There are two input variables that radically change the results attained through the use of XFOIL: the Reynolds number, Re , and the angle of attack, α . As clearly outlined by Eq. (8.12), there is an equivalency between α and ϕ (for a twistless case, $\alpha \equiv \phi$) and, thus, a dependency between α and β , $\rho(\alpha, \beta)$, where, following probability theory's nomenclature [Aitken 1942], ρ represents correlation. Regarding the Reynolds number, considering Eq. (4.7), we have $Re \propto w$.

With this in mind we can verify the impact the tower has on the values of the Reynolds number and angle of attack through the calculation of the coefficient of variation and the range, expressed in terms of a percentage.

The coefficient of variation is defined as the ratio between the standard deviation, σ , and the mean, μ [Everitt and Skrondal 2010]. Nevertheless this formula is slightly altered to accommodate the idiosyncrasies of this case. As such, the standard deviation is calculated for the set of the i -number of Reynolds numbers (in Eq. (9.1), Re is this data set), but the mean is substituted by the Reynolds number of the airfoil in a tower-free case ($Re_{undisturbed}$):

$$CV = \frac{\sigma(Re)}{Re_{undisturbed}} \quad (9.1)$$

The range [Everitt and Skrondal 2010] expressed in percentage, is usually calculated as:

$$T(\%) = \frac{|\max(x) - \min(x)|}{\mu(x)} \quad (9.2)$$

In this particular application it shall be:

$$T(\%) = \frac{|\max(Re) - \min(Re)|}{Re_{undisturbed}} \quad (9.3)$$

We can now express these values in a table for the different gaps.

Table 9.1: Coefficient of variation and range according to gap for Reynolds number and angle of attack.

Gap	Variable	CV(%)	T(%)
0.0D	<i>Re</i>	2.36	13.00
	α	23.0158	114.3804
0.5D	<i>Re</i>	0.99	4.49
	α	6.9349	28.7363
1.0D	<i>Re</i>	0.54	1.99
	α	3.6789	12.7233
1.5D	<i>Re</i>	0.35	1.13
	α	2.30	7.16

Table 9.1 clearly singles out the preponderance of variation on the angle of attack when compared to the Reynolds number: when we compare the coefficients of variation of both, α is, on average, about 7 times greater than the Reynolds number, which signifies that the variation is much greater for α than for *Re*. This leads us to deduce that the variation of the angle of attack (and implicitly, the yaw angle) is more relevant than the variation of the Reynolds number (and implicitly, the relative velocity).

9.2 Lift and Drag Coefficients

The first outcomes from XFOIL we plot using MATLAB are the lift and drag coefficients, C_l and C_d , respectively.

Figures 9.1 and 9.2 represent the C_l vs α curve and its close up for $gap/D = 1$. These curves were calculated separately from the main 'for' loop with the help of XFOIL for a Reynolds number of approximately 9389082, which represents the mean value of the Reynolds numbers used in the i -iterations, \overline{Re} . The values of α were selected as to allow a full-bodied representation of the C_l vs α curve, as well as preventing XFOIL from not reaching viscal convergence due to separation (this term, *viscal convergence* not reached, appears in XFOIL when no convergence is found for the solution of the linear equations system at the b -Newton-Raphson-iteration as it is operating in the viscous mode).

Additionally, 3 values from the curve are highlighted by circles: the red circle represents the value of the lift coefficient for α_0 , which is the angle of attack for the undisturbed

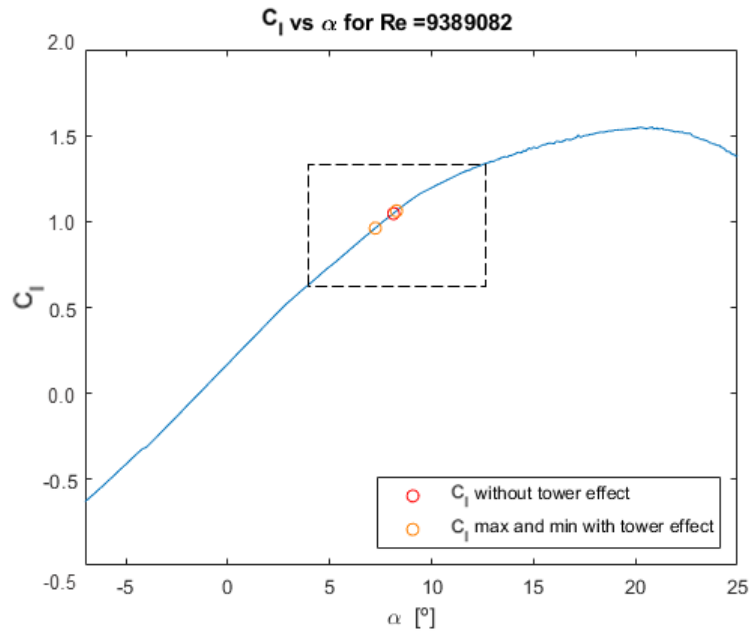


Figure 9.1: C_l vs α full curve for $-7^\circ \leq \alpha \leq 25^\circ$. Plotted using MATLAB. The dashed box represents the close-up zoomed area.

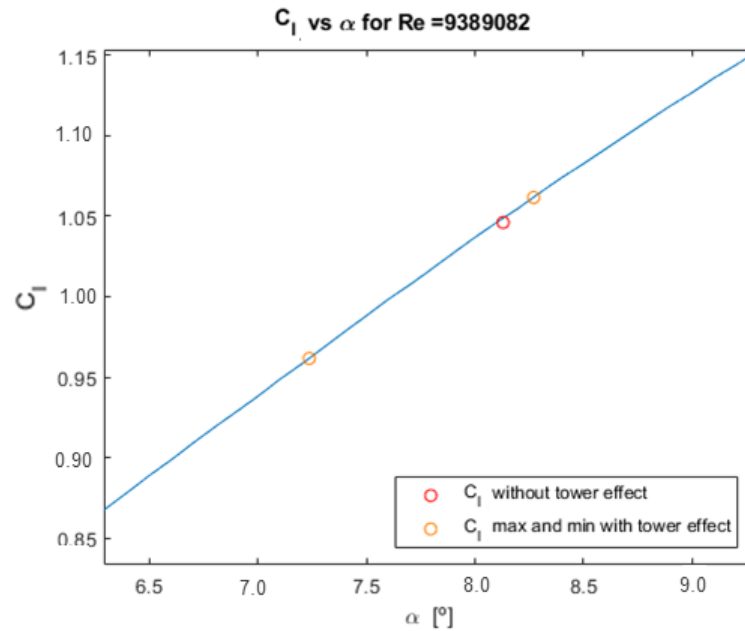


Figure 9.2: C_l vs α graph close-up. Plotted using MATLAB.

case (there is no presence of the tower, $\alpha_0 = \phi_0$). The orange circles represent the maximal and minimal values of C_l for the maximal and minimal α , respectively, as, in this region of the curve, there is a fair degree of linearity.

We can interpret these graphs as the following: instead of facing a single, 'original' value of α and thus having just one C_l (in red), the presence of the tower will make the airfoil face a varying range of α , producing different values of C_l (the values of the curve delimited by the orange circles).

There are, obviously, values of C_l which will actually exceed the undisturbed case ($C_{l,0}$), as can be inferred from Fig. 8.14 and 8.13, as there is a surge due to bigger velocity magnitude on the left-side of the tower, but this effect is relatively slight, when one considers how close $C_{l,max}$ and $C_{l,0}$ are ($C_{l,max}$ is 3.96 % superior to $C_{l,0}$). What is far more noticeable is the $C_{l,min}$, which is considerably inferior to $C_{l,0}$, as $C_{l,min}$ is 24.79 % inferior to $C_{l,0}$.

This seems to be in line with initial considerations [Dolan and Lehn 2006], as the decrease of the lift coefficient is directly related to the power output (there is also a dependency on the drag coefficient, but it isn't as relevant due to its smaller magnitude): Power is directly connect both with lift and drag ($P_t = F_t \cdot u$, where the F_t is the tangential force).

The same methodology has been applied to different gaps, as prescribed in the beginning of Setion. 9, which can be seen in Fig. 9.3 and 9.4:

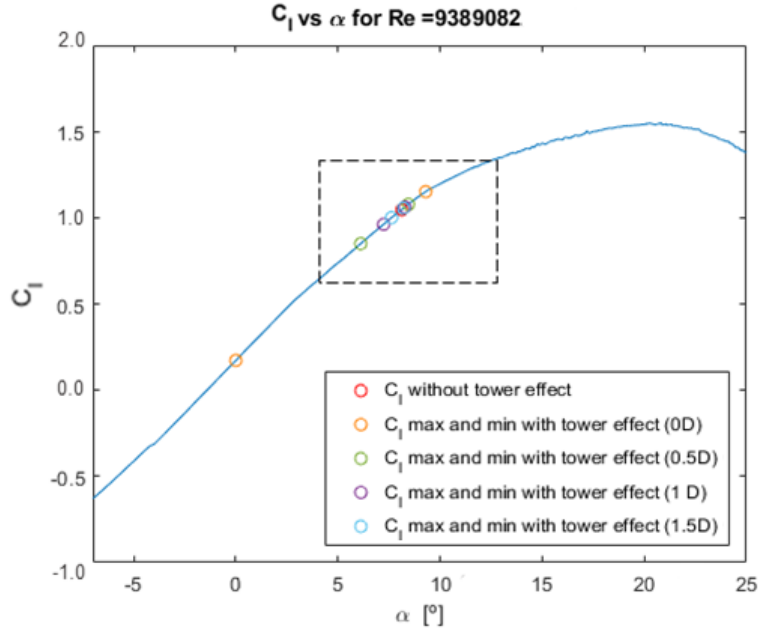


Figure 9.3: C_l vs α full curve for $-7^\circ \leq \alpha \leq 25^\circ$ with limit values for C_l , for several gaps. Plotted using MATLAB. The dashed box represents the close-up zoomed area.

What becomes evident from the analysis of both figures is the progressive distancing of the maximum and minimum points as the gap decreases, which again reaffirms the strong correlation between the decrease of velocity and increase of variation of α caused by the ever-closer presence of the tower, with the widening of the range of values of C_l , becoming all the more relevant as the increase of C_l is rather meek when compared to

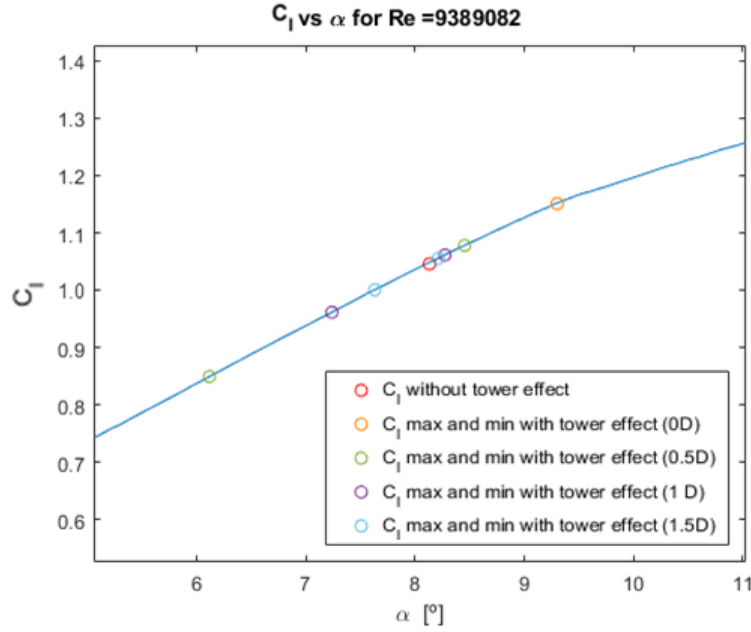


Figure 9.4: C_l vs α close-up with limit values for C_l for several gaps. Plotted using MATLAB. *N.b.*, $C_{l,min}$ for $gap = 0D$ hasn't been presented, as it would hinder the visualization of the other circles.

its decrease. This is further evinced by Table 9.2, which compares the percentage of increase of the maximal lift coefficient and the percentage of decrease of the minimal lift coefficient, considering the undisturbed case as the benchmark:

Table 9.2: Maximum and minimum lift coefficient increase/decrease in relation to undisturbed value.

gap/D	Variable	Increase/Decrease (%)
0.0	$C_{l,min}$	-83.51
	$C_{l,max}$	10.03
0.5	$C_{l,min}$	-24.79
	$C_{l,max}$	3.96
1.0	$C_{l,min}$	-8.07
	$C_{l,max}$	1.48
1.5	$C_{l,min}$	-4.34
	$C_{l,max}$	0.91

The same procedure has been applied to the drag coefficient (*vd.* Fig. 9.5 and 9.6), which mirrors the behaviour of the lift coefficient: the reduction of the gap induces an increase on the range of values of the angle of attack and subsequently, on the values of the drag coefficient. It is again evident that the increase of the drag coefficient is less severe than the stark decrease it faces.

A table analogous to Table 9.2 has been produced, as to allow a better understanding of the range widening phenomenon.

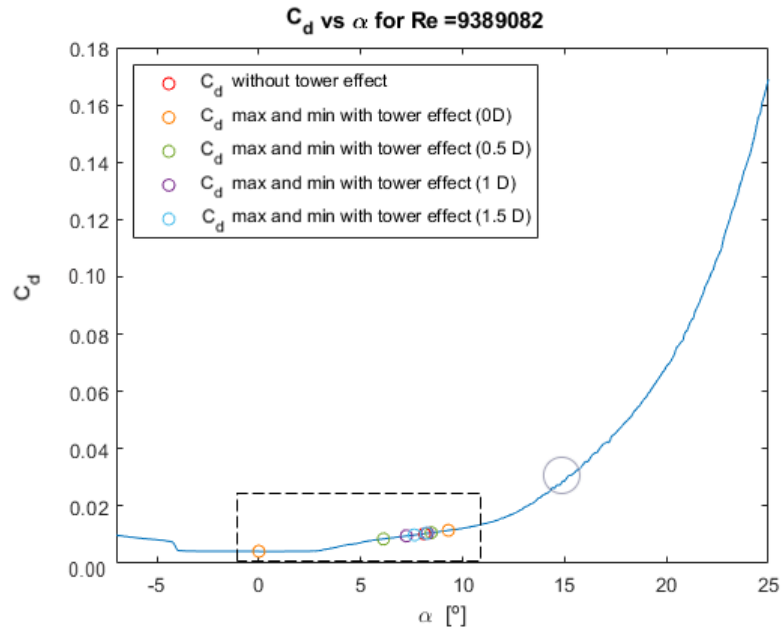


Figure 9.5: C_d vs α full curve for $-7^\circ \leq \alpha \leq 25^\circ$ with limit values for C_d for several gaps. Plotted using MATLAB. The dashed box represents the close-up zoomed area.

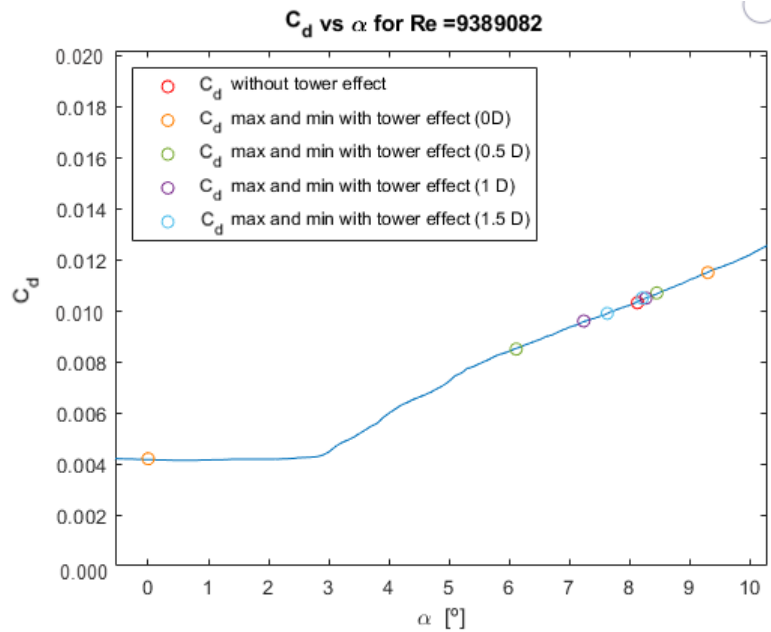


Figure 9.6: C_d vs α close-up with limit values for C_d for several gaps. Plotted using MATLAB.

Table 9.3: Maximum and minimum drag coefficient increase/decrease in relation to undisturbed value.

gap/D	Variable	Increase/Decrease (%)
0.0	$C_{d,min}$	-59.22
	$C_{d,max}$	11.65
0.5	$C_{d,min}$	-17.48
	$C_{d,max}$	3.88
1.0	$C_{d,min}$	-6.80
	$C_{d,max}$	1.94
1.5	$C_{d,min}$	-3.88
	$C_{d,max}$	1.94

The upshots that become apparent from the comparison of Table 9.2 and 9.3 are two-fold: even though the percentage of increase on both the lift and drag coefficients are essentially aligned, the drag coefficient presents, nevertheless, a slightly stronger increase than the lift coefficient.

The other core outcome is the evident misalignment of the percentual decrease values between the lift and drag coefficients: the decrease of lift is notoriously steeper than the decrease of drag.

This further reinforces the assumption that the power output will be negatively affected by the presence of the tower.

9.3 Tangential- and Normal Coefficients

With the aid of Eq. (8.18) and (8.19), we can plot the normal and tangential force coefficients along the y -axis, as illustrated by Fig. 9.7 and 9.8.

The analysis of these graphs paints a clear picture: both Fig. 9.8 and 9.7 have obvious connections with the angle of attack graph, Fig. 8.14. These similarities are namely: the $L/2D$ shifting towards the positive spectrum of the y -axis, the strong reduction of the value in near-tower situations and the vertical asymmetry (as to the $y = L/2D$ line), most evident for the higher values of the curve on the left side before the plummet.

An interesting take-away from the comparison between both of these graphs is the higher value of the normal coefficient when juxtaposed to the tangential coefficient ($C_n > C_t$), which can be explained through the smallness of α/ϕ , due to the chosen value for the tip speed ratio ($\lambda = 7$, with $C_n \approx 7 \times C_t$). We can, finally, present the C_n and C_t graphs for different gaps (*vd.* Fig. 9.10 and 9.9), where it is evident the influence the proximity to tower has on the normal and tangential components.

There is certainly some validity to the model as, for a case in which there's no gap ($gap = 0D$), the tangential coefficient is equal to zero at the stagnation streamline, which is in accordance with what was previously theorized and expressed by the graphs (no velocity implies no lift). Also, with each increased level, farther away from the tower, the impact that negatively affects both coefficients wanes (for example, from a 100% decrease of C_t at $gap = 0D$ to a 14 % decrease at $gap = 1.5D$), as does the degree of asymmetry, which becomes increasingly less noticeable with each gap farther away from the tower.

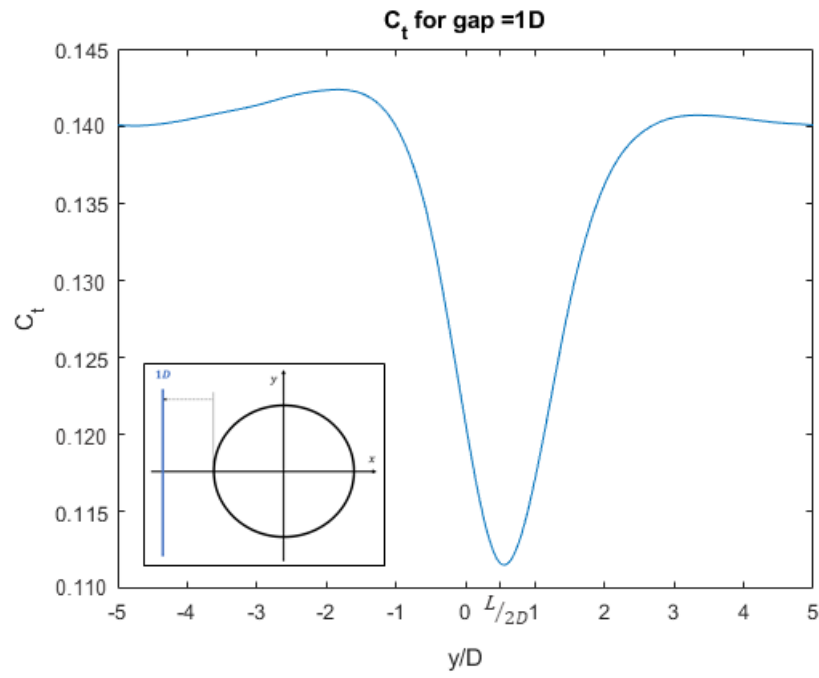


Figure 9.7: Value of C_t along y -axis for $gap/D = 1$.

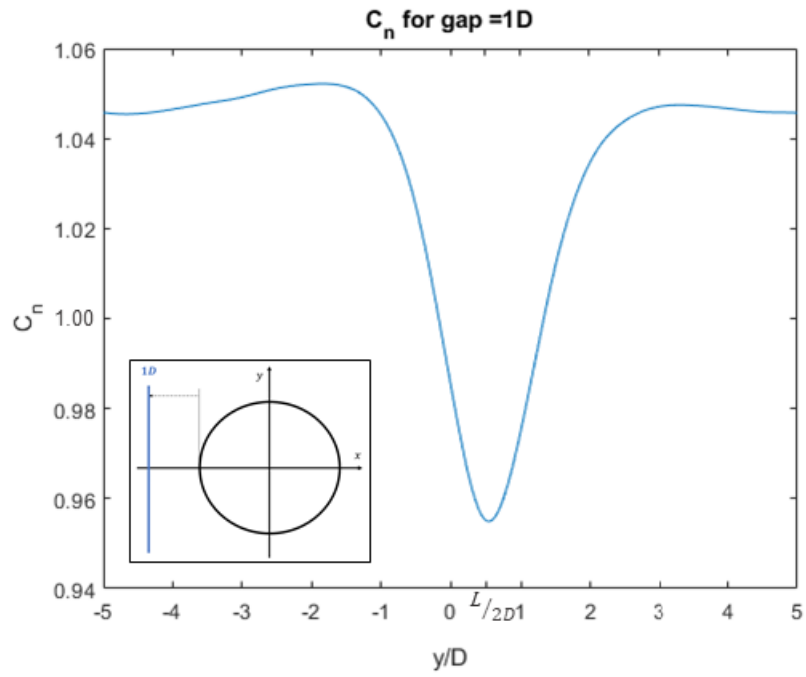


Figure 9.8: Value of C_n along y -axis for $gap/D = 1$.

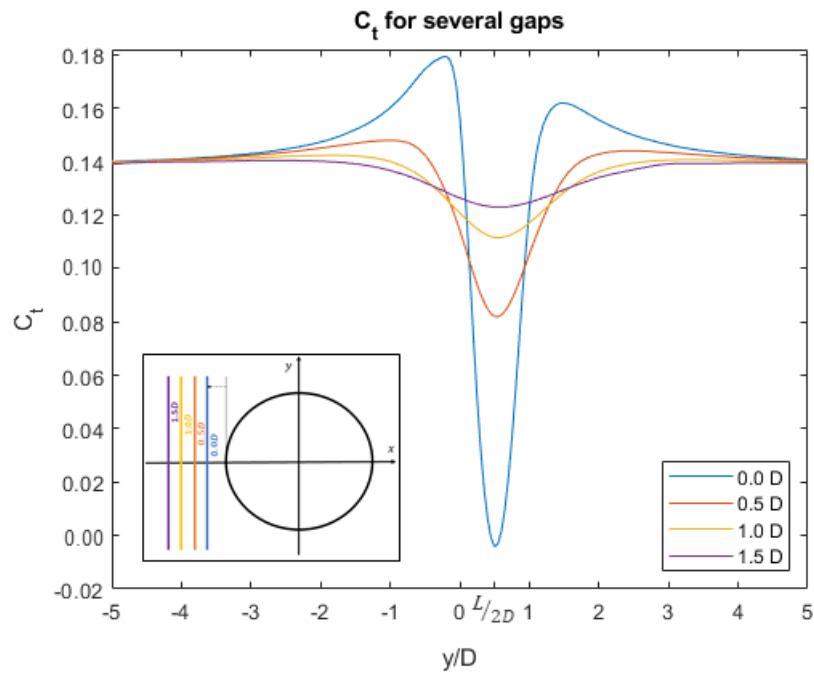


Figure 9.9: Comparison of C_t values along y -axis for different gaps.

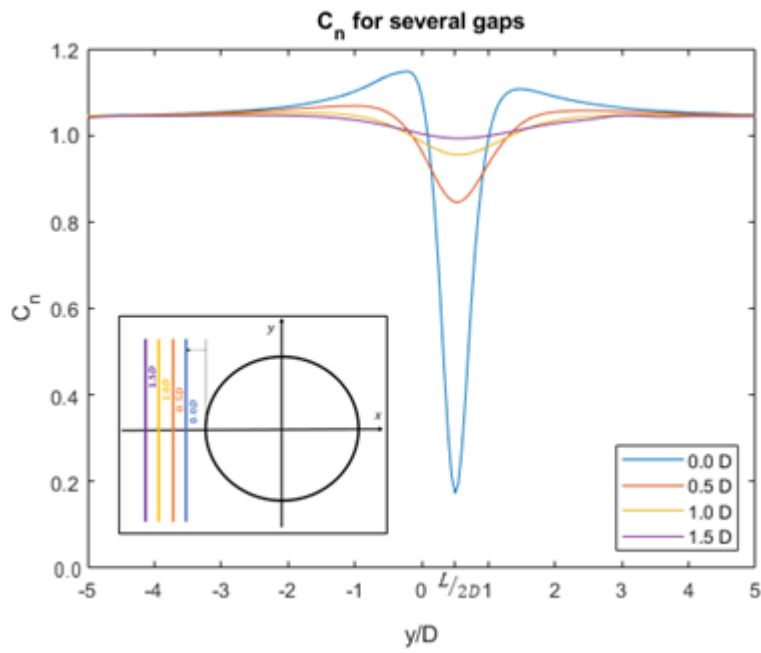


Figure 9.10: Comparison of C_n values along y -axis for different gaps.

9.4 Twist Angle

It is now relevant to introduce variations into the tower interference model initially studied, since, as previously established, it is based on simplifying physical notions, but nevertheless, has the ability of allowing a deeper study of some of the specificities that arise from the tower interference-related phenomena through quick alterations/add-ons on the MATLAB-XFOIL interface.

An important commencing step into the enlargement of the study initially carried through is the inclusion of non-zero values for the twist angle, as, not only is its influence accounted for in Eq. (8.12), but also, there are changes on the twist angle after the on-location assembly of the blades onto the hub (which collectively form the rotor). This has been the subject of considerable literature which addresses the twist angle mostly through the lens of spanwise optimization [Liu *et al.* 2013], or the effect it has on model-building [Chaviaropoulos and Hansen 2000], as it is a recurring parameter of interest for most WECS applications, and its change is generally taken into account.

It is, nevertheless, of the greatest importance to properly differentiate between the concept of spanwise twist angle and changes to the twist angle begotten by assembly. While the spanwise twist angle is accounted for, as it is employed along the blade to allow the different airfoils composing it to optimally face varying angles of attack (we've operated under a fixed tip speed ratio, λ , however, if one moves along the blade its value is changed, thus having an impact on the value of α), assembly induced alterations to the twist angle on a particular level (λ constant) aren't desirable and the study of the newly arisen results is important to paint a fuller picture.

It was thus deemed that, after the initial twistless case, two additional full simulations for $gap = 1D$ with $\gamma = -1^\circ$ and $\gamma = 1^\circ$ would be sufficiently representative as working with the unity simplifies extrapolations and interpretations (though exact industry tolerance norms or guidelines are unknown to the author, the figure of $\pm 0.3^\circ$ has nevertheless been referenced through conversation as a common value).

The full C_l vs α and C_d vs α curves (as well as close-ups of said curves) resulting from the aforementioned simulations are presented in Fig. 9.11 - 9.14. Much like in Section 9.2, a set of coloured circles representing the expected lift and drag coefficients are also drawn. The red circle is the expected coefficient in a towerless case, which ought to be interpreted as the benchmark value. All other circles are actually pairs that represent the maximal and minimal values of the coefficients (we can think of them as the upper and lower limits of the section of the curve scanned during the tower-including simulation).

Unlike Fig. 9.4 and 9.6 we can't speak of an expansion/contraction of the scanned sections of the curve as with each new gap, but rather a shifting of the initial limits (represented by the purple circles, $\gamma = 0^\circ$) right- or leftwards, depending on the twist angle. The shifting that occurs is, naturally, of exactly one degree: if we again consider Eq. (8.12) we can observe that α is negatively related to γ ; consequently, a positive value for the twist angle will reduce the value of the angle of attack, as observable in Fig. 9.12 and 9.14 (for $\gamma = 1^\circ$, the green circles, there is a leftward shifting, indicating the $\alpha - 1^\circ$ reduction). Conversely, for a negative value of γ , we shall have $\alpha + 1^\circ$, and thus, a rightward shifting as evidenced by the orange circles.

The influence of the twist angle can more clearly be ascertained by inspecting Fig. 9.15, which presents the curves for the angle of attack for different twist angles. As expected, all three curves are identical (same y -axis $L/2D$ rightward shifting, vertical

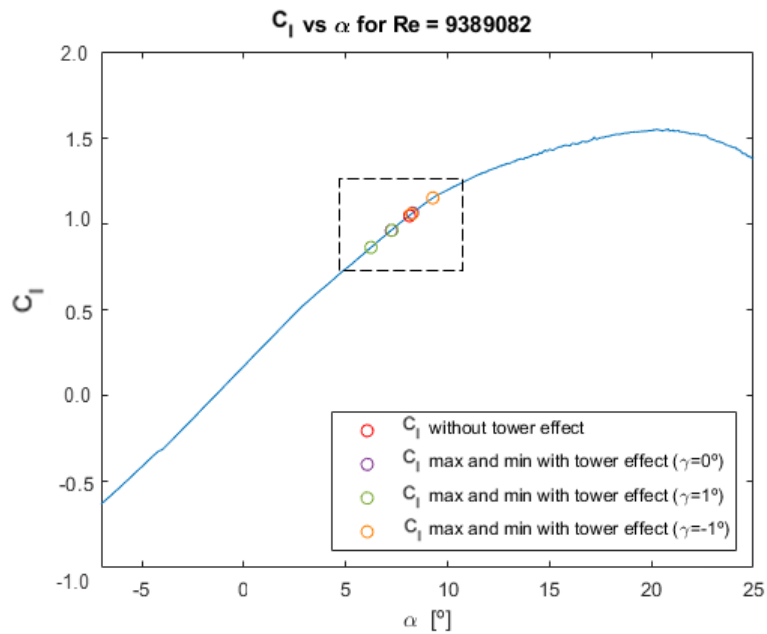


Figure 9.11: C_l vs α full curve for $-7^\circ \leq \alpha \leq 25^\circ$ with limit values for C_l , for some twist angles, γ . Plotted using MATLAB. The dashed box represents the close-up zoomed area.

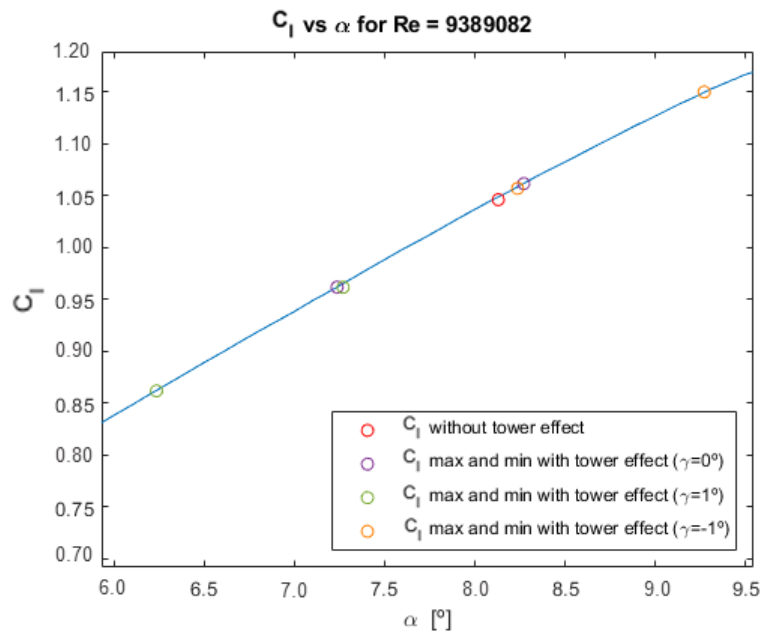


Figure 9.12: C_l vs α close-up with limit values for C_l , for several twist angles, γ . Plotted using MATLAB.

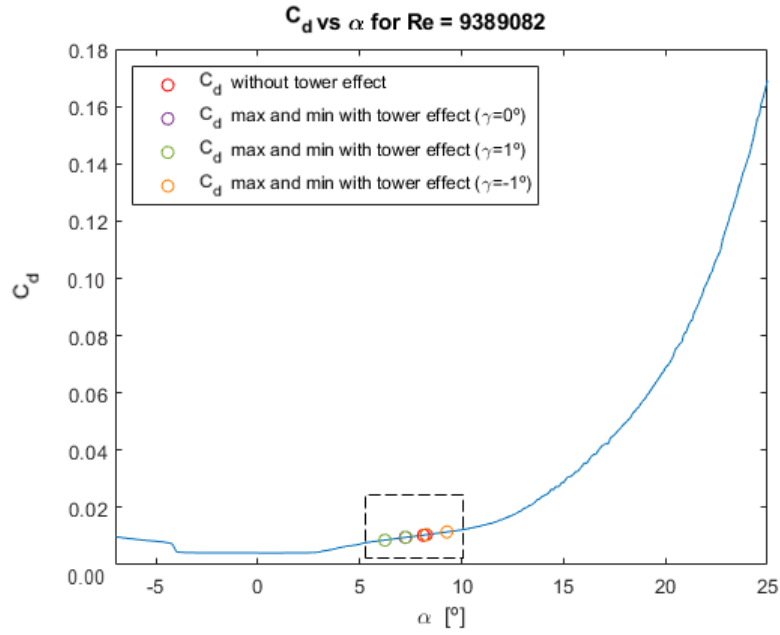


Figure 9.13: C_d vs α full curve for $-7^\circ \leq \alpha \leq 25^\circ$ with limit values for C_d , for some twist angles, γ . Plotted using MATLAB. The dashed box represents the close-up zoomed area.

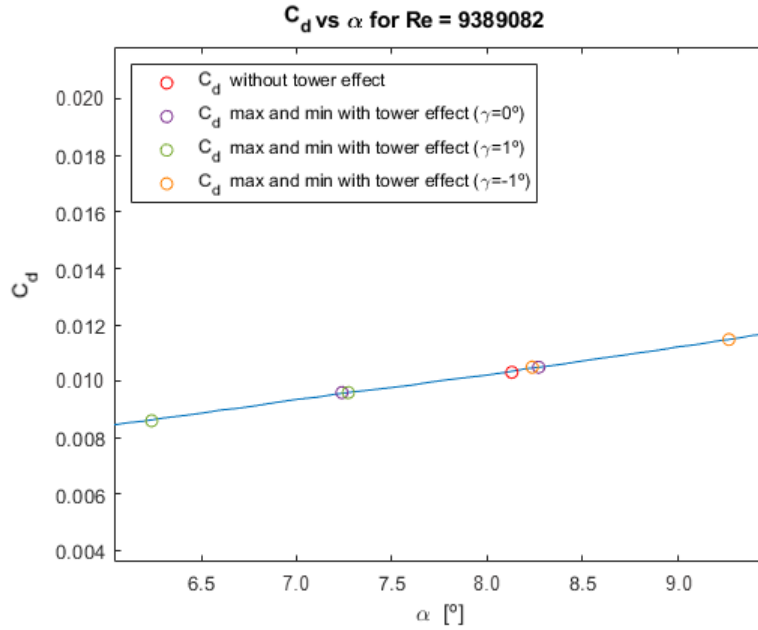


Figure 9.14: C_d vs α close-up with limit values for C_d , for several twist angles, γ . Plotted using MATLAB.

asymmetry and near-tower plummet), but with the noticeable difference of a vertical shifting of the graph (upwards for $\gamma = -1^\circ$, downwards for $\gamma = 1^\circ$).

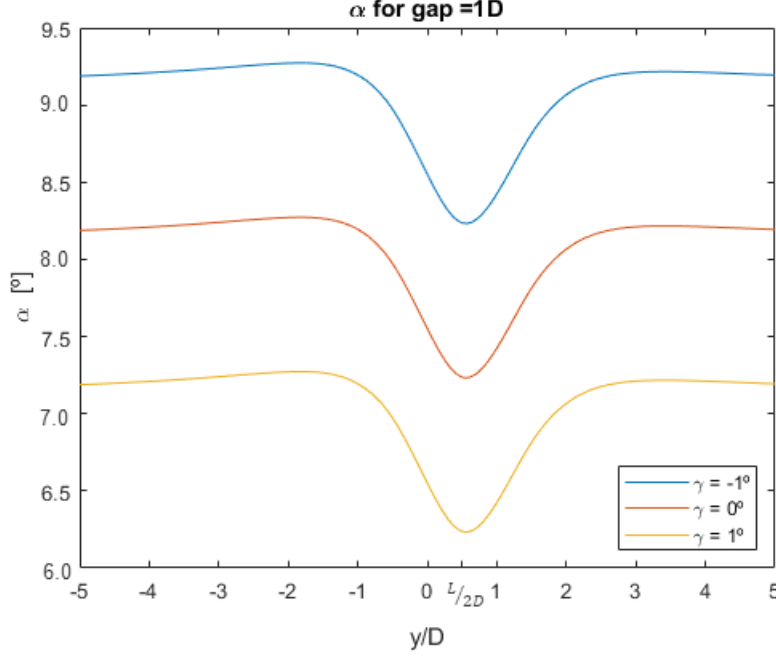


Figure 9.15: Values of α along y -axis for some twist angles.

Unlike Fig. 9.15, Fig. 9.16 and 9.17 bring more insight into the direct influence of a varying twist angle, namely, on the change it brings to the tangential and normal coefficients (there is an apparent trepidation on some of the curves, but this can be explained by deficiencies in MATLAB's interpolation polynomial and the small number of calculations).

Both figures (but perhaps even more noticeable in Fig. 9.17 due to the form of the curves) have clear parallels with Fig. 9.15, as in both cases a negative value of γ induces an increase on both coefficients and, conversely, a positive γ induces a decrease in both coefficients. This increase/decrease is, for both coefficients, of around $\pm 8,6\%$ and calculated as:

$$S = \frac{C_{t|n,\gamma \neq 0} - C_{t|n,\gamma = 0}}{C_{t|n,\gamma = 0}} \quad (9.4)$$

where, S represents the normalized increase/decrease;

$C_{t|n,\gamma \neq 0}$, is the tangential or normal coefficient value for a non-zero twist angle;

$C_{t|n,\gamma = 0}$, is the tangential or normal coefficient value for zero twist angle.

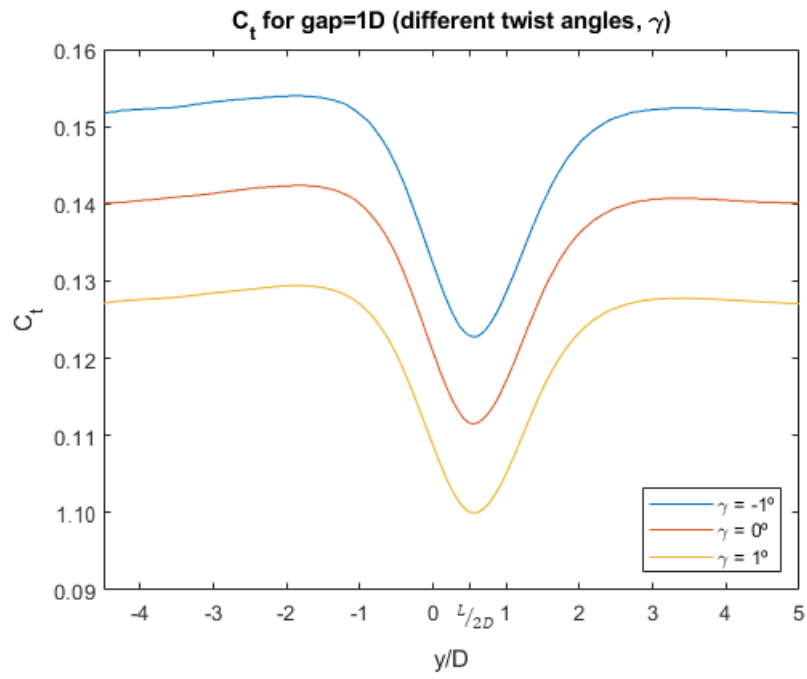


Figure 9.16: Value of C_t along y -axis for some twist angles.

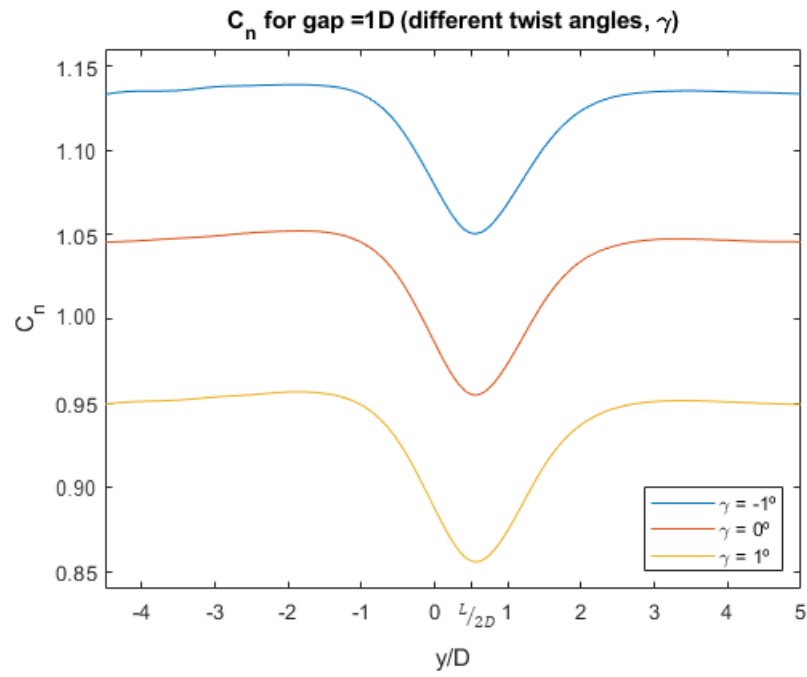


Figure 9.17: Value of C_n along y -axis for some twist angles.

9.5 Bak Model

The original formulation used the simple mathematical expressions derived from the potential flow theory for a circular cylinder immersed in the flow. As discussed, the potential flow solutions don't have an actual counterpart in the physical world (they are an idealized formulation), but were deemed sufficiently trustworthy to employ in an initial simplified approach, particularly as the region of interest is in front of the tower and there is a fair level of conformity [Gómez and Seume 2009a]. There are, naturally, different models which can be applied to more correctly emulate the behaviour of the flow around the tower (although most are worried with the wake region), as, for example, Parkinson and Jandali's blunt body wake conformal mapping model [Parkinson and Jandali 1970].

Nevertheless, a simpler model, known as Bak's model [Bak *et al.* 2001] has been employed due to, not only its simplicity, but also its wide application in the literature, as it is the case of AeroDyn [Moriarty and Hansen 2005], which implements the Bak model upwind and a widening-conscious wake formulation developed by Powles [Powles 1983] downwind.

This model can be described as the conjugation of three distinct parts: the base flow field is the solution of the potential flow around a cylinder, the wake is modelled as being dependent of the tower drag coefficient, C_d (which takes into account the tower's diameter), and finally, an additional tower dam model, as to model the upwind influence (the upwind wind velocity section is negatively influenced by the wake, which can be fundamentally understood as an extension of the original body, a second, contiguous, blunt body, bigger than the original due to the wake). It ultimately provides information about the influence of the tower on the local velocity field of near-tower points, which is especially noticeable on the increase of wind velocity at the tower sides.

Some modifications were performed to the original formulation (Eq. (8.4) and (8.5)), identified by the boxes in the equations, in order to have concordance between the mathematical expressions and the coordinate system, which leads us to the following normalized velocity components [Gómez and Seume 2009a]:

$$\frac{c_x}{c_0} = 1 - \frac{\left(\frac{-x}{R} - \boxed{0.1}\right)^2 - \frac{y^2}{R^2}}{\left(\left(\frac{-x}{R} - \boxed{0.1}\right)^2 + \frac{y^2}{R^2}\right)^2} + \boxed{\frac{C_d}{2\pi} \frac{\frac{-x}{R} - 0.1}{\left(\frac{-x}{R} - 0.1\right)^2 + \frac{y^2}{R^2}}} \quad (9.5)$$

$$\frac{c_y}{c_0} = -2 \frac{\left(\frac{-x}{R} - \boxed{0.1}\right) \frac{y}{R}}{\left(\left(\frac{-x}{R} - \boxed{0.1}\right)^2 + \frac{y^2}{R^2}\right)^2} + \boxed{\frac{C_d}{2\pi} \frac{\frac{y}{R}}{\left(\frac{-x}{R} - 0.1\right)^2 + \frac{y^2}{R^2}}} \quad (9.6)$$

Equations (9.5) and (9.6) relate the x - and y velocity components (duly normalized in relation to the undisturbed free-stream inflowing velocity, c_0) to the relative position from the tower, as expressed by x and y , the upwind and cross-wind distances normalized by the tower radius, R . C_d represents the drag coefficient of the tower, dependant on the Reynolds number of the tower, as dealt with in Chapter 4, and expressed as:

$$Re = \frac{c_0 D}{\nu} \quad (9.7)$$

where, D is the tower's diameter. Typically, for the Reynolds number of a wind turbine's working conditions, $C_d \approx 1$ [Schlichting and Gersten 2016] (for this application it is used $C_d = 1.1$).

We can then plot the velocity components for different gaps and compare them to the potential flow model, as seen in Fig. 9.18 and 9.19 (there is no $L/2D$ shifting in these graphs as the main objective of these is to compare the potential flow- and Bak's model, without yet taking into account the geometrical centre of the airfoil).

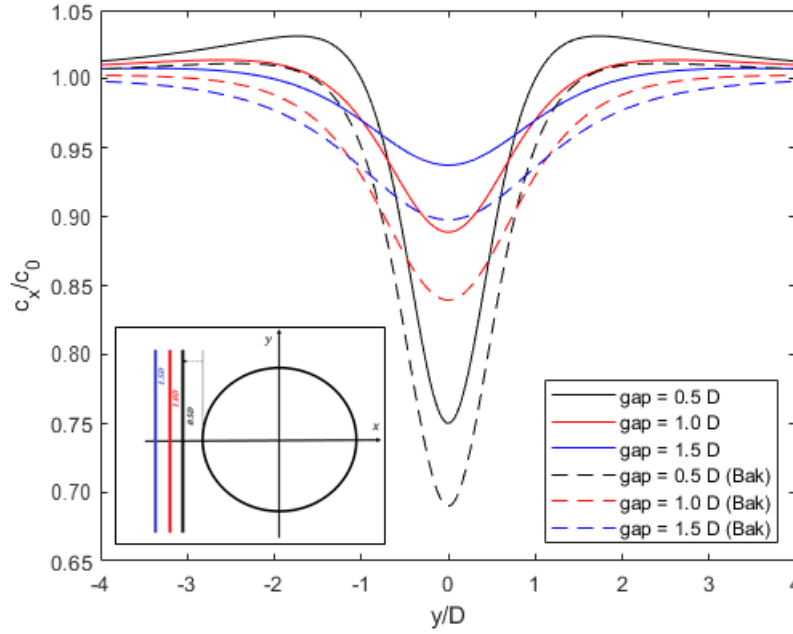


Figure 9.18: Value of c_x/c_0 along y -axis for several gaps for the potential theory formulation (full line), as well as for Bak's formulation (dashed line).

Figure 9.18 compares the normalized value of c_x along the relative position to the tower (y/D), from which two relevant differences in relation to the potential flow model become apparent: Bak's model consistently predicts for each gap a lower value for c_x than the potential flow model (which, for the minimal value, is around 5 %) and the slight increase before the plummet ($-4 \leq y/D \leq -1.5 \cup 1.5 \leq y/D \leq 4$) disappears for each different gap value.

This is due to the proximity to the tower: for the potential theory model, which doesn't take into account the tower wake effect, the slight increase in c_x/c_0 is explained by the closeness to the tower, which implies a stronger influence of the velocity increase on the sides of the tower (which isn't verified for higher gaps). This does not happen in Bak's model, as the velocity is noticeably smaller due to the adverse effect of the 'wake-enlarged' blunt body (for $\Delta x/D = 0.5$, no gap, this slight increase before the plummet is also verifiable using Bak's model; not represented in any figure).

Relatively to Fig. 9.19 there is a clear increase on the value of c_y for any gap (afar relatively from the tower, at $y/D = -4$ or $y/D = 4$, the value of c_y , instead of converging to 0, does so, but to -0.013 and 0.013 , respectively).

We can finally observe the final results attain with Bak's model for a gap of one tower

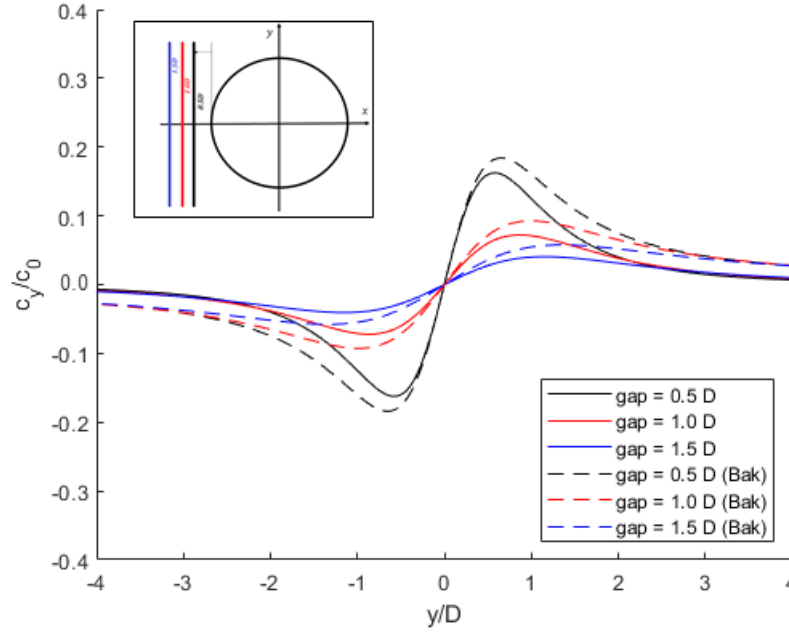


Figure 9.19: Value of c_y/c_0 along y -axis for several gaps for the potential theory formulation (full line), as well as Bak's formulation (dashed line).

diameter and compare to the original potential flow model: α (vd. Fig. 9.20), C_n (vd. Fig. 9.22), C_t (vd. Fig. 9.21).

These results are in line with the ones attained for the potential flow model ($L/2D$ rightwards shifting, left-side higher value), but with clear differences, particularly the lower values and the smoothing of near-tower value increase curves.

Fig. 9.20, 9.22 and 9.21 also seem to collectively show a faster convergence faraway from the tower between the potential flow model and Bak's model in the negative region of the y -axis. The convergence itself is expected, as both models ought to predict the same value for C_n , C_t and α afar from the tower since there its influence isn't noticeable, which allows us to identify the reason behind its speedier convergence on the left-field, apparently the $L/2D$ rightwards shifting, which, for every image exhibited, means that the curves to the left of the global minimum (at $y/D = L/2D$) are represented 10 % more than the right-side ones.

As Bak's model is believed to be more accurate, since it also considers the wake behind the tower (which, despite being downwind, nonetheless has an influence upstream), we can assume that the potential flow model is then prone to beget over-predictions of both the normal (≈ 4 %, $gap = 1D$) and tangential (≈ 1 %, $gap = 1D$) coefficients.

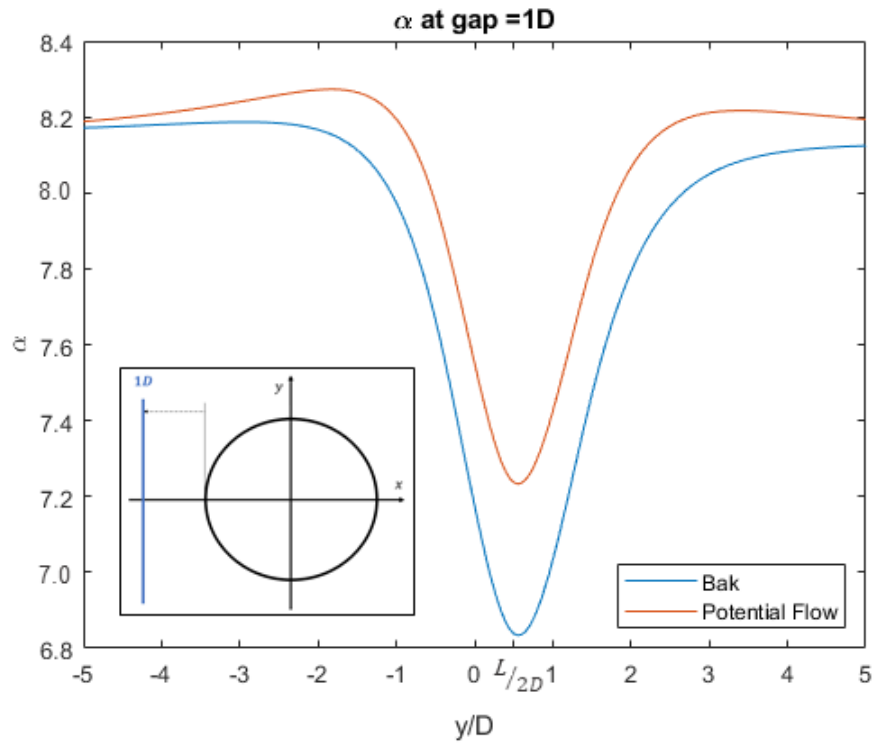


Figure 9.20: Value of α along y -axis for $gap = 1D$.

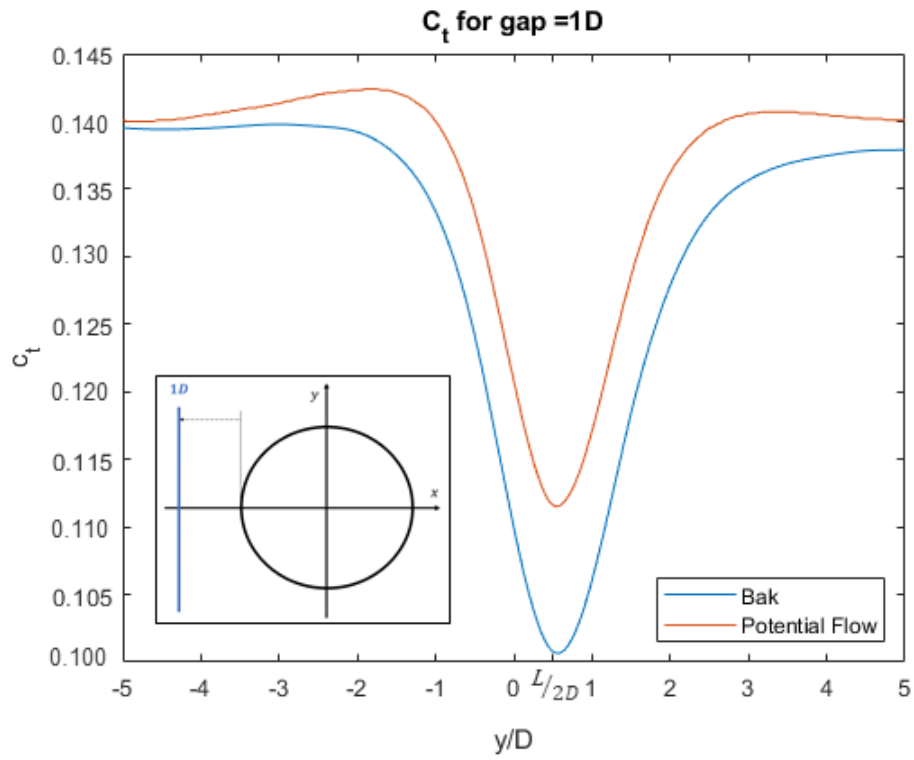


Figure 9.21: Value of C_t along y -axis vs α for $gap = 1D$.

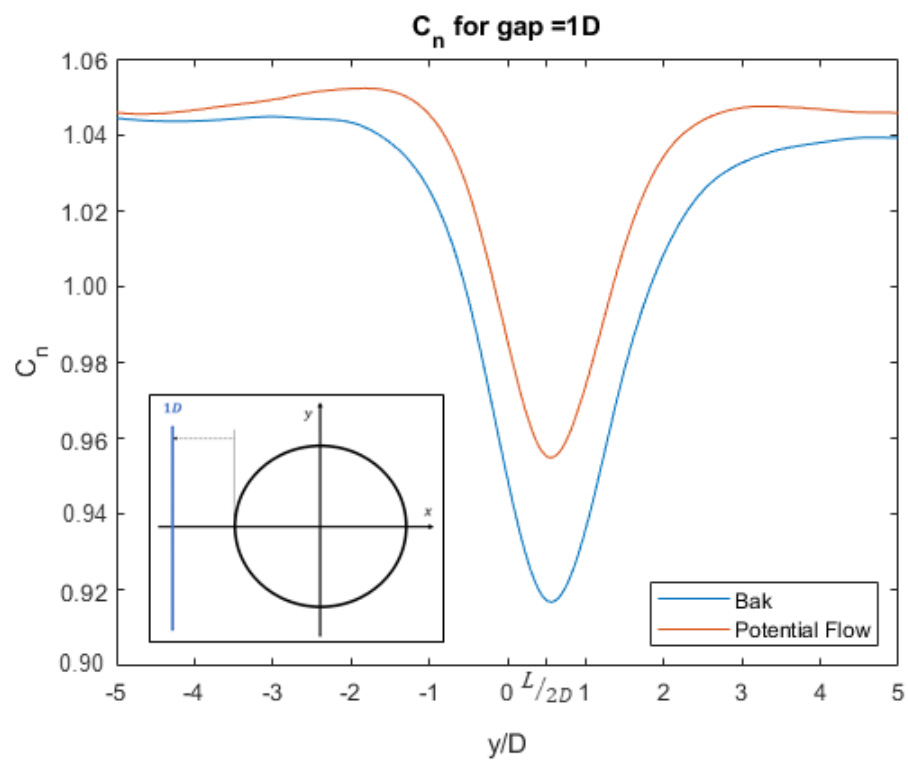


Figure 9.22: Value of C_n along y -axis vs α for $gap = 1D$.

Intentionally blank page.

Part IV

Discussion

Chapter 10

Discussion

The results attained in Chapter 9 ought to be properly addressed, as to their similitude with the comparable literature. To this end, two articles by A. Gómez and J. Seume [Gómez and Seume 2009a, Gómez and Seume 2009b] are essential to understand the plausibility of these results. These articles have been selected as benchmarks as, due to their methodology (passing the airfoil in front of the tower in a CFD simulation), the application of CFD in a tower interference model can be seen has a more accurate representation of the physical phenomena taking place, but also because these articles are based and obtain similar results to NREL's Phase VI program, which has experimental results for tower interference situations [Hand *et al.* 2001]. It must be noted that both articles perform computations for a S809 airfoil, as is the case for the outcomes of the present work.

As with most sources, both articles are sparse in so-called intermediary outputs, which can help us to more easily validate the model that is being implemented, but, nonetheless, some engaging figures can be extracted, namely, Fig. 10.1 and 10.2, which are evidently the counterparts of Fig. 9.18 and 9.19, respectively.

The juxtaposition of these four figures, apart from the axes scaling and the names of the gap levels selected, gives us an almost one-to-one comparison between Fig. 10.1 and Fig. 9.18, and Fig. 10.2 and 9.19. This allows us to assume that, both the potential flow model, as well as the tower interference model based on Bak's formulations, are calculating properly and that the near-tower velocity decrease faced by the blades has been properly computed. This allows us to affirm more convincingly that Bak's model is an improvement on the potential flow model, as the latter is likely to over-predict C_t and C_n .

As to the end-results (tangential and normal coefficients), one can start by comparing Fig. 9.7 and 9.8 with Fig. 10.3 and 10.4, where both coefficients were computed using QBLADE. Naturally, both sets of figures apply to the tangential and normal coefficients value (y -axis), but the variable in the x -axis is altered: the values of Fig. 9.7 and 9.8 are related to the relative distance to the centre of the tower, whereas those of Fig. 10.3 and 10.4 are coreferent to the position along the blade (spanwise). This requires us to return to Eq. (8.6), specifically, by relating $\lambda(r) = \omega r/c$, the tip speed ratio at any given radius, r , and $\lambda_R = \omega R/c$, the tip speed ratio for $r = R$, where R is the radius of the

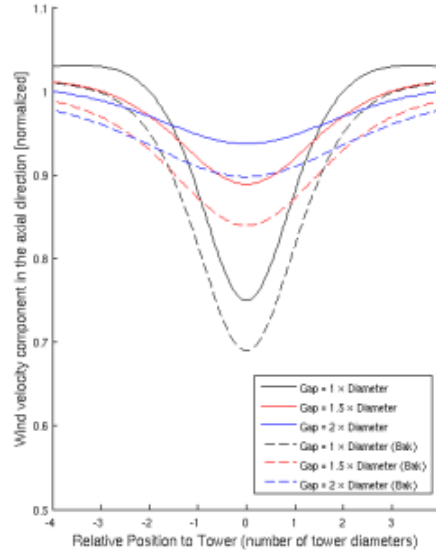


Figure 10.1: Axial velocity (c_x) calculated with the Bak-Model ($C_d = 1.1$) and with the potential flow model for 3 different gaps. Extracted from "Aerodynamic coupling of rotor and tower in HAWTs," by A. Gómez and J.R. Seume, 2009 [Gómez and Seume 2009a]

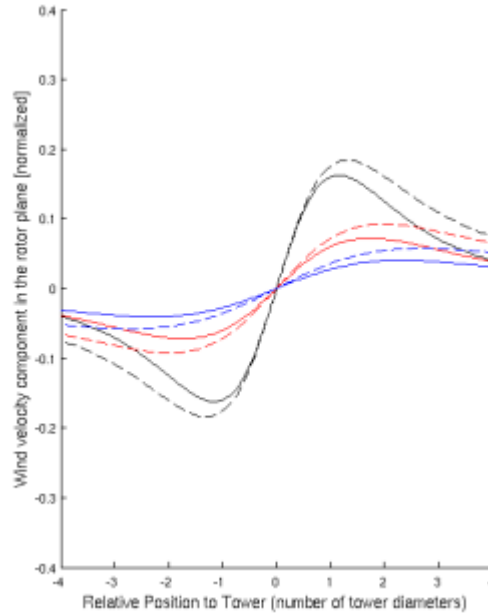


Figure 10.2: Tangential velocity (c_y) calculated with the Bak-Model ($C_d = 1.1$) and with the potential flow model for 3 different gaps. Extracted from "Aerodynamic coupling of rotor and tower in HAWTs," by A. Gómez and J.R. Seume, 2009 [Gómez and Seume 2009a]

wind turbine. As such, we have:

$$\frac{\lambda(r)}{\lambda_R} = \frac{r}{R} \quad (10.1)$$

Considering the initial assumptions that the value for the TSR was 7 ($\lambda(r) = 7$) and that the maximal expected value for the TSR would be around 9 ($\lambda_R = 9$), then Eq. (10.1) becomes:

$$\frac{\lambda(r)}{\lambda_R} = \frac{r}{R} = \frac{7}{9} \approx 0.778 \quad (10.2)$$

The value extracted from Eq. (10.2) is extremely valuable, as it indicates the position along the blade, r/R (identified in Fig. 10.3 and 10.4 as $pos[m]$), for which the calculations were performed. This means that, when reading these figures only the values of the curves at $pos \approx 0.78$ are to be considered (represented by the dashed circle).

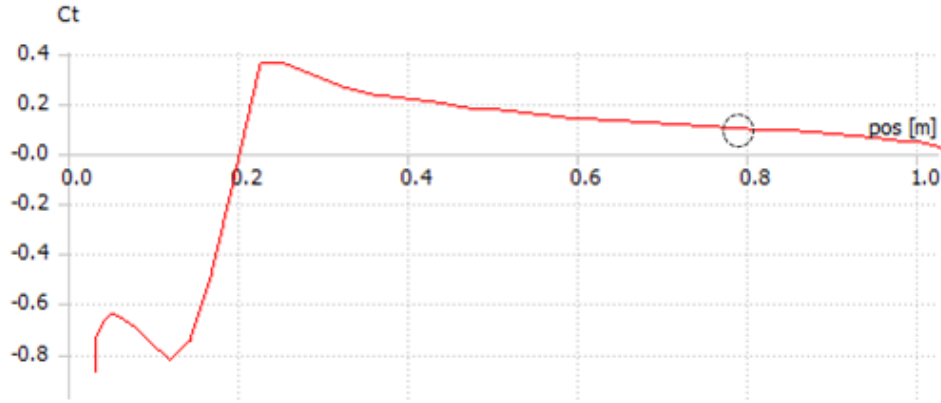


Figure 10.3: Steady tangential force coefficient, C_t , along blade spanwise position. Computed using QBLADE.

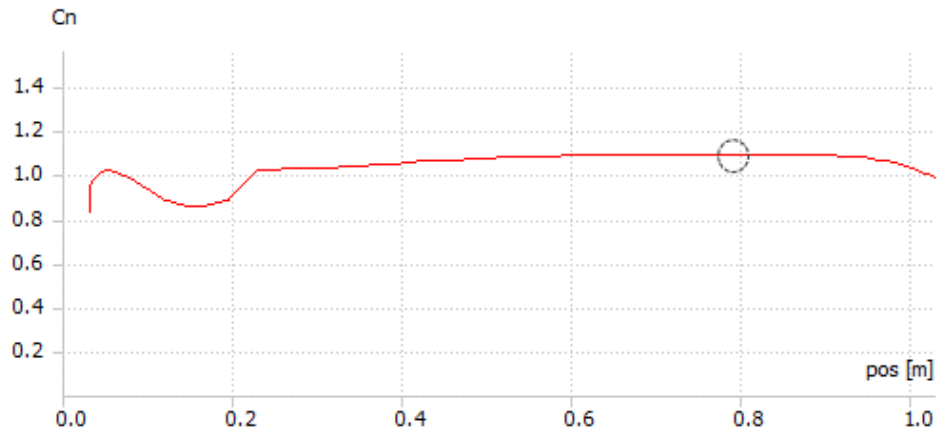


Figure 10.4: Steady axial force coefficient, C_n , along blade spanwise position. Computed using QBLADE.

The values are $C_t \approx 0.15$ and $C_n \approx 1.06$, which are almost identical to the values obtained by the MATLAB-XFOIL interface calculations, specifically, the tangential and normal coefficients values afar from the tower (which makes sense, as the QBLADE values are computed in a towerless scenario, and the y -afar values are mostly undisturbed by the influence of the tower).

The final possible comparison comes from Gómez and Seume [Gómez and Seume 2009b], who only provide a graphical illustration of the value attained for the normal coefficient, C_n , as depicted in Fig. 10.5, which contains the C_n curves for both the dynamic (red) and steady (black) cases. The dynamic axial force (normal) coefficient curve, which wasn't calculated, as it would escape one of the fundamental premises of this thesis, namely, a quasi-steady approach, was predicated upon the computation of the unsteady response when coupled with a Beddoes-Leishman dynamic stall model, previously mentioned in Section 1.4.

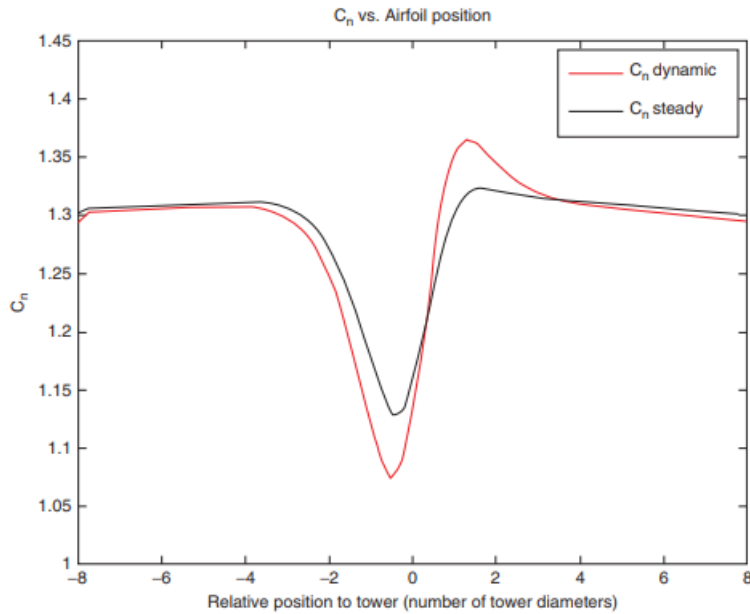


Figure 10.5: Steady normal force coefficient, C_n , for a varying angle of attack, for the steady inviscid TIM and a dynamic model. Extracted from "Load pulses on wind turbine structures caused by tower interference," by A. Gómez and J.R. Seume, 2009 [Gómez and Seume 2009b]

As dynamic calculations aren't the subject of this work, the normal force coefficient dynamic curve shall be ignored in this discussion.

Focusing on the black curve (steady), and comparing Fig. 10.5 with Fig. 9.8, we notice some differences, but, notwithstanding, an overall agreement on the shape of both curves: in both cases there is a clear vertical asymmetry, where one peak is noticeably higher than the other, a convergence to an undisturbed value, and what also appears to be, in this case, a slight left-ward shift of the curve. This asymmetry is highly relevant when one considers the loading the blades encounter, as maintenance and structural concerns might arise from this asymmetrical loading. When designing wind turbine blades, one must take into consideration the loading variation from its lowest point to

the highest peak, and not to the undisturbed values, as one might have assumed.

An essential point to be made when discussing the normal coefficient, and related to the loading variation above mentioned, is its influence on the wind turbine's structure: as stated in earlier chapters, one can not examine wind turbines as being unidirectionally influenced by aerodynamic factors; there is an important interdependent relation between structural- and fluid mechanics, which is described by the terms aeroelasticity or fluid-structure interactions. Whereas the tangential force is responsible for the motion of the rotor blades around the shaft, the normal force is responsible for blade-deflecting loading, which is transmitted to the shaft and to the tower itself, representing an added maintenance concern due to increased fatigue levels. The periodic drop (3 times per rotation period) on C_n gives rise to a mechanical loading which induces fatigue. It was also considered that, due to the magnitude of the frequencies and elements' mass at play, it would be unlikely to have the excitation frequency matching the eigenfrequency, thus downplaying the role of vibrations.

If we address the differences between both figures, we can perform a reverse-engineering analysis, and identify which assumptions were taken by Gómez and Seume [Gómez and Seume 2009b], namely, the apparent mirroring as to the vertical axis between both figures (peak on the left for Fig. 9.8, on the right for Fig. 10.5) leads us to believe that, either the referential axes are different, or the airfoil is translating incoming from another direction. Despite the small, reference-axes-related, dissimilarities, it can be stated that both curves are overwhelmingly agreeing, and stating the same fundamental result.

Finally, one of the most important outtakes must be discussed, specifically the different values the tangential and the normal coefficients present, which, as previously commented, due to the nature of the angle of attack (dependent on ϕ and, subsequently, on λ) see the tangential coefficient being approximately seven times smaller than the normal coefficient ($C_n \approx 7 \times C_t$).

This is extremely poignant, as one would assume that, with the tangential force being the main responsible for the rotation of the blades, the tangential force ought to be bigger than the normal force. This apparent contradiction is, as mentioned above, explained by the nature of the angle of attack, but shows very clearly the necessity of properly accommodating structures, not just accounting for the tangential force, but also, and perhaps even more so, for the normal force.

Another important consequence from the results attained in Chapter 9 is that, naturally, the farther away from the tower the rotor-plane is, the weaker the upstream tower influence will be, which yields an immediate practical conclusion: to hinder the nefarious consequences of this influence the rotor plane must be as far-away from the tower as possible (this is not always feasible, as wind turbines must take into account a myriad of other issues, namely structural- and assembly-related ones).

Finally, the results hereby presented fully reflect some of the initial assertions of Section 1.3, namely:

- Drop in power output – Although the tower influence effect on the power wasn't quantified in this work, it is obvious that the drop on the tangential force coefficient is connected with a drop on the useful torque, which is naturally connected to a drop on the power output by multiplying the torque by the angular speed, ω . This has been extensively researched [Dolan and Lehn 2006, Fadaeinedjad *et al.* 2009, Mur-Amada and Bayod-Rújula 2007, Sintra *et al.* 2014], where a periodic (3 times per

cycle, each 120°) drop on the power output is to be expected due to the upstream influence of the tower.

- Blade loads – The periodicity (which arises from the 120° -periodicity where loading is changed), inherent to the loading blades encounter when taking into account the upstream influence of the tower, has a particularly adverse effect on these structures. This has a direct implication on the increased fatigue levels faced by wind turbines [Pedersen *et al.* 2012], from which design and maintenance concerns emerge [Leishman 2002].

One can, then, affirm the overall consistency between the end-results of this work and the consulted literature, and whose numerous undesirable practical implications moreover support the need to take into account this effect not only in specialized analysis, but also in the designing stages of wind turbines, which would benefit from the employment of simplified methods due to their speed and results quality.

Part V

Conclusions

Chapter 11

Conclusions and Further Research Directions

In the scope of this work the upstream influence of the tower on the flow on the blade section was studied by employing simplified methods. These consisted of a potential flow formulation that replicates the characteristics of the flow around a circular cylinder (some of the debilities inherent to this model were subsequently amended by the implementation of Bak's model). A panel-method-based software, XFOIL, whose integration in a interface with the numerical computing program MATLAB enabled the calculation of the aerodynamic characteristics of a chosen subsonic airfoil, in the form of lift and drag coefficients.

The applicability of the simplified methods was investigated through an extensive literature research and a comparative study in which more complete alternatives were also equated. The advantages and disadvantages, as well as the employment adequacy, of every method were comprehensively summed up, wherein the selection of a panel-based method was taken due to: overall method speed, satisfactory results (when compared to experimental ones), generalized scope of the study (a more specific investigation would require more complex methods, such as CFD) and availability of the software.

Having successfully attained the lift and drag coefficients for some representative scenarios, namely the inclusion of a twist angle and Bak's model, the tangential and normal coefficients were calculated and validated with the help of QBLADE and secondary literature results. The values of these final coefficients and their respective patterns were then critically analyzed in relation to the adverse physical phenomena wind turbines face and the implications they have on their functioning and power output. It was proven that the potential flow model over-predicts these coefficients, when compared to Bak's formulation.

The results obtained were also related to their practical ramifications in wind turbines, namely prescribing a greater distance between the rotor-plane and the tower, but also, by providing a quantitative value for the decrease the tangential and normal coefficients suffer for each gap. Thus, it is provided an immediate sense of the significance the tower interference has on power (tangential coefficient) and axial loading (normal coefficient) and its implications on blade design (namely due to the asymmetrical nature of the loading, one must take into account the peak- and lowest values).

It can be thus concluded that, through the use of simplified methods, all of the ini-

tial objectives were attained and the influence of the tower was studied as far as this methodology allowed. Hence, this work presents a strong basis from which many further inquiries can be performed, outlining several future research directions, tendentially departing from the simplified methodology into evermore complex methods, specifically:

- Unsteadiness – One of the initial assumptions was that we could reduce our system to a quasi-steady response [Zahle *et al.* 2009]. Nonetheless, an unsteady model would encompass more information as related to the flow, allowing for a more complete model. One such possibility would be the study of a dynamic stall model (*vd.* Section 1.4), as the Leishman-Beddoes model. Nevertheless, as studied by Gómez and Seume [Gómez and Seume 2009a, Gómez and Seume 2009b], the implementation of said model might be prone to overshooting some estimations. Regardless, other possible research directions, when considering unsteadiness and an increase in the model's complexity, would almost invariably have to include CFD tools in their methodology;
- Influence of the blades on the tower – The present study was one-sided as to the tower-blades dichotomy, since only the influence of the tower on the flow on the blades was investigated. It would be interesting to research, not just from an aerodynamic, but also from a structural point-of-view, the inverse influence;
- Geometric changes – As mentioned in the introduction to Chapter 2, the aerodynamic study is insufficient, as one must account for the geometric changes and loads wind turbine components suffer and their converse influence on external loads (aerodynamic), summed up by the term aeroelasticity. Such a study would require a Fluid-Structure Interaction software (as, for example, ANSYS);
- Power calculation – It would also be of interest to calculate the power output drop for the entirety of the wind turbine, which would require the employment of BEM, and that would account for the tower influence and its further comparison to a tower-free model (as obtained through the use of QBLADE).
- Change of the rotor-plane – One final future research direction would be to investigate what would be the maximal distance between the rotor-plane and the tower, taking into account structural and assembly considerations.

Bibliography

- [Abbott *et al.* 1945] I. H. Abbott, A. E. Von Doenhoff and L. Stivers Jr. *Summary of Airfoil Data*. Technical Report NACA-TR-824, National Advisory Committee for Aeronautics, Langley Aeronautical Lab, Langley Field, VA, United States, 1945.
- [Aerodynamics for Students 2019] Aerodynamics for Students. 2D Panel Methods. <http://www.aerodynamics4students.com/subsonic-aerofoil-and-wing-theory/2d-panel-methods.php>, 2019. Accessed: 11-03-2019.
- [Aichinger 2012] Georg Aichinger. *Einfluss der Änderung der Rotorblattgeometrie auf Windkraftanlagen*. Master’s thesis, Technische Universität Wien, Vienna, Austria, 2012.
- [Airfoil Tools 2019] Airfoil Tools. Airfoil Tools E387. <http://airfoiltools.com/airfoil/details?airfoil=e387-il>, 2019. Accessed: 05-03-2019.
- [Aitken 1942] A. C. Aitken. *Statistical Mathematics*. Oliver And Boyd; London, 1942.
- [Anderson Jr. 1999a] J. D. Anderson Jr. *A History of Aerodynamics and its Impact on Flying Machines*, Vol. 8 de *Cambridge Aerospace Series*. Cambridge University Press, 1999.
- [Anderson Jr. 1999b] J. D. Anderson Jr. *Aircraft Performance and Design*. McGraw-Hill Science/Engineering/Math, 1999.
- [Aris 1989] R. Aris. *Vectors, Tensors, and the Basic Equations of Fluid Mechanics*. Dover Publications, 1989.
- [AWEA 2011] US AWEA. *Wind Industry Annual Market Report Year Ending 2010*. Technical report, American Wind Energy Association, Washington, DC, USA, 2011.
- [Baines *et al.* 1996] P. G. Baines, S. J. Majumdar and H. Mitsudera. The mechanics of the Tollmien-Schlichting wave. *Journal of Fluid Mechanics*, 312:107–124, 1996.
- [Bak *et al.* 2001] C. Bak, H. A. Madsen and J. Johansen. Influence from blade-tower interaction on fatigue loads and dynamics (poster). In *2001 European Wind Energy Conference and Exhibition (EWEC’01)*. WIP Renewable Energies, 2001.
- [Barthlott and Fiedler 2003] C. Barthlott and F. Fiedler. Turbulence structure in the wake region of a meteorological tower. *Boundary-Layer Meteorology*, 108(1):175–190, 2003.

- [Bazilevs *et al.* 2013] Y. Bazilevs, K. Takizawa and T. Tezduyar. *Computational Fluid-Structure Interaction: Methods and Applications*. Wiley-Blackwell, 2013.
- [Bernoulli 1738] D. Bernoulli. *Hydrodynamica, sive de viribus et motibus fluidorum commentarii*. Typis Joh. Reihn. Deckeri, 1738.
- [Bertagnolio *et al.* 2001] F. Bertagnolio, N. N. Sørensen, J. Johansen and P. Fuglsang. Wind turbine airfoil catalogue. *Forskningscenter Risø*, Risø-R, No. 1280(EN), 2001.
- [Best and Burke 2018] R. Best and P. J. Burke. Adoption of solar and wind energy: The roles of carbon pricing and aggregate policy support. *Energy Policy*, 118:404–417, 2018.
- [Betz 1920] A. Betz. Das maximum der theoretisch möglichen ausnutzung deswindes durch windmotoren. *Zeitschrift für das gesamte Turbinenwesen*, 20, 1920.
- [Betz 1926] A. Betz. *Wind-Energie und ihre Ausnutzung durch Windmühlen*. Vandenhoeck, 1926.
- [Blasius 1908] P. R. H. Blasius. Grenzsichten in flüssigkeiten mit kleiner reibung. *Zeitschrift für angewandte Mathematik und Physik*, 56:1–37, 1908.
- [Branlard and Gaunaa 2015] E. S. P. Branlard and M. Gaunaa. *Analysis of Wind Turbine Aerodynamics and Aeroelasticity using Vortex-Based Methods*. DTU Wind Energy, 2015.
- [Brederode 2014] V. Brederode. *Aerodinâmica Incompressível: Fundamentos*. Lisboa: IST Press, 2014.
- [Buckingham 1914] E. Buckingham. On physically similar systems; illustrations of the use of dimensional equations. *Physical Review*, 4:345–376, October 1914.
- [Burton *et al.* 2011] T. Burton, N. Jenkins, D. Sharpe and E. Bossanyi. *Wind Energy Handbook*. John Wiley & Sons, 2011.
- [Butterfield *et al.* 1991] C. P. Butterfield, D. Simms, G. Scott and A. C. Hansen. *Dynamic Stall on Wind Turbine Blades*. Technical report, National Renewable Energy Lab., Golden, CO (United States), 1991.
- [Cermak and Horn 1968] J. E. Cermak and J. D. Horn. Tower shadow effect. *Journal of Geophysical Research*, 73(6):1869–1876, 1968.
- [Cervantes 2017] M. Cervantes. *Dom Quixote de La Mancha*. Edições Dom Quixote, 2017.
- [Ceyhan 2012] O. Ceyhan. Towards 20MW wind turbine: High Reynolds number effects on rotor design. In *50th AIAA Aerospace Sciences Meeting including the New Horizons Forum and Aerospace Exposition*, p. 1157, 2012.
- [Chattot 2006] J.-J. Chattot. Extension of a helicoidal vortex model to account for blade flexibility and tower interference. *Journal of Solar Energy Engineering*, 128(4):455–460, 2006.

- [Chattot 2008] J.-J. Chattot. Tower shadow modelization with helicoidal vortex method. *Computers & Fluids*, 37(5):499–504, 2008.
- [Chattot and Hafez 2015] J.-J. Chattot and M. Hafez. *Theoretical and Applied Aerodynamics and Related Numerical Methods*. Springer-Verlag, 2015.
- [Chaviaropoulos and Hansen 2000] P. K. Chaviaropoulos and M. O. L. Hansen. Investigating three-dimensional and rotational effects on wind turbine blades by means of a quasi-3D Navier-Stokes solver. *Journal of Fluids Engineering*, 122(2):330–336, 2000.
- [Cline 2011] S. Cline. *Potential Flow Modelling for Wind Turbines*. Master’s thesis, University of Victoria, Department of Mechanical Engineering, 2011.
- [Cline and Crawford 2010] S. Cline and C. Crawford. Comparison of potential flow wake models for horizontal-axis wind turbine rotors. In *48th AIAA Aerospace Sciences Meeting Including the New Horizons Forum and Aerospace Exposition*, p. 463, 2010.
- [Coder and Maughmer 2014] J. G. Coder and M. D. Maughmer. Comparisons of theoretical methods for predicting airfoil aerodynamic characteristics. *Journal of Aircraft*, 51(1):183–191, 2014.
- [Crowdy 2006] D. G. Crowdy. Analytical solutions for uniform potential flow past multiple cylinders. *European Journal of Mechanics-B/Fluids*, 25(4):459–470, 2006.
- [Dabberdt 1968] W. F. Dabberdt. Tower-induced errors in wind profile measurements. *Journal of Applied Meteorology*, 7(3):359–366, 1968.
- [d’Alembert 1752] J. Le R. d’Alembert. *Essai d’une Nouvelle Théorie de la Résistance des Fluides*. David l’aîné, 1752.
- [Darrieus 1931] G. J. M. Darrieus. Turbine having its rotating shaft transverse to the flow of the current, December 8 1931. US Patent 1,835,018.
- [De Vries 1979] O. De Vries. *Fluid Dynamic Aspects of Wind Energy Conversion*. Technical report, Advisory Group for Aerospace Research and Development, Neuilly-sur-Seine, France, 1979.
- [DeBenedictis 2017] E. P. DeBenedictis. It’s time to redefine moore’s law again. *Computer*, 50(2):72–75, 2017.
- [Dirichlet 1889] P. G. L. Dirichlet. *Werke*. Reimer, Ed. by L. Kronecker and L. Fuchs, Berlin, 1889.
- [Dolan and Lehn 2006] D. S. L. Dolan and P. W. Lehn. Simulation model of wind turbine 3p torque oscillations due to wind shear and tower shadow. In *Power Systems Conference and Exposition, 2006. PSCE’06. 2006 IEEE PES*, pp. 2050–2057. IEEE, 2006.
- [Dorian et al. 2006] J. P. Dorian, H. T. Franssen and D. R. Simbeck. Global challenges in energy. *Energy Policy*, 34(15):1984–1991, 2006.

- [Drela 1989] M. Drela. XFOIL: An analysis and design system for low Reynolds number airfoils. In *Low Reynolds number aerodynamics*, pp. 1–12. Springer, 1989.
- [Drela 1998] M. Drela. Assorted views on teaching of aerodynamics. In *16th AIAA Applied Aerodynamics Conference*, p. 2792, 1998.
- [Drela and Giles 1987] M. Drela and M. Giles. ISES-A two-dimensional viscous aerodynamic design and analysis code. In *25th AIAA Aerospace Sciences Meeting*, p. 424, 1987.
- [Eppler 1990] R. Eppler. *Airfoil Design and Data*. Springer Verlag, Berlin, 1990.
- [Eriksen and Krogstad 2017] P. E. Eriksen and P.-Å. Krogstad. Development of coherent motion in the wake of a model wind turbine. *Renewable Energy*, 108:449–460, 2017.
- [Everitt and Skrondal 2010] B. S. Everitt and A. Skrondal. *The Cambridge Dictionary of Statistics*. Cambridge University Press, Cambridge, UK, 4th edition, 2010.
- [Fadaeinedjad *et al.* 2009] R. Fadaeinedjad, G. Moschopoulos and M. Moallem. The impact of tower shadow, yaw error, and wind shears on power quality in a wind–diesel system. *IEEE Transactions on Energy Conversion*, 24(1):102–111, 2009.
- [Ferreira 2009] C. S. Ferreira. The Near Wake of the VAWT. Delft University of Technology, Stevinweg 1, 2628 CN Delft, Netherlands, 2009.
- [Froude 1889] R. E. Froude. On the part played in propulsion by differences of fluid pressure. *Trans. Inst. Naval Architects*, 30:390, 1889.
- [Garzon *et al.* 2010] B. B. Garzon, L. C. Henriksen, A. D. Hansen, N. A.o Cutululis and P. E. Sørensen. Coupling of HAWC2 and Matlab: Towards an integrated simulation platform. In *2010 European Wind Energy Conference and Exhibition*. European Wind Energy Association (EWEA), 2010.
- [Ge *et al.* 2014] M. Ge, D. Tian and Y. Deng. Reynolds number effect on the optimization of a wind turbine blade for maximum aerodynamic efficiency. *Journal of Energy Engineering*, 142(1):04014056, 2014.
- [Glauert 1935] H. Glauert. Airplane propellers. In *Aerodynamic Theory*, pp. 169–360. Springer, 1935.
- [Gomes *et al.* 2018] A. O. Gomes, R. F. Brito, H. M. P. Rosa, J. C. C. Campos, A. M. B. Tibiriça and P. C. Treto. Experimental analysis of an S809 airfoil. *Re-term-Thermal Engineering*, 13(2):28–32, 2018.
- [Gómez and Seume 2009a] A. Gómez and J. R. Seume. Aerodynamic coupling of rotor and tower in hawts. *Proceedings of the EWEC. Marseille, France*, 2009.
- [Gómez and Seume 2009b] A. Gómez and J. R. Seume. Load pulses on wind turbine structures caused by tower interference. *Wind Engineering*, 33(6):555–570, 2009.
- [Green 1828] G. Green. *An Essay on the Application of Mathematical Analysis to the Theories of Electricity and Magnetism*. T. Wheelhouse, Nottingham, England, 1828.

- [Hager and Castro-Orgaz 2016] W. H. Hager and O. Castro-Orgaz. William Froude and the Froude number. *Journal of Hydraulic Engineering*, 143(4):02516005, 2016.
- [Hand *et al.* 2001] M. M. Hand, D. A. Simms, L. J. Fingersh, D. W. Jager, J. R. Cottrell, S. Schreck and S. M. Larwood. *Unsteady Aerodynamics Experiment Phase VI: Wind Tunnel Test Configurations and Available Data Campaigns*. Technical report, National Renewable Energy Lab., Golden, Colorado, US, 2001.
- [Hansen 2015] M. O. L. Hansen. *Aerodynamics of Wind Turbines*. Routledge, 2015.
- [Hansen *et al.* 2004] M. H. Hansen, M. Gaunaa and H. A. Madsen. A Beddoes-Leishman type dynamic stall model in state-space and indicial formulations. *Forskningscenter Risø, Risø-R*, No 1354, 2004.
- [Hansen *et al.* 2006] M. O. L. Hansen, J. N. Sørensen, S. Voutsinas, N. Sørensen and H. A. Madsen. State of the art in wind turbine aerodynamics and aeroelasticity. *Progress in Aerospace Sciences*, 42(4):285–330, 2006.
- [Harlow 2004] F. H. Harlow. Fluid dynamics in group T-3 Los Alamos National Laboratory:(LA-UR-03-3852). *Journal of Computational Physics*, 195(2):414–433, 2004.
- [Hau 2013] E. Hau. *Wind Turbines: Fundamentals, Technologies, Application, Economics*. Springer Science & Business Media, 2013.
- [Heath 1956] T. L. Heath. The thirteen books of Euclid’s Elements. Courier Corporation, 1956.
- [Heinzelmann 2011] B. S. Heinzelmann. *Strömungsbeeinflussung bei Rotorblättern von Windenergieanlagen mit Schwerpunkt auf Grenzschichtabsaugung*. Technische Universität Berlin, 2011.
- [Hele-Shaw 1898] H. S. Hele-Shaw. *The Flow of Water*. Nature Publishing Group, 1898.
- [Hersey 1966] M. D. Hersey. *Theory and Research in Lubrication: Foundation for Future Developments*. John Wiley & Sons, 1966.
- [Hills 1996] R. L. Hills. *Power From Wind: a History of Windmill Technology*. Cambridge University Press, 1996.
- [Houcque 2005] D. Houcque. *Introduction to Matlab for Engineering Students*. Northwestern University, 2005.
- [Jonkman *et al.* 2015] J. M. Jonkman, G. J. Hayman, B. J. Jonkman, R. R. Damiani and R. E. Murray. *AeroDyn v15 User’s Guide and Theory Manual*. NREL, Golden, Colorado, USA, 2015.
- [Joseph 2003] D. D. Joseph. Viscous potential flow. *Journal of Fluid Mechanics*, 479:191–197, 2003.
- [Kahng 2010] A. B. Kahng. Scaling: more than Moore’s law. *IEEE Design & Test of Computers*, 27(3):86–87, 2010.

-
- [Kerwin 2001] J. E. Kerwin. 13.04. Lecture Notes on Hydrofoils and Propellers. [Online]. Available from: <https://ocw.mit.edu/>, January 2001. License: Creative Commons BY-NC-SA.
- [Kusiak and Song 2010] A. Kusiak and Z. Song. Design of wind farm layout for maximum wind energy capture. *Renewable energy*, 35(3):685–694, 2010.
- [Kutta 1910] W. M. Kutta. Über eine mit den grundlagen des flug problems in beziehung stehende zweidimensionale strömung. *KB Akad. der wissenschaften in kommission des G. Franz'schen Verlags (J. Roth)*, 1910.
- [Lackner *et al.* 2013] M. Lackner, N. Devellder and T. Sebastian. On 2D and 3D potential flow models of upwind wind turbine tower interference. *Computers & Fluids*, 71:375–379, 2013.
- [Lanchester 1908] F. W. Lanchester. *Aerodynamics: Constituting the First Volume of a Complete Work on Aerial Flight*, Vol. 1. D. Van Nostrand, 1908.
- [Langford 1989] J. Langford. The Daedalus project-A summary of lessons learned. In *Aircraft Design and Operations Meeting*, p. 2048, 1989.
- [Larsen and Hansen 2007] T. J. Larsen and A. M. Hansen. How 2 HAWC2, the user's manual. *Forskningscenter Risø, Risø-R*, No. 1597(ver. 3-1)(EN), 2007.
- [Launder and Spalding 1983] B. E. Launder and D. B. Spalding. The numerical computation of turbulent flows. In *Numerical prediction of flow, heat transfer, turbulence and combustion*, pp. 96–116. Elsevier, 1983.
- [Leishman 2002] J. G. Leishman. Challenges in modelling the unsteady aerodynamics of wind turbines. *Wind Energy: An International Journal for Progress and Applications in Wind Power Conversion Technology*, 5(2-3):85–132, 2002.
- [Leishman and Beddoes 1989] J. G. Leishman and T. S. Beddoes. A semi-empirical model for dynamic stall. *Journal of the American Helicopter society*, 34(3):3–17, 1989.
- [Lin and Shieh 2010] S.-Y. Lin and T.-H. Shieh. Study of aerodynamical interference for a wind turbine. *International Communications in Heat and Mass Transfer*, 37(8):1044–1047, 2010.
- [Liu *et al.* 2013] X. Liu, L. Wang and X. Tang. Optimized linearization of chord and twist angle profiles for fixed-pitch fixed-speed wind turbine blades. *Renewable Energy*, 57:111–119, 2013.
- [Lopion *et al.* 2018] P. Lopion, P. Markewitz, M. Robinius and D. Stolten. A review of current challenges and trends in energy systems modeling. *Renewable and Sustainable Energy Reviews*, 96:156–166, 2018.
- [Lubitz and Michalak 2018] W. D. Lubitz and A. Michalak. Experimental and theoretical investigation of tower shadow impacts on anemometer measurements. *Journal of Wind Engineering and Industrial Aerodynamics*, 176:112–119, 2018.
-

- [Magnus 1853] G. Magnus. Über die abweichung der geschosse, und über eine auffallende erscheinung bei rotirenden körpern. *Annalen der physik*, 164(1):1–29, 1853.
- [Manwell *et al.* 2010] J. F. Manwell, J. G. McGowan and A. L. Rogers. *Wind Energy Explained: Theory, Design and Application*. John Wiley & Sons, 2010.
- [Marten 2016] D. Marten. *QBlade v0.95 Guidelines for Lifting Line Free Vortex Wake Simulations*. Technical University of Berlin, 2016.
- [Marten and Wendler 2013] D. Marten and J. Wendler. *Qblade Guidelines, Ver. 0.6*. Technical University of Berlin, Berlin, Germany, 2013.
- [Marten *et al.* 2013] D. Marten, J. Wendler, G. Pechlivanoglou, C. N. Nayeri and C. O. Paschereit. QBLADE: an open source tool for design and simulation of horizontal and vertical axis wind turbines. *Int. J. Emerging Technol. Adv. Eng*, 3(3):264–269, 2013.
- [Marzocca *et al.* 2001] P. Marzocca, L. Librescu and G. Chiocchia. Aeroelastic response of 2-D lifting surfaces to gust and arbitrary explosive loading signatures. *International Journal of Impact Engineering*, 25(1):41–65, 2001.
- [Mauclère 2009] X. Mauclère. *Automatic 2D Airfoil Generation, Evaluation and Optimisation Using MATLAB and XFOIL*. Master’s thesis, Danish Technical University, Department of Mechanical Engineering, 2009.
- [McGhee *et al.* 1988] R. J. McGhee, B. S. Walker and B. F. Millard. *Experimental Results for the Eppler 387 Airfoil at Low Reynolds Numbers in the Langley Low-Turbulence Pressure Tunnel*. Technical report, NASA Langley Research Center, Hampton, VA, United States, 1988.
- [McTavish *et al.* 2013] S. McTavish, D. Feszty and F. Nitzsche. Evaluating Reynolds number effects in small-scale wind turbine experiments. *Journal of Wind Engineering and Industrial Aerodynamics*, 120:81–90, 2013.
- [Menter 1993] F. R. Menter. Zonal two equation k- ω turbulence models for aerodynamic flows. In *23rd Fluid Dynamics, Plasmadynamics, and Lasers Conference*, p. 2906, 1993.
- [Moler 2004] C. B. Moler. *Numerical Computing with MATLAB*. SIAM, 2004.
- [Montgomerie 2004] B. Montgomerie. *Methods for Root Effects, Tip Effects and Extending the Angle of Attack Range to ± 180 deg, With Application to Aerodynamics for Blades on Wind Turbines and Propellers*. Technical report, FOI, Swedish Defence Research Agency, Stockholm, Sweden, 2004.
- [Moore 1965] G. E. Moore. Cramming more components onto integrated circuits. *Electronics*, 38(8):144–end, 1965.
- [Morgado *et al.* 2016] J. Morgado, R. Vizinho, M. A. R. Silvestre and J. C. Páscoa. XFOIL vs CFD performance predictions for high lift low Reynolds number airfoils. *Aerospace Science and Technology*, 52:207–214, 2016.

- [Moriarty and Hansen 2005] P. J. Moriarty and A. C. Hansen. *AeroDyn Theory Manual*. National Renewable Energy Lab, Golden, Colorado, USA, 2005.
- [Munduate *et al.* 2004] X. Munduate, F. N. Coton and R. A. M. Galbraith. An investigation of the aerodynamic response of a wind turbine blade to tower shadow. *Journal of Solar Energy Engineering*, 126(4):1034–1040, 2004.
- [Mur-Amada and Bayod-Rújula 2007] J. Mur-Amada and Á. A. Bayod-Rújula. Pace of tower shadow fluctuations in a wind farm. *Pulse*, 2(2):2, 2007.
- [Newton 1687] I. Newton. *Philosophiæ Naturalis Principia Mathematica*. London, 1687.
- [Nissen 2011] P.-O. Nissen, editor. The story of the reduction in the number of windmill sails. *The International Molinological Symposium*, 2011.
- [Noyes *et al.* 2018] C. Noyes, C. Qin, E. Loth and S. Schreck. Measurements and predictions of wind turbine tower shadow and fairing effects. *Journal of Wind Engineering and Industrial Aerodynamics*, 179:297–307, 2018.
- [NREL 2012] NREL. *OSU Wind-Tunnel Test Data*. https://wind.nrel.gov/airfoils/OSU_data/data/, 2012. Accessed: 04-03-2019.
- [Oerlemans *et al.* 2007] S. Oerlemans, P. Sijtsma and B. M. López. Location and quantification of noise sources on a wind turbine. *Journal of Sound and Vibration*, 299(4-5):869–883, 2007.
- [Parkinson and Jandali 1970] G. V. Parkinson and T. Jandali. A wake source model for bluff body potential flow. *Journal of Fluid Mechanics*, 40(3):577–594, 1970.
- [Pedersen *et al.* 2012] R. R. Pedersen, S. R. K. Nielsen and P. Thoft-Christensen. Stochastic analysis of the influence of tower shadow on fatigue life of wind turbine blade. *Structural Safety*, 35:63–71, 2012.
- [Pena *et al.* 2017] I. Pena, I. L. Azevedo and L. A. F. M. Ferreira. Lessons from wind policy in Portugal. *Energy Policy*, 103:193–202, 2017.
- [Pereira *et al.* 2013] R. Pereira, G. Schepers and M. D. Pavel. Validation of the Beddoes–Leishman dynamic stall model for horizontal axis wind turbines using MEXICO data. *Wind Energy*, 16(2):207–219, 2013.
- [Petot 1989] D. Petot. Differential equation modeling of dynamic stall. *La Recherche Aérospatiale (English Edition)*, 5:59–72, 1989.
- [Pires *et al.* 2016] O. Pires, X. Munduate, O. Ceyhan, M. Jacobs and H. Snel. Analysis of high Reynolds numbers effects on a wind turbine airfoil using 2D wind tunnel test data. In *Journal of Physics: Conference Series*, Vol. 753, p. 022047. IOP Publishing, 2016.
- [Powles 1983] S. R. J. Powles. The effects of tower shadow on the dynamics of a horizontal-axis wind turbine. *Wind Engineering*, pp. 26–42, 1983.
- [Prandtl 1918] L. Prandtl. Tragflügeltheorie. *Königliche Gesellschaft der Wissenschaften zu Göttingen*, 1918.

- [Ragheb and Ragheb 2011] M. Ragheb and A. M. Ragheb. Wind turbines theory-the betz equation and optimal rotor tip speed ratio. In *Fundamental and Advanced Topics in Wind Power*. IntechOpen, 2011.
- [Rankine 1854] W. J. M. Rankine. On plane water-lines in two dimensions. *Philosophical Transactions*, 154:369–392, 1854.
- [Ransford 1995] T. Ransford. *Potential Theory in the Complex Plane*, Vol. 28. Cambridge University Press, 1995.
- [Rapin and Ortun 2007] M. Rapin and B. Ortun. 3D rotational corrections in ONERA aeroelastic predictions of NREL wind turbine. In *45th AIAA Aerospace Sciences Meeting and Exhibit*, 2007.
- [Reynolds 1883] O. Reynolds. An experimental investigation of the circumstances which determine whether the motion of water shall be direct or sinuous, and of the law of resistance in parallel channels. *Philosophical Transactions of the Royal Society of London*, 174:935–982, 1883.
- [Richardson 2007] L. F. Richardson. *Weather Prediction by Numerical Process*. Cambridge University Press, 2007.
- [Rogelj *et al.* 2016] J. Rogelj, M. D. Elzen, N.s Höhne, T. Fransen, H. Fekete, H. Winkler, R. Schaeffer, F. Sha, K. Riahi and M. Meinshausen. Paris Agreement climate proposals need a boost to keep warming well below 2 C. *Nature*, 534(7609):631, 2016.
- [Russo 1948] F. Russo. Deux ingénieurs de la Renaissance: Besson et Ramelli. *Thalés*, 5:108–112, 1948.
- [Ruzicka 2008] M. C. Ruzicka. On dimensionless numbers. *Chemical Engineering Research and Design*, 86(8):835–868, 2008.
- [Sant 2007] T. Sant. *Improving BEM-based Aerodynamic Models in Wind Turbine Design Codes*. Delft University of Technology, Stevinweg 1, 2628 CN Delft, Netherlands, 2007.
- [Savonius 1981] S. J. Savonius. *The Wing-Rotor in Theory and Practice*. Omnia-Mikrofilm-Technik, 1981.
- [Schaffarczyk 2014] A. P. Schaffarczyk. *Introduction to Wind Turbine Aerodynamics*. Springer, 2014.
- [Schepers *et al.* 2018] J. G. Schepers, K. Boorsma, N. Sørensen, G. Sieros, H. Rahimi, H. Heisselmann, E. Jost, T. Lutz, T. Maeder, A. Gonzalez, C. Ferreira, B. Stoevesandt, G. Barakos, N. Lampropoulos, A. Croce and J. Madsen. Final results from the EU project AVATAR: Aerodynamic modelling of 10 MW wind turbines. In *Journal of Physics: Conference Series*, Vol. 1037, p. 022013. IOP Publishing, 2018.
- [Scherhaufer *et al.* 2017] P. Scherhaufer, S. Höltinger, B. Salak, T. Schauppenlehner and J. Schmidt. Patterns of acceptance and non-acceptance within energy landscapes: A case study on wind energy expansion in Austria. *Energy Policy*, 109:863–870, 2017.

- [Schlichting 1933] H. Schlichting. Zur entstehung der turbulenz bei der plattenströmung. *Nachrichten von der Gesellschaft der Wissenschaften zu Göttingen, Mathematisch-Physikalische Klasse*, 1933:181–208, 1933.
- [Schlichting and Gersten 2016] H. Schlichting and K. Gersten. *Boundary-Layer Theory*. Springer, 2016.
- [Schoenberg 1946] I. J. Schoenberg. Contributions to the problem of approximation of equidistant data by analytic functions. *Quarterly of Applied Mathematics*, 4(2):45–99, 112–141, 1946.
- [Schubel and Crossley 2012] P. J. Schubel and R. J. Crossley. Wind turbine blade design. *Energies*, 5(9):3425–3449, 2012.
- [Selig 2003] M. S. Selig. *Low Reynolds Number Airfoil Design Lecture Notes*. VKI lecture series, 2003.
- [Selig *et al.* 1995] M. S. Selig, J. J. Guglielmo, A. P. Broeren and P. Giguere. Summary of Low-Speed Airfoil Data, 1995.
- [Simms *et al.* 2001] D. Simms, M. Hand, D. Jager, J. Cotrell, M. Robinson, S. Schreck, S. Larwood and L. Fingersh. Wind tunnel testing of NREL’s unsteady aerodynamics experiment. In *20th 2001 ASME Wind Energy Symposium*, p. 35, 2001.
- [Sintra *et al.* 2014] H. Sintra, V. M. F. Mendes and R. Melício. Modeling and simulation of wind shear and tower shadow on wind turbines. *Procedia Technology*, 17:471–477, 2014.
- [Snel 2003] H. Snel. Review of aerodynamics for wind turbines. *Wind Energy: An International Journal for Progress and Applications in Wind Power Conversion Technology*, 6(3):203–211, 2003.
- [Somers 1997] D. M. Somers. *Design and Experimental Results for the S809 Airfoil*. Technical report, National Renewable Energy Lab, Golden, Colorado, USA, 1997.
- [Sørensen and Kock 1995] J. N. Sørensen and C. W. Kock. A model for unsteady rotor aerodynamics. *Journal of Wind Engineering and Industrial Aerodynamics*, 58(3):259–275, 1995.
- [Sørensen *et al.* 2002] P. Sørensen, A. D. Hansen and P. A. C. Rosas. Wind models for simulation of power fluctuations from wind farms. *Journal of Wind Engineering and Industrial Aerodynamics*, 90(12-15):1381–1402, 2002.
- [Spurk 2013] J. H. Spurk. *Dimensionsanalyse in der Strömungslehre*. Springer-Verlag, 2013.
- [Strouhal 1878] V. Strouhal. Über eine besondere Art der Tonerregung. *Annalen der Physik*, 241(10):216–251, 1878.
- [Sun *et al.* 2016] Z. Sun, J. Chen, W. Z. Shen and W. J. Zhu. Improved blade element momentum theory for wind turbine aerodynamic computations. *Renewable Energy*, 96:824–831, 2016.

- [Tangler 2002] J. L. Tangler. The nebulous art of using wind-tunnel airfoil data for predicting rotor performance. In *ASME 2002 Wind Energy Symposium*, pp. 190–196. American Society of Mechanical Engineers, 2002.
- [Theodorsen 1935] T. Theodorsen. *General Theory of Aerodynamic Instability and the Mechanism of Flutter*. Technical Report NACA Report Nr. 496, National Advisory Committee for Aeronautics, Washington, DC, 1935.
- [Thomson (Lord Kelvin) 1871] W. Thomson (Lord Kelvin). Hydrokinetic solutions and observations. *Philosophical Magazine*, 42:362–377, 1871.
- [Tietjens and Prandtl 1957] O. K. G. Tietjens and L. Prandtl. *Fundamentals of Hydro- and Aeromechanics*, Vol. 1. Courier Corporation, 1957.
- [Tollmien 1929] W. Tollmien. Über die entstehung der turbulenz Nachr. *Ges. Wiss. Göttingen Math.-Phys. Kl*, pp. 21–44, 1929.
- [Tsien 1939] H.-S. Tsien. Two-dimensional subsonic flow of compressible fluids. *Journal of the Aeronautical Sciences*, 6(10):399–407, 1939.
- [UNFCCC. 2015] UNFCCC. *Adoption of the Paris Agreement*. Report No. FCCC/CP/2015/L.9/Rev.1. UNFCCC, 2015.
- [Van Dyke 1982] M. Van Dyke. *An Album of Fluid Motion*. Parabolic Press, Stanford, California, USA, 1982.
- [Van Garrel 2003] A. Van Garrel. *Development of a Wind Turbine Aerodynamics Simulation Module*. Technical Report ECN-C-03-079, Energy research Centre of the Netherlands ECN, 2003.
- [Van Kuik 2007] G. Van Kuik. The Lanchester–Betz–Joukowsky limit. *Wind Energy: An International Journal for Progress and Applications in Wind Power Conversion Technology*, 10(3):289–291, 2007.
- [Van Kuik and Peinke 2016] G. Van Kuik and J. Peinke. *Long-term Research Challenges in Wind Energy - a Research Agenda by the European Academy of Wind Energy*, Vol. 6. Springer, 2016.
- [Van Rooij and Timmer 2004] R. Van Rooij and N. Timmer. *Design of Airfoils for Wind Turbine Blades*. Delft University of Technology, The Netherlands, 2004.
- [von Eötvös 1910] R. von Eötvös. Verhandlungen der 16 allgemeinen konferenz der internationalen erdmessung, 319, G. Reiner, 1910.
- [von Helmholtz 1868] H. von Helmholtz. Über diskontinuierliche Flüssigkeitsbewegungen. *Monatsberichte der Königlich Preussische Akademie der Wissenschaften zu Berlin*, 23:215–228, 1868.
- [von Kármán 1941] T. von Kármán. Compressibility effects in aerodynamics. *Journal of the Aeronautical Sciences*, 8(9):337–356, 1941.

- [Wang and Coton 2001] T. Wang and F. N. Coton. A high resolution tower shadow model for downwind wind turbines. *Journal of Wind Engineering and Industrial Aerodynamics*, 89(10):873–892, 2001.
- [Wang and Zhao 2015] Q. Wang and Q. Zhao. Modification of Leishman–Beddoes model incorporating with a new trailing-edge vortex model. *Proceedings of the Institution of Mechanical Engineers, Part G: Journal of Aerospace Engineering*, 229(9):1606–1615, 2015.
- [Warn *et al.* 1995] T. Warn, O. Bokhove, T. G. Shepherd and G. K. Vallis. Rossby number expansions, slaving principles, and balance dynamics. *Quarterly Journal of the Royal Meteorological Society*, 121(523):723–739, 1995.
- [Werlé 1974] H. Werlé. *Le Tunnel Hydrodynamique au Service de la Recherche Aérospatiale*, Vol. n. 156. ONERA, Office National d’Études et de Recherches Aérospaceiales, 1974.
- [Wermer 1981] J. Wermer. *Potential Theory*. Springer Verlag, 1981.
- [White 2011] F. M. White. *Fluid Mechanics*. McGraw-hill, 7th edition, 2011.
- [Willis *et al.* 2018] D. J. Willis, C. Niezrecki, D. Kuchma, E. Hines, S. R. Arwade, R. J. Barthelmie, M. DiPaola, P. J. Drane, C. J. Hansen, M. Inalpolat, J. H. Mack, A. T. Myers and M. Rotea. Wind energy research: State-of-the-art and future research directions. *Renewable Energy*, 125:133–154, 2018.
- [Wilson *et al.* 2018] D. Wilson, S. Rodrigues, C. Segura, I. Loshchilov, F. Hutter, G. L. Buenfil, A. Kheiri, E. Keedwell, M. Ocampo-Pineda, E. Özcan, S. I. V. Peña, B. Goldman, S. B. Rionda, A. Hernández-Aguirre, K. Veeramachaneni and S. Cussat-Blanca. Evolutionary computation for wind farm layout optimization. *Renewable Energy*, 126:681–691, 2018.
- [Wolfe and Ochs 1997] W. Wolfe and S. Ochs. CFD calculations of S809 aerodynamic characteristics. In *35th Aerospace Sciences Meeting and Exhibit*, p. 973, 1997.
- [Wucknitz 1977] J. Wucknitz. Disturbance of wind profile measurements by a slim mast. *Boundary-Layer Meteorology*, 11(2):155–169, 1977.
- [Yu and Kwon 2014] D. O. Yu and O. J. Kwon. Predicting wind turbine blade loads and aeroelastic response using a coupled CFD–CSD method. *Renewable Energy*, 70:184–196, 2014.
- [Zahle *et al.* 2009] F. Zahle, H. Aa. Madsen and N. N. Sørensen. Evaluation of tower shadow effects on various wind turbine concepts. In *Risoe*, pp. 11–29. Danmarks Tekniske Universitet, Risø Nationallaboratoriet for Bæredygtig Energi, 2009.
- [Zangenberg *et al.* 2014] J. Zangenberg, P. Brøndsted and M. Koefoed. Design of a fibrous composite preform for wind turbine rotor blades. *Materials & Design (1980-2015)*, 56:635–641, 2014.